Preprint typeset in JINST style - HYPER VERSION

MicroBooNE

A.N. Author[1]

[1]*Institution 1, City, State 12345*

ABSTRACT: This paper describes the design and construction of the MicroBooNE liquid argon time projection chamber and associated systems. Details of design specifications, assembly procedures, and acceptance tests are reported.

KEYWORDS: Time projection chambers; Noble-liquid detectors; Data analysis.

Contents

Date: September 21, 2016; Paper Version: 1.0

1. Introduction and Physics Motivation

Neutrino detection is entering a new era with a number of large precision neutrino detectors, specifically Liquid Argon Time Projection Chambers (LArTPCs), now in design, construction, data taking, and analysis, both for long and short baseline neutrino oscillation experiments. The **Micro** **Boo**ster **N**eutrino **E**xperiment, henceforth referred to as MicroBooNE, is the first large ($\sim$100 tons) LArTPC to operate in the United States and the second only after ICARUS to operate worldwide. LArTPC detectors combine fine-grained tracking with total absorption calorimetry to provide excellent signal efficiency and background rejection.

The MicroBooNE experiment combines a physics program of short-baseline oscillations and neutrino cross-section measurements with development goals to inform larger scale construction of LArTPCs for the long-baseline program. MicroBooNE's principal physics goal is to address the long standing unsolved puzzles generated by short-baseline neutrino oscillation results from past experiments. These include results from accelerator based experiments, LSND and MiniBooNE, reactor experiments, and radiochemical experiments. The LSND accelerator based oscillation experiment observed anti-electron neutrino appearance in an anti-muon neutrino beam. The MiniBooNE experiment [1] also investigated (anti)muon- to (anti)electron-neutrino oscillations and found a significant deviation from the expectation in the number of electron (anti)neutrino candidates at low energy ($\sim$ 200-500 MeV). Other hints come from a re-analysis of the expected reactor antineutrino flux that suggests a deficit of reactor neutrinos [2, 3], and the analysis of calibration data taken by GALLEX and SAGE [4, 5] radiochemical experiments. Interpreting these results through neutrino oscillations suggests a mass squared difference on the order of $\sim$1 eV^2 and an oscillation probability consistent with small mixing, incompatible with the oscillation parameters from solar and atmospheric results. These signals can be interpreted as oscillations to sterile neutrinos, which are neutrinos that do not interact via the weak interaction but which can oscillate with the three standard model neutrinos. While each of the short baseline results taken alone does not reach the statistical significance to claim a discovery, combining them together suggests sterile neutrino oscillations or some other phenomena underway at short baselines. Definitive evidence for sterile neutrinos would constitute a revolutionary discovery, with strong implications for particle physics as well as for cosmology. Proposals to address these signals by employing reactor, accelerator, and radioactive source experiments are in the planning stages or underway worldwide.

MicroBooNE will address short baseline neutrino oscillations, specifically the MiniBooNE low energy excess result, at Fermi National Accelerator Laboratory (Fermilab). MicroBooNE will be exposed to the 0.5-2 GeV on-axis Booster Neutrino beam, the same beam used for the MiniBooNE experiment, at a $\sim$ 500 m baseline, also the same as MiniBooNE, but by employing the LArTPC technology to efficiently separate signal electrons from background photons. In addition to MicroBooNE's signature oscillation analyses, a suite of precision cross-section measurements will be performed, critical both for future LArTPC oscillation experiments and for what can be learned about neutrino interactions in general. In the neutrino interactions from Fermilab's Booster Neutrino Beamline (BNB), multiple interaction processes (quasi-elastic, resonances, deep inelastic scattering) are possible, and complicated nuclear effects in neutrino interactions on argon result in a variety of final states. These can range from the emission of several nucleons to more complex topologies with multiple pions, all in addition to the leading lepton in charged-current events. The

LArTPC technology employed by MicroBooNE is particularly well suited for complicated topologies because of its excellent particle identification capability and calorimetric energy reconstruction down to very low detection thresholds. MicroBooNE will also be supernova live and capable of detecting a galactic supernova, and prepare the analysis of the search for proton decays. For a proton decay search, the experiment will not have a competitive sensitivity due to too small target mass. However, this will be an important proof of principle measurement towards future searches in larger detectors.

MicroBooNE is the first phase of a staged program of neutrino detectors at short baseline (the Short Baseline Neutrino (SBN) program at Fermilab) exposed to the on-axis BNB beam and an off-axis component of the NuMI beam (Neutrinos from the Main Injector) at Fermilab.

The MicroBooNE experiment is located 470 m from the BNB production target and 600 m from the NuMI production target. MicroBooNE began operations in late 2015 for an anticipated $\sim$3 year data taking run to be followed by data taking as part of the full SBN program beginning in 2018 with the commencement of operations of the SBND [6] and ICARUS experiments, located at 110 m and 600 m respectively from the BNB production target. MicroBooNE will definitively address whether or not the MiniBooNE low energy excess in neutrino mode is due to electrons or photons. SBND will look for this low energy excess at the near location (110m) from the production target, and the three detectors combined will cover the entire LSND allowed region in neutrino parameter space to 5σ through ν_e appearance.

The LArTPC technique will be used by MicroBooNE at a relatively large scale, so far only surpassed by the ICARUS T600 detector. The potential of liquified noble gases to be employed as the detection media in particle detectors with high spatial resolution was recognized in the 1960's [7]. Large calorimeters for the measurement of particle energy were then realized by using cryogenic noble liquids as active components [8]. Furthermore, the LArTPC was proposed at CERN by C. Rubbia in 1977 [9] as a detector capable of providing uniform and precise imaging of large volumes.

The implementation of the LArTPC idea was extensively developed within the ICARUS experiment through an intense R&D program. Various prototype detectors were realized and operated to develop the systems needed for larger physics experiments. Techniques for purification, signal readout electronics, and cryogenics were developed. The largest ICARUS test device had a mass of about 3 tons of LAr [10, 11] and allowed for the collection of large samples of cosmic-ray events. In parallel, a smaller volume detector (50 liters of LAr) was exposed to the CERN WANF neutrino beam allowing the detection of neutrino interaction events for the first time in a LArTPC [12].

The largest LArTPC detector built so far is the 600-ton ICARUS T600 detector, which was operated first on the surface exposed to cosmic rays [13] before deployment underground at LNGS for operation in the CNGS neutrino beam. ICARUS measurements have shown that the technique is viable at large scales with a drift length as long as 1.5 m [14 – 18].

The success of the construction of the T600 motivated several follow up ideas aimed at reaching even higher target masses [19]. A monolithic magnetized large mass device was proposed in [20], based on the scaling up of the ICARUS approach. The ICARUS experience led then to the broader development of the LArTPC concept. A LArTPC design envisioning a single cylindrical volume of 70 m diameter and 20 m height, called GLACIER, was discussed in [21, 22], based on a double-phase readout. This approach eventually evolved to the LAGUNA [23] proposal and to the

LAGUNA LBNO [24, 25] conceptual design, aimed at a large detector placed along a long-baseline beam from CERN to an European underground site. In the United States, an analogous multi-kton detector was proposed using conventional single-phase wire readout for the LBNE project [26], aimed at a long-baseline neutrino beam sent from Fermilab to the Sanford Laboratory in South Dakota. The LBNE and LBNO efforts have now largely merged to form the DUNE experiment [27].

In parallel, LArTPCs were also considered for short-baseline neutrino experiments, motivating the use of relatively smaller size devices. At Fermilab, the first LArTPC to be successfully operated in the NuMI beam was the ArgoNeuT detector [28] that, despite the relatively small mass of ~ 170 kg, has been able to perform a series of detailed studies on the interaction of medium-energy neutrinos[29 – 32]. Other critical development projects are currently underway at Fermilab such as [33 – 37], all geared towards development of the technology and of analyzing particle interactions in the detectors. The goal of the development in the near term is towards the SBN program experiments, and in the farther term, following the recent recommendations of the P5 panel [38], the LBNF project and the DUNE experiment which envisions an internationally coordinated effort for the realization of an intense neutrino beam facility at Fermilab and a far large mass neutrino detector in a long-baseline configuration (> 1000 km).

More information on the LArTPC technology can be found in existing reviews (see, e.g., [39] and references therein).

Organization of Document This document describes the design, construction, and technical details of the MicroBooNE experiment. Section 2 gives a brief review of the LArTPC technique and its implementation in MicroBooNE. Section 3 describes the cryogenic and purification systems which are required for maintaining a stable volume of highly purified liquid argon. The LArTPC detector described in section 4 is the centerpiece of the experiment, providing fine-grained images of neutrino interactions. A light collection system, described in section 5, provides precise timing information by viewing the detector volume and recording signals from the scintillation light that is produced therein. Signals from the light collection system and from the LArTPC are amplified, sampled, and recorded by a custom-designed electronic and readout system, as described in section 6. Section 7 describes the auxiliary instrumentation that monitor and control the detector and all of its associated systems, as well as provide an electrically quiet environment for the experiment to operate. Finally, one of the main calibration sources for the experiment is an ultraviolet laser system, described in section 8, that provides the capability to map out the performance of the LArTPC detector. A cosmic ray tagger system, under construction at the time of the writing of this paper, will be sited to beam right and left, and above and below the detector cryostat.

2. Experiment Overview

The MicroBooNE detector at Fermilab in Batavia, Illinois is sited on axis on the BNB, 470m downstream from the neutrino production target. The BNB delivers a beam of predominantly muon neutrinos with energies peaking at 700 MeV produced primarily from pion decays. MicroBooNE is also exposed to an off-axis component of the NuMI beam [40] produced from pion and kaon decays with average neutrino energies of about 2 GeV and 0.5 GeV respectively. MicroBooNE is located about 600m downstream from the NuMI neutrino production target. The characteristics of the BNB beamline are well measured and understood from many years of data taking and analysis on the MiniBooNE experiment [41], which operated directly downstream of the MicroBooNE location. Figure 1 shows the arrangement of MicroBooNE with respect to the BNB and NuMI beamlines at Fermilab. The physics program of MicroBooNE will utilize both BNB and NuMI samples. MicroBooNE will also collect data that is out-of-time with either beam, which will be useful for developing analyses (e.g. proton decay searches) relevant for next-generation detectors. The primary detector technology employed by MicroBooNE is the LArTPC, whose operating principle is described in this section.

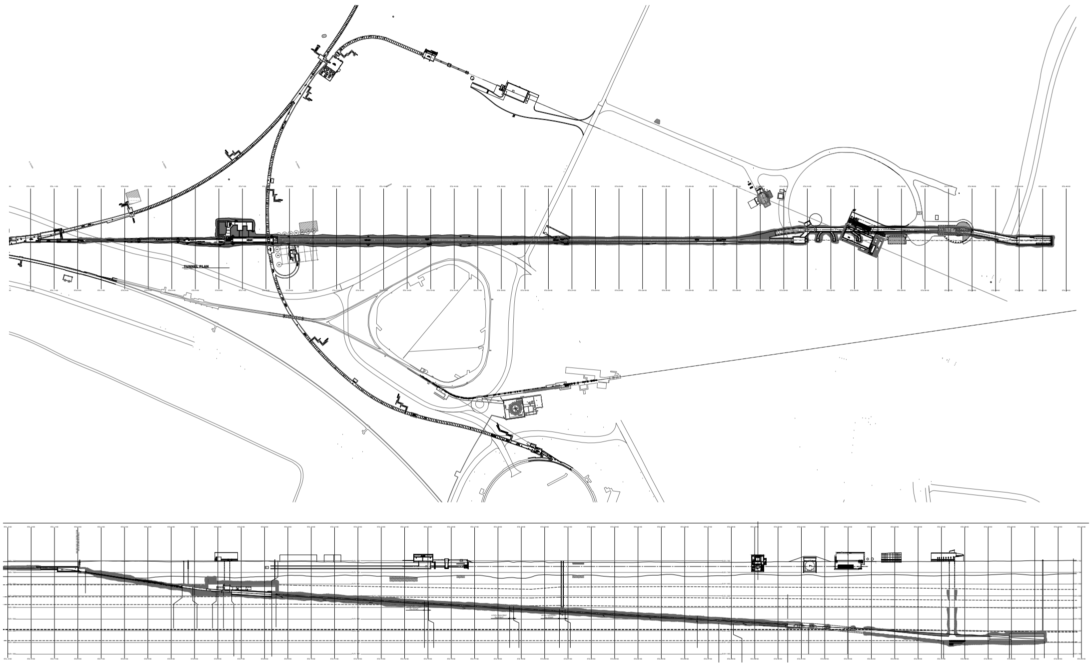

Figure 1: Plan (top) and cross-sectional (bottom) views of MicroBooNE. MicroBooNE is on-axis to the BNB, and off-axis to the NuMI beam.

2.1 The MicroBooNE LArTPC

Charged particles traversing a volume of highly-purified liquid argon leave trails of ionization electrons in their wake and also create prompt vacuum ultraviolet (VUV) scintillation photons. In a LArTPC , the liquid argon is highly purified and the ionization trails are transported practically undistorted over distances of the order of meters [42] under the influence of a uniform electric field in the detector volume, until they reach anode planes located along one side of the active volume. The uniform electric field is created by introducing voltage onto a cathode plane and gradually stepping that voltage down in magnitude across a field cage, which is formed from a series of equipotential rings surrounding the drift volume. The anode plane is arranged parallel to the cathode plane, and in MicroBooNE, parallel to the beam direction. There are typically three planes of sense wires comprised of wires with a characteristic pitch, held at a predetermined bias voltage, that continuously sense the signals induced by the ionization electrons drifting towards them. The electrostatic potentials of the sequence of anode planes allow ionization electrons to pass undisturbed by the first planes before ultimately ending their trajectory on a wire in the last plane. The drifting ionization thus induces signals on the first planes (referred to as Induction planes) and directly contributes to the signals in the final plane (referred to as the Collection plane). Figure 2 depicts a simplified arrangement for a LArTPC.

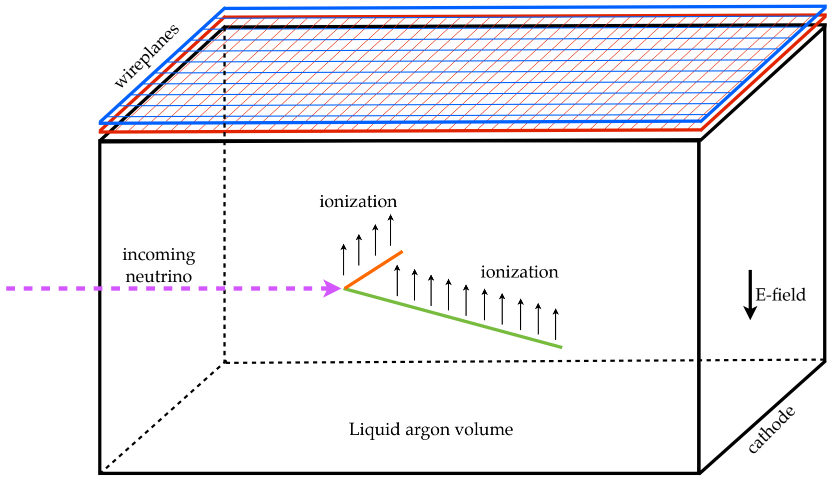

Figure 2: Operational principle of a LArTPC.

The charged particle trajectory is reconstructed using the known positions of the anode plane wires and the recorded drift time of the ionization. The drift time is the difference between the arrival times of ionization signals on the wires and the time the interaction took place in the detector (t_0) which is provided by an accelerator clock synced to the beam (e.g. - BNB or NuMI) or from a trigger provided by the light collection system. The characteristics of the waveforms observed by each wire provide a measure of the energy deposition of the traversing particles near that wire, which, when taken as a whole for each contained particle's trajectory, allow for determination of momentum and particle identity.

The scintillation photons are detected by a light collection system that is immersed in the liquid argon and faces into the detector volume. This system provides signals that can establish the event t_0 and supplies trigger information to an electronic readout system. The light collection system signals are vital in distinguishing detector activity that is in-time with the beam (e.g. originating from beam interactions) from that which is out-of-time (e.g. likely not originating from beam-related interactions), benefiting event reconstruction. Spatial information transverse to the drift direction can also be inferred from the light collection signals, further aiding in the reconstruction of the activity occurring inside the detector.

The choice of liquid argon as both the neutrino target and detector medium in LArTPCs is well motivated, though not without introducing unique considerations for experimental design. Liquid argon as a target for neutrinos is attractive due to its density, allowing a more compact detector with a substantial boost in event rate over a comparable detector using less dense media, such as water. A tradeoff to this aspect is the short radiation length (14 cm) and that the complicated structure of the argon atom, relative to simpler targets such as hydrogen or helium, does introduce nuclear effects that must be considered during data analysis. The cryogenic temperatures at which the noble elements are in the liquid phase also introduces the need for additional design considerations to ensure stable and safe operations.

Table 1 lists some of the properties of liquid argon that are salient for LArTPC design. The noble liquids are all characterized by their excellent dielectric properties, able to maintain high voltages without suffering electrical breakdown. The long drift lengths over which ionization electrons must travel in large LArTPC detectors requires the presence of a uniform electric field over that distance. This is achieved via the introduction of extremely high voltage ($\mathscr{O}$(100 kV) magnitude) onto the LArTPC cathode; this voltage is suitably maintained due to the dielectric properties of liquid argon and by ensuring the detector components have no sharp edges. The noble liquids are all very bright scintillators, with wavelengths deep in the UV, and also produce copious amounts of ionization. Both the scintillation and the ionization signals are necessary for a robust accounting of the activity occurring inside the LArTPC. Finally, the desire to build LArTPCs on increasingly larger scales, such as those necessary in neutrino experiments, is bolstered by the abundance (1% of atmosphere) and low cost of argon.

Table 1: Selected properties of liquid argon.

Property	Value	Reference
Atomic number	18	
Atomic weight [g/mol]	39.95	
Boiling point [K] @ 1 atm	87.3	[43]
Density [g/cm^3] @ 1 atm	1.4	[43]
Dielectric constant	1.505	[44]
Radiation length [cm]	14.0	[45]
Molière radius [cm]	10.0	[45]
W-value for ionization [eV/pair]	23.6	[46, 47]
Minimum specific energy loss [MeV/cm]	2.12	[45]
Electron transverse diffusion coef. [cm^2/s]	13	[48, 49, 11]
Electron longitudinal diffusion coef. [cm^2/s]	5	[11, 50]

The successful implementation of the LArTPC technique depends critically on several factors. The liquid argon must be purified of any electronegative contaminants, such as water or oxygen, to accommodate the very long drift path of ionization through a MicroBooNE-sized LArTPC without significant charge loss. The signals that the ionization electrons create on the anode wires are very small, requiring low-noise electronics to discern signal pulses. The MicroBooNE collaboration has designed and constructed an experiment that addresses all of these considerations, providing critical technological development for the next generation of LArTPC experiments to build upon.

2.2 MicroBooNE LArTPC Implementation

MicroBooNE's LArTPC active volume, which is defined as the volume immediately within the confines of the LArTPC field cage, is a rectangular liquid argon volume with dimensions 2.3 m vertical x 2.5 m horizontal x 10.4 m along the beam direction. This is the maximum volume that can be used for physics analyses. The cathode (anode) defines the beam-left (beam-right) side of the active volume. The end of the LArTPC that the beam first encounters is referred to as the “upstream" end, while the opposite end is referred to as “downstream". Anode plane-to-plane spacing is 3 mm, and each plane has 3 mm wire pitch. The induction plane wires are oriented at $\pm 60^\circ$ relative to vertical, and the collection plane has vertically oriented wires. Field cage loops are employed to maintain uniformity of the electric field across the entire width of the detector, and these loops also act to define the top, bottom, upstream, and downstream sides of the active volume.

MicroBooNE uses a right-handed Cartesian coordinate system, with the origin defined to be located on the upstream face of the LArTPC, centered halfway up the vertical height of the active volume and horizontally centered on the anode plane closest to the cathode (the innermost anode plane). In this system, x ranges from 0.0 m at the innermost anode plane to $+2.5$ m at the cathode, y ranges from -1.15 m on the bottom of the active volume to $+1.15$ m at the top of the active volume, and z ranges from 0.0 m at the upstream end of the active volume to $+10.4$ m at the downstream end.

The light collection system, which is an array of photomultiplier tubes and scintillator paddles, is located directly behind the anode planes on beam-right, facing the detector volume through the anode planes. The LArTPC and light collection system are immersed in liquid argon contained within a single-walled cryostat with a 170 ton capacity. Electronics mounted directly on the LArTPC amplify the signals on the wires, which are then passed out of the cryostat for further processing and storage on disk. Table 2 lists the primary detector design parameters of MicroBooNE, and figure 3 shows a schematic of the cross section of the detector. Details of these design parameters and construction of all detector subsystems will be provided in the subsequent sections.

Table 2: Primary detector design parameters for MicroBooNE.

Parameter	Value
LArTPC Dimensions	2.325 m vertically
	2.560 m horizontally
	10.368 m longitudinally
LArTPC argon mass	90 tons
Total Number of Wires	8256
Induction0 Wires	2400
Induction1 Wires	2400
Collection Plane Wires	3456
Drift field	500 V/cm
Light collection	30 8” diameter PMTs
	4 scintillator paddles
Cryostat liquid argon capacity	170 tons
Operating temperature	87 K
Operating pressure	2 psig

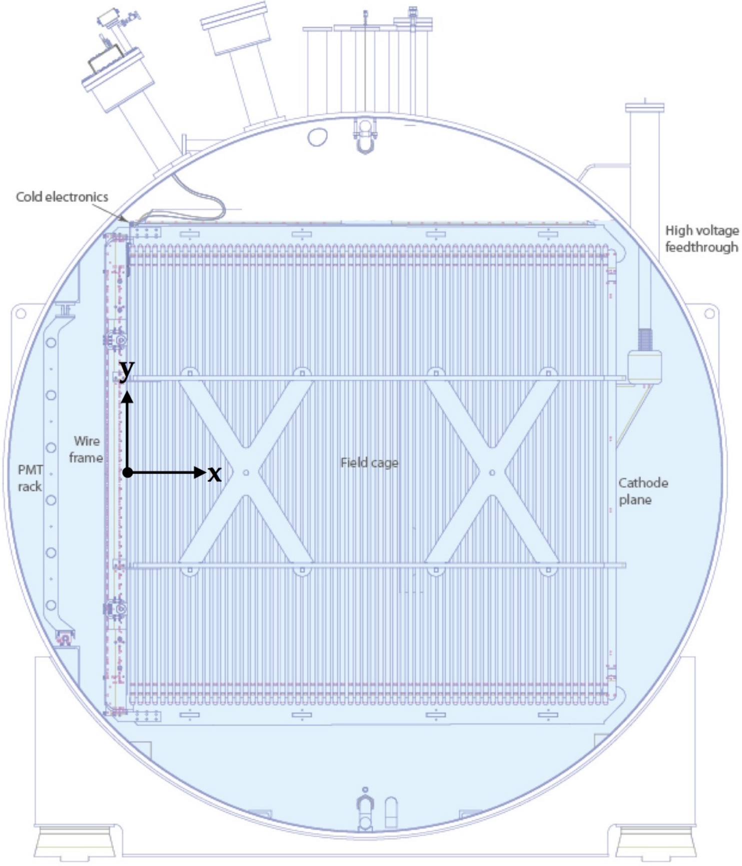

Figure 3: Schematic of the cross section of the MicroBooNE LArTPC. In this view, the beam would be directed out of the page (in the z direction).

3. Cryogenic System

The use of large quantities of highly-purified liquid argon as a detector medium in MicroBooNE requires a sophisticated cryogenic infrastructure that can maintain stable operations for years at a time. Not only must the purity of the liquid argon be maintained, but the pressure and temperature gradients within the LArTPC active volume must be tightly controlled as the drift velocity of electrons is dependent on these quantities. A customized cryogenic system that serves these purposes has been built, and the requirements for this system are shown in table 3.

The MicroBooNE cryogenic system is represented in figure 4. The central component of the system is a cryostat that houses the complete LArTPC and light-collection detector systems. The cryostat is supported by three major subsystems: the argon purification system, the nitrogen refrigeration system, and the controls and monitoring system. These systems each represent the next generation of LArTPC cryogenic system after the Liquid Argon Purity Demonstrator (LAPD) [35] and make considerable use of the expertise gained during the design and implementation of that apparatus.

Table 3: Primary design requirements for MicroBooNE cryogenic and purification systems.

Parameter	Value	Motivation
Argon purity	$<$100 ppt O_2	MIP identification at longest drift
Argon purity	$<$2 ppm N_2	Scintillation light output
LAr Temperature gradient	$<1^\circ$ K	Drift-velocity uniformity
LAr recirculation rate	1 volume change/day	Maintain purity
Cryostat heat load	$<$15 W/m^2	Minimize convection currents and bubbles
Cryogenic capacity	10 kW	Capacity to deal with expected heat load
Cryostat maximum pressure	30 psig	Determines relief sizing

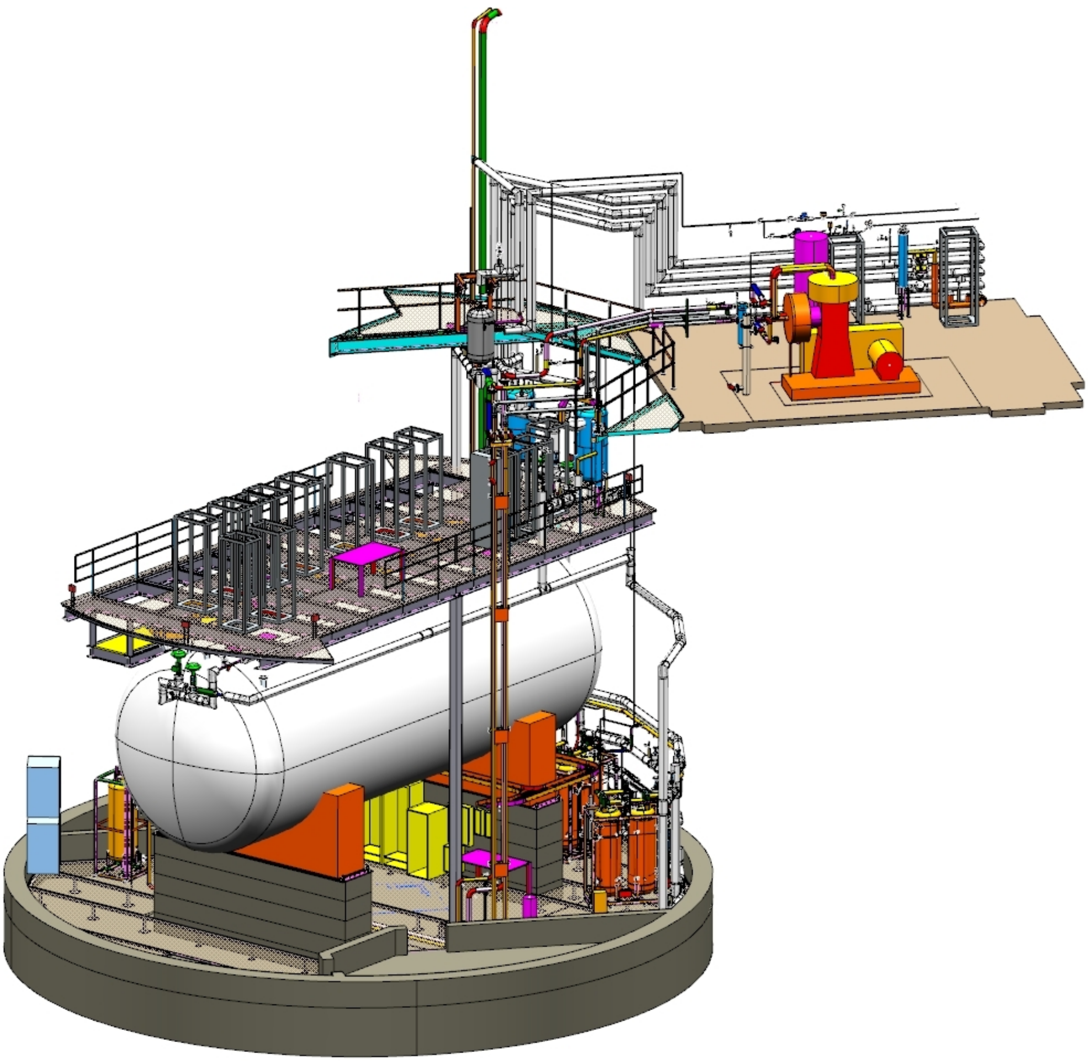

Figure 4: Three-dimensional renderings of the MicroBooNE cryogenic system installed at LArTF.

3.1 Cryostat Design Overview

Three major components make up the MicroBooNE cryostat: a stainless steel (type 304) vessel to contain the liquid argon and all the active detector elements, front and rear supports to carry the weight of the fully loaded cryostat, and foam insulation covering the cryostat outer surfaces. The foam insulation serves to reduce heat input from the ambient environment to a sufficiently low level to prevent large temperature gradients and boiling of the liquid argon. The cryostat and the cryogenic systems are designed to achieve the high-purity liquid argon needed to allow ionization electrons to drift to the anode wires with low probability of capture, and the high degree of thermal homogeneity needed to avoid the introduction of non-constant drift velocities for the ionization electrons. Finally, the outer diameter of the vessel is designed to be the maximum standard size for over-the-road transport.

Ionization electrons must not be significantly attenuated, via attachment to electronegative contaminants in the liquid argon, as they drift up to 2.5 m across the active volume. This dictates that the argon be kept free of electronegative contaminants to the level of 100 parts-per-trillion (ppt). The cryostat is designed to minimize outgassing (desorption) and to avoid leakage and diffusion of air into the system. This requirement imposes strict quality assurance demands on all welds for penetrations into the cryostat and on cleaning and handling procedures for the finished vessel. Achieving the required level of purity is accomplished with a purification system, described in section 3.2, that removes electronegative contaminants from the argon during the initial fill and those introduced over time by leaks and outgassing of system components.

The electron drift velocity ($v_d = 1600$ m/s at an electric field of 500 V/cm, with a liquid argon temperature dependence $\Delta v_d / v_d = -0.019 \Delta T$) must remain constant in magnitude and direction throughout the active liquid argon volume to avoid distortion of the mapping of drift time into the position along the drift ($\hat{x}$) direction. This requirement limits the allowable temperature variations of the liquid argon to less than 0.1 K and the laminar and turbulent flow rate of liquid argon to less than 1 m/s. These requirements limit fractional errors in velocity, and therefore in the drift-coordinate determination, to be less than 0.1%. The constraints on constancy of drift velocity affect the design by imposing limits on the acceptable heat flux through the insulation.

The cryostat is constructed to the latest American Society of Mechanical Engineers (ASME) boiler code requirements [51] and features a single-walled construction, cylindrical shape, and domed caps closing each end, as shown in figure 5. One end was removed for installation of the active detectors, welded back in place upon completion of that task, and then recertified to the ASME code requirements. Upon installation of the sealed cryostat in its final location at the Liquid Argon Test Facility (LArTF), 16 inches of spray-on, closed cell, Polyurethane insulation was applied to the exterior of the cryostat, as shown in figure 6. At LArTF, to avoid ground loops that could interfere with the LArTPC signals, the cryostat vessel is grounded in only one place, allowing it to act as a Faraday cage. This grounding scheme is explained further in section 7.1.

The vessel surface has 34 nozzle penetrations for cryogenic and electrical services, detailed in table 4. All nozzles are sealed with feedthroughs, flanges, or pipes that are suitable for operation at the nominal pressure and temperature of the cryostat.

3.2 Liquid Argon Purification Subsystem

The heart of the cryogenic system is the liquid argon purification subsystem. The primary requirement of this subsystem is to keep the level of electronegative contamination to below 100 ppt of oxygen-equivalent contaminants. This requirement was determined by the physics needs of the

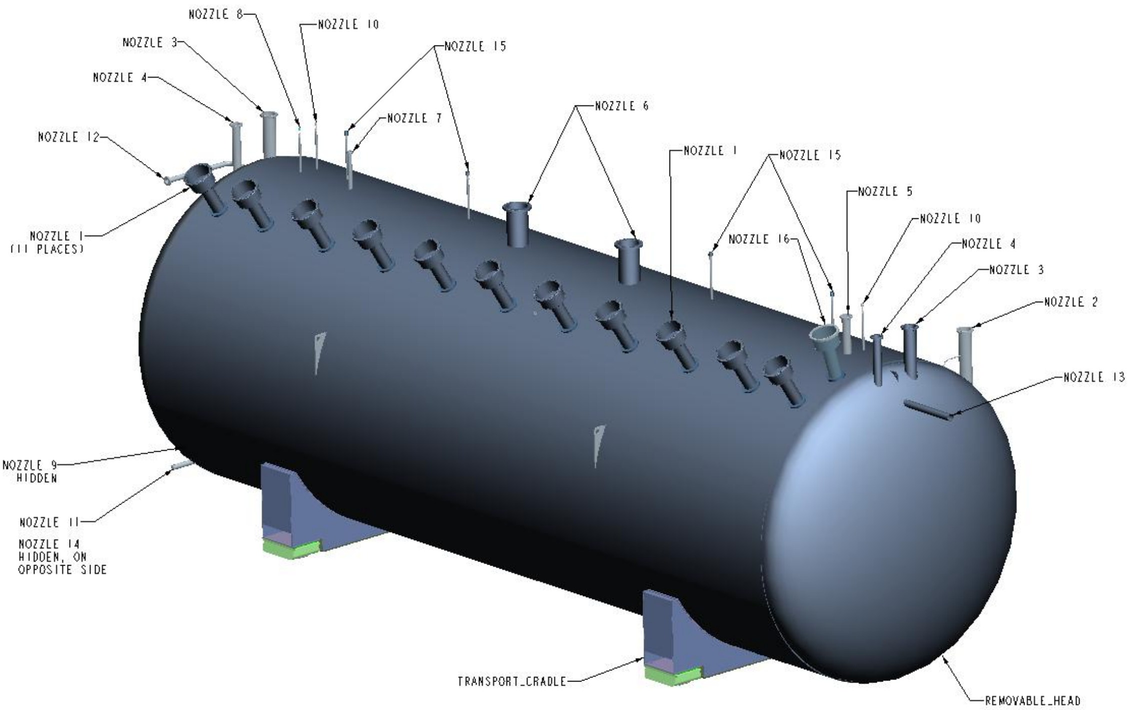

Figure 5: MicroBooNE cryostat with nozzle penetrations labeled.

Figure 6: Photographs of the cryostat after application of exterior foam insulation.

experiment, namely the need to keep the attenuation of ionization electrons to less than 20% over the longest drift distance in the LArTPC. In addition to the requirement on the electronegative con-

Table 4: List of nozzle penetrations in MicroBooNE cryostat. CF=ConFlat flanges, RFWN=raised face weld neck flanges.

Nozzle ID	Function	Flange
N1A-N1K	LArTPC Signal Feedthrough	14" CF
N2	LArTPC HV Feedthrough	8" CF
N3A-N3B	Purity Monitor	8" CF
N4	Temperature Signals	6" CF
N5	Safety Vent	4" RFWN
N6A-N6B	Vacuum Pump-Out	10" RFWN
N7	Condensor	3"
N8	Top Instrument Port	3/4"
N9	Bottom Instrument Port	3/4"
N10A-N10B	Liquid Level Probe	3/4"
N11	Gas Circulation In	2"
N12	Gas Circulation Out	2"
N13	From LAr Filters	3"
N14	To LAr Pumps	2"
N15A-N15B	Laser Calibration	2-3/4" CF
N16	PMT Signal Feedthrough	14" CF
N17	Spare	6" CF
N18	Temperature Signals	6" CF
N19	Spare	6" CF

tamination, the system must maintain the level of nitrogen contamination in the argon at less than 2 parts per million (ppm) [52] to keep the attenuation of the scintillation photons in the argon to a minimum.

The MicroBooNE argon purification subsystem consists of liquid argon pumps and filters that serve to circulate the argon and remove impurities that degrade the quality of the data collected by the active detectors. There are two pumps in the system arranged in parallel in order to allow for continuous recirculation while one pump is being serviced. Similarly, there are two sets of filters arranged in parallel in the system. Figure 7 schematically depicts the flow of liquid and gaseous argon in the MicroBooNE cryogenic system.

The recirculation pumps are Barber-Nichols [53] BNCP-32B-000 magnetically-driven partial-emission centrifugal pumps. Each pump isolates the liquid argon from the electric motor. The impeller, inducer, and driving section of the magnetic coupling each have their own bearings that are lubricated by the liquid argon at the impeller. The motor is controlled by a variable frequency drive (VFD) that allows adjustment of the pump speed to produce the desired head pressure and flow within the available power range of the motor.

Each filter skid contains two filters, each having identically-sized filtration beds of 77 liters. The first filter that the argon stream enters contains a 4A molecular sieve supplied by Sigma-Aldrich [54] that primarily removes water contamination but can also remove small amounts of nitrogen and oxygen. The second filter contains BASF CU-0226 S, a highly-dispersed copper ox-

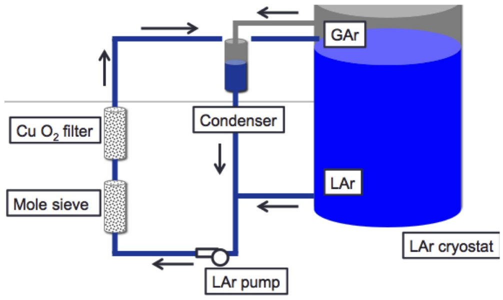

Figure 7: Flow diagram of argon in MicroBooNE, showing direction of liquid and gaseous argon in the cryogenic system. Gaseous argon from the cryostat is condensed and directed through the purification subsystem. Liquid argon drawn from the cryostat volume is directed into the purification subsystem. **NOTE: Update with better figure!**

ide impregnated on a high-surface-area alumina, which removes oxygen [55] and, to a lesser extent, water. Thus, the oxygen filter is placed downstream of the molecular sieve to maximize oxygen filtration. The oxygen-filtering media must be reduced to copper with the procedure described below before it can remove oxygen from the liquid argon. The filters are insulated with vacuum jackets and aluminum radiation shields. The metallic radiation shields were chosen because the filter regeneration temperatures, described below, would damage traditional aluminized mylar insulation. Pipe supplying the filter regeneration gas is insulated both inside the filter vacuum-insulation space and outside the filter with Pyrogel XT which is an aerogel-based insulation [56] that can withstand temperatures up to 650°C.

The filters are regenerated *in situ* using heated gas, by a procedure developed for LAPD. The filters are regenerated using a flow of argon gas that is heated to 200°C, supplied by a commercial 500 liter liquid argon dewar. Once the argon gas reaches 200°C, a small flow of hydrogen is mixed into the primary argon flow and exothermically combines with oxygen captured by the filter to create water. Too much hydrogen mixed in with the primary argon flow would induce temperatures that are sufficiently high to damage the copper-based filter media. The damage is induced by sintering of the copper, which reduces the available filter surface area. Thus, precautions are taken to maintain a hydrogen fraction below 2.5% of the heated gas mixture. During the heated gas regeneration, five filter-bed temperature sensors monitor the filter-material temperature and the water content of the regeneration exhaust gas is measured. To remove any remaining trace amounts of water, the filters are then evacuated using turbomolecular vacuum pumps while they cool.

A particulate filter with an effective filtration of 10 microns, positioned between the cryostat and the filter skids, prevents any debris in the piping from being introduced into the cryostat. The particulate filter consists of a commercial stainless steel sintered-metal cylinder mounted in a custom cryogenic housing and vacuum jacket. Filtration is accomplished by flowing liquid argon to the interior, then outward through the walls, of the sintered-metal cylinder. Flanges on the argon piping, along with flanges and edge-welded bellows on the vacuum jacket, allow removal of the particulate filter.

The argon-purification piping is 2.54 cm diameter stainless steel that was pre-insulated by the manufacturer with 10.2 cm of polyurethane foam. During the fabrication process, all piping was

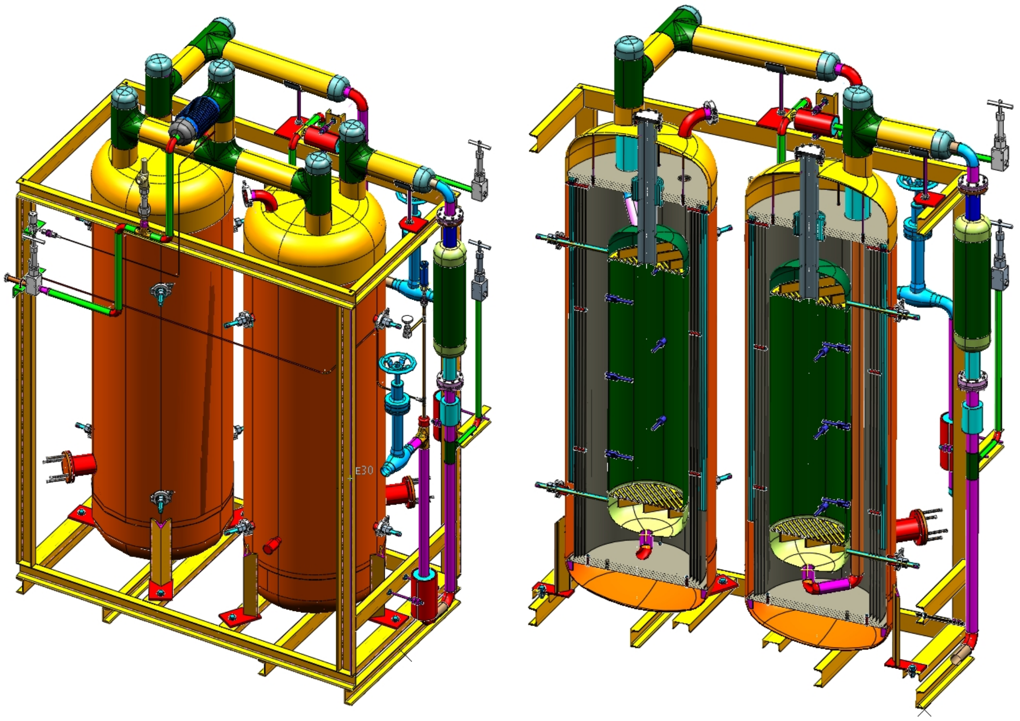

Figure 8: Three-dimensional rendering of a MicroBooNE filter skid. The left drawing shows the full skid, while the right drawing shows a cut-away of the vessels.

washed with distilled water and detergent to remove oil and grease, then cleaned with ethanol. All valves associated with the argon-purification piping utilize a metal seal with respect to ambient air, either through a bellows or a diaphragm, to prevent the diffusion of oxygen and water contamination. The exhaust side of each relief valve is continuously purged with argon gas to prevent diffusion of oxygen and water from ambient air across the o-ring seal. Where possible, ConFlat flanges with copper seals are used on both cryogenic and room-temperature argon piping. Pipe flanges in the system are sealed using spiral-wound graphite gaskets. Smaller connections are made with VCR fittings with stainless steel gaskets.

3.3 Nitrogen Refrigeration

The cryostat and purification systems that contain the liquid argon are subject to heat load from the environment, as well as from the active detectors that have electrical power enabled. To keep these systems operating at a stable temperature and pressure, a liquid nitrogen refrigeration system is present to provide the necessary cooling power. The liquid nitrogen system contains two condensers that are arranged in parallel. One of these is utilized for normal operations and one serves as a backup on standby. Each condenser contains two liquid nitrogen coils, an inner and an outer, with the gas argon on the shell side, as shown in figure 9. Typically only one coil is actively running and the second can be manually activated during situations where the system heat load is higher than usual. Each condenser is sized to handle a heat load of approximately 9.5 kW. With the vessel full of liquid argon and no pump or liquid argon circulation running, the condenser uses 600-650 gallons of liquid nitrogen per day, which equates to a 3.9 kW system heat load. Once liquid argon begins circulating using the pumps, this usage rate will increase by 50-100%.

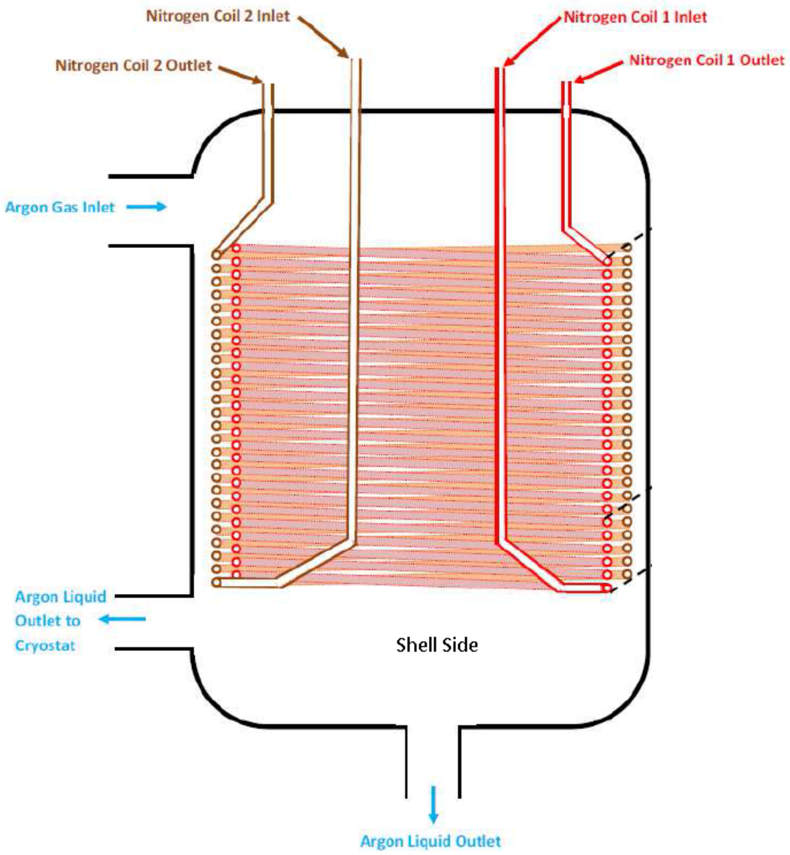

Figure 9: Diagram of a condenser.

3.4 Controls and Purity Monitoring

MicroBooNE makes use of resistive thermal devices (RTDs) to measure temperatures throughout the experimental infrastructure. Twelve RTDs are located along the walls of the cryostat, and another ten RTDs are mounted inside screws attached to the structure of the LArTPC. Each of the filter vessels in the purification system contain nine RTDs. The RTDs within the filter vessels prevent overheating which could potentially occur during filter regeneration with heated argon-hydrogen gas.

Liquid argon contaminations ranging between 300 and 50 ppt oxygen equivalent can be measured using double-gridded ion chambers, henceforth referred to as purity monitors, immersed in liquid argon. The design of the purity monitors is based on the design presented by Carugno et al. [57]. A thorough description of the purity monitors, the data-acquisition hardware and software used in LAPD can be found in [35]. MicroBooNE uses the same type of purity monitors, and the same data-acquisition hardware and software.

A measure of the electronegative impurities is made with the purity monitor by examining the fraction of electrons generated at the purity monitor cathode that subsequently arrive at the purity monitor anode (Q_A/Q_C) after a drift time t. The ratio of (Q_A/Q_C) is related to electron lifetime, τ, such that

$$Q_A/Q_C = e^{-t/\tau}. \tag{3.1}$$

Measurement of liquid argon purity in the MicroBooNE cryogenic system are provided by three purity monitors of varying lengths. One purity monitor with a drift distance of 50 cm sits in a vessel just downstream of the filters and is used to monitor filter effectiveness. Two purity monitors, one with a drift distance of 19 cm and the other with a drift distance of 50 cm, sit within the primary MicroBooNE vessel at each end of the LArTPC.

4. Liquid Argon Time Projection Chamber

The MicroBooNE LArTPC drifts and collects charge to produce fine-grained images of the ionization that is liberated by charged particles traversing a volume of highly-purified liquid argon. This section describes the design and implementation of the LArTPC in the experiment.

The LArTPC is composed of three major structures: the cathode, the field cage, and the anode. A negative voltage is introduced via a feedthrough passing through nozzle N2 on the cryostat and applied at the cathode, which defines an equipotential surface. This cathode voltage is incrementally stepped down in magnitude by means of a voltage divider chain spanning the field cage, creating a region of uniform electric field within the LArTPC. Opposite the cathode, and oriented parallel to it, are the anode wire planes: two induction planes (referred to as the “U" and “V" planes) with wires oriented at ± 60 from vertical, followed by one collection plane (referred to as the “Y" plane) with vertically-oriented wires. The wires of the anode planes are the sensitive elements that detect the ionization created by charged particles traveling through the LArTPC. Figure 10 depicts the assembled MicroBooNE LArTPC after insertion into the cryostat, showing details of the cathode, field cage, and anode plane. Table 5 lists the main parameters of the MicroBooNE LArTPC, which will be described in detail in this section.

4.1 Cathode

The cathode is assembled from 9 individual stainless steel sheets (Type 304, 0.09 inches thick) that are fastened to a supporting frame by hex button head stainless steel screws. The outer edge of the cathode frame consists of round stainless steel tubes of 50.8 mm outer diameter and 3.2 mm wall thickness. Within this outer edge, square tubes with 50.8 mm $\times$ 50.8 mm cross-sectional area, and 3.2 mm wall thickness, are fastened together with button head screws, forming a support structure upon which the cathode sheets are attached. The individual components of the support structure are further welded together to eliminate sharp features from this high-potential surface. The exterior frame and support structure of the cathode are shown in figure 11 and a view of the interior is shown in figure 12. The cathode plane sheets are shimmed according to survey data to make the cathode as flat and as parallel to the anode frame as possible. Flatness of the cathode is evaluated relative to a best fit plane of survey data (more than 10000 survey points recorded with a laser tracker). The

Table 5: MicroBooNE LArTPC design parameters and nominal operating conditions.

Parameter	Value
LArTPC (active) dimensions ($h \times w \times l$)	2.325 m $\times$ 2.560 m $\times$ 10.368 m
LArTPC (active) mass	90 tons
# Anode planes	3
Anode planes spacing	3 mm
Wire pitch	3 mm
Wire type	SS, diam. 150 μm
Wire coating	2μm Cu, 0.1μm Ag
# wires (total)	8256
# Induction0 plane (U) wires	2400
# Induction1 plane (V) wires	2400
# Collection plane (Y) wires	3456
Wire orientation (w.r.t. vertical)	+60°,-60°,0° (U,V,Y)
Cathode voltage (nominal)	-128 kV
Bias voltages (U,V,Y)	-200 V, 0 V, +440 V
Drift-field	500 V/cm
U-V gap field	666.7 V/cm
V-Y gap field	1466.7 V/cm
Max. Drift Time, Cathode to U (at 500 V/cm)	1.6 ms
# Field-cage steps	64
Ring-to-ring voltage step	2.0 kV

largest deviations of the cathode from the best fit plane are +6.6mm and -6.5mm. Approximately 55% of the measured survey points fall within +/-3mm of the best fit plane, and more than 90% of the points fall within $\pm$5 mm. Figure 13 shows the results of the survey, with deviations from flat represented as color-coded data extending away from the nominal plane of an ideal cathode.

4.2 Field Cage

The field cage encloses the volume between the cathode plane and the anode wire planes, and in doing so creates a region with a uniform electric field. The volume defined by the interior of the field cage, bounded by the anode and cathode planes, is referred to as the “active" volume. The field cage structure consists of 64 individual thin-walled stainless steel tubes (1.0 inch OD, 0.065 inch wall thickness), each shaped into a rectangular loop framing the perimeter of the active volume. These 64 loops are mounted parallel to the cathode and anode planes, as shown in figures 11 and 12, and are held in place by a G-10 rib support structure. Each field cage loop is electrically connected to its neighbors via a resistor divider chain (described in following section), causing each loop to operate at a different electrical potential which in turn maintains a uniform electric field between the cathode and anode planes. For a nominal -128 kV cathode voltage, the difference in potential between adjacent field cage loops is 2 kV, ramping down the total potential in equidistant steps from cathode to anode. The distance from center-to-center of adjacent field cage loops is 1.575 inches.

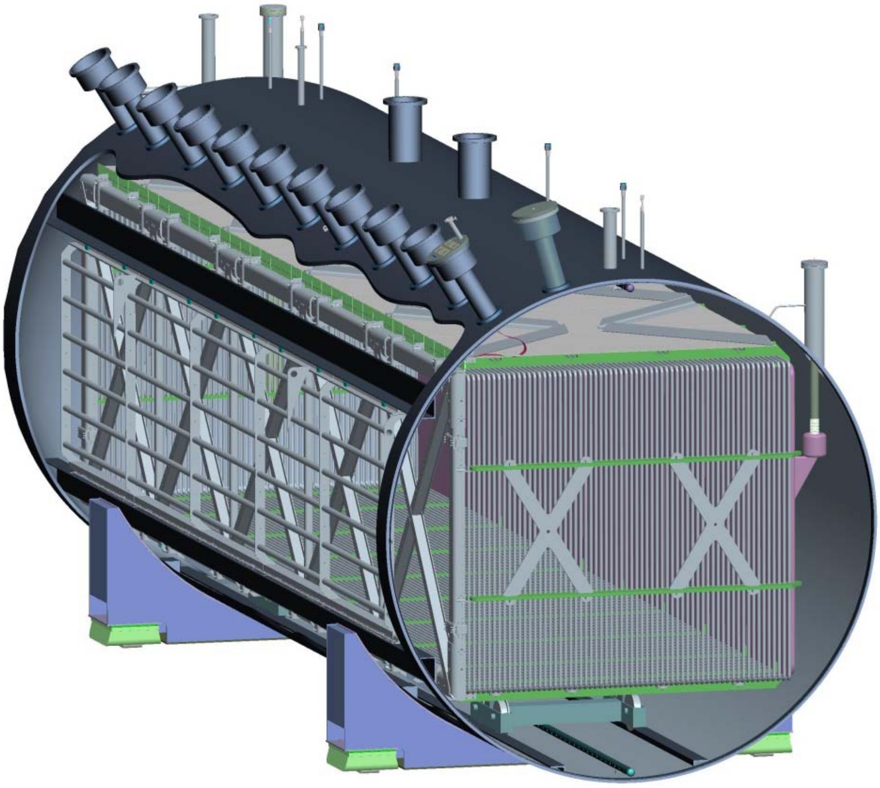

Figure 10: Schematic diagram of the MicroBooNE LArTPC , depicted as it is arranged inside the cryostat.

Figure 11: Exterior view showing the cathode frame and structural supports to which cathode sheets are fastened.

Each field cage loop is assembled from 6.77 feet long vertical pipes on the upstream and downstream ends of the LArTPC , and on the top and bottom from two 17 feet long horizontal pipes connected by a stainless steel coupling in the center. Each tube has venting holes approximately

Figure 12: Interior view of cathode plane as viewed from the upstream end of the LArTPC , showing cathode sheets.

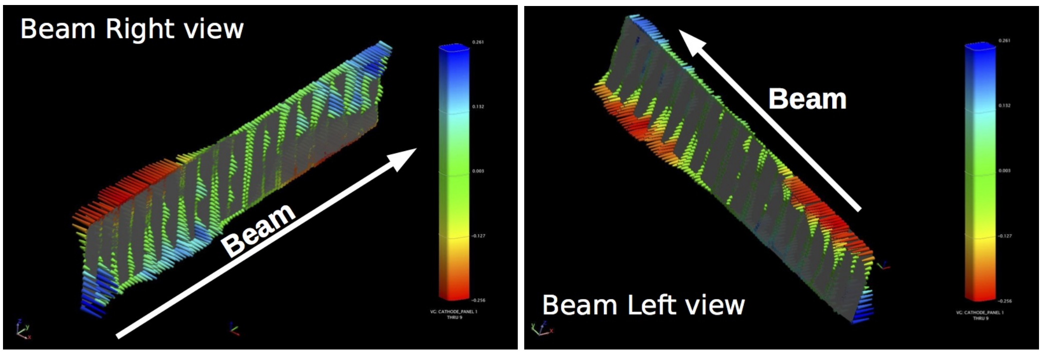

Figure 13: Survey results for interior (left) and exterior (right) of the cathode after shimming.

every 6 inches so that they fill with liquid argon and allow air and gaseous argon to escape during cryostat cool down and filling.

The four corners of each field cage loop are curved with a radius of 2.0625 inch. Each corner is formed by three parts: two couplings and an elbow, shown in figure 14. The couplings make the connections between the pipes and the elbow. The thin-walled tubes and elbows slip-fit over the ends of the couplings with a 0.88-inch overlap. Each coupling has two 6-32 NC tapped holes and the connections to the adjoining pieces are made by hex head button screws and lock washers.

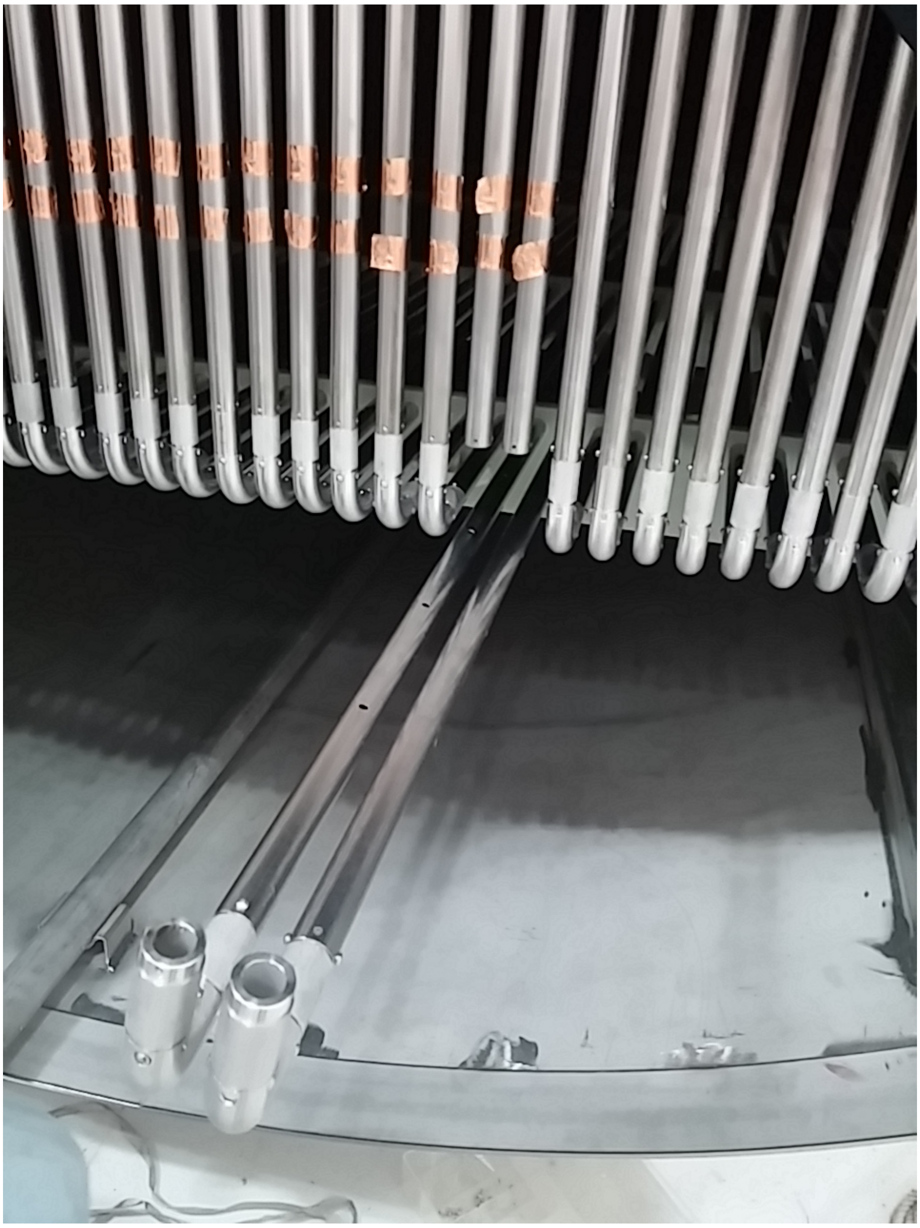

Figure 14: Field cage loops, with two partially disassembled to show elbow and couplings.

In order to avoid electrical breakdown between the inner cryostat surface and field cage parts at high potential on or near the cathode, the electric field strength is minimized at the corners and edges of the field cage. Loop 0 is the cathode frame, which is at the same potential as the cathode plane sheets attached to it. The frame is made from larger diameter piping of 2 inch OD, and it has a slightly smaller circumference than the other field cage loops, as shown in figure 15. The elbow of loop 1 has a specially designed shape in order to minimize the electric field potential, and the elbow of loop 2 has a softer radius of curvature than the standard elbows. For all three of these loops (loop 0, 1, and 2), connections at corners and joints are made by welding instead of screws to avoid sharp edges that would result in higher electric fields and greater chance of electrical breakdown.

Figure 15: Field cage loops closest to (and including) the cathode are modified to reduce sharp edges that would result in higher electric fields.

Another precaution to minimize the electrical field between the loops and the cryostat surface is the positioning of the coupling screws: for the first 20 loops, the screws are positioned on the sides facing the screws of the neighboring loops instead of facing inward to the LArTPC active volume and outward toward the grounded cryostat surface. Hex head button screws and lock washers are also used here in order to minimize sharp metal edges.

4.2.1 Resistor Divider Chain

A resistor divider chain installed across the field cage loops steps the voltage down in magnitude from the cathode plane to the anode wire plane in equidistant steps. 63 of the 64 loops between the cathode plane and the anode wire plane are electrically isolated. For a nominal value of -128 kV on the cathode, this results in a potential difference of 2 kV between each pair of loops. The value of the equivalent resistance between loops within the divider chain was chosen to be low enough such that the current flow through the divider circuit is much greater than the signal current flowing through the LArTPC . The signal current in this case is the total energy deposited by cosmic rays, and is estimated to be <50 nA. An equivalent resistance of 250 MΩ between each pair of field cage loops, corresponding to a current flow of 8 μA, was chosen.

The voltage divider chain is mounted on the inside of the field cage at the upstream end of the detector. The couplings at the top corner of each field cage loop have additional holes facing the inside of the field cage, where the resistors are mounted. On the first 16 field cage loops, pairs of Metallux HVR 969.23 499 MΩ resistors (rated to 23 W, 48 kV in air) are mounted electrically in parallel to establish the beginning of the voltage divider chain. On the remaining loops, thick-film Ohmite Slim-Mox 104E metal-oxide epoxy-coated resistors with a lower power and voltage rating (1.5 W, 10 kV in air) are used. Extensive testing was done on these two types of resistors [58]. For redundancy, the desired 250 MΩ total resistance between each pair of field cage loops is composed of four individual 1 GΩ Slim-Mox 104E resistors placed electrically in parallel and attached to a printed circuit board. Printed circuit boards span across eight field cage gaps and therefore have eight 250 MΩ resistances in series, shown in figure 16. The electrical connection between the boards and each field cage loop is made by metal contact pads on the back side of the boards, held in electrical contact with the field cage tube by a button-head hex screw and lock washer.

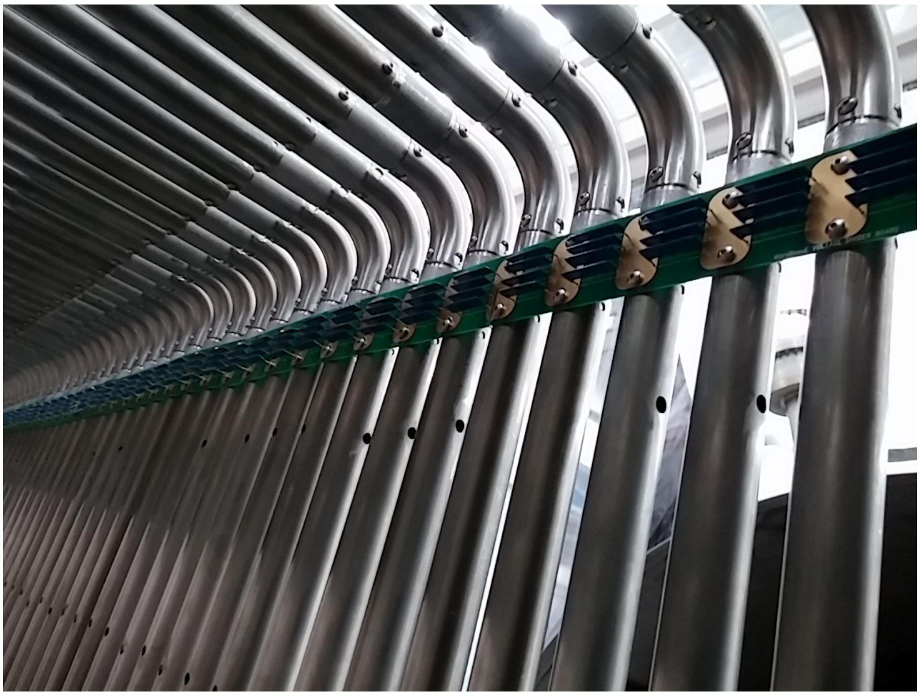

Figure 16: The Ohmite Slim-Mox 104E resistors arranged in parallel sets of four on printed circuit boards that span eight field cage tubes.

While the designed operating voltage difference across each resistor in the detector is 2 kV with a power flow of 4 mW, there is a slight possibility that these values could temporarily exceed the rating of the resistors in the case of discharge between the cathode plane or field cage loops and the cryostat wall, through the bulk liquid argon. Recent studies [59] have shown that the value of the minimum breakdown electrical field decreases with the increasing argon purity; for purities as high as that required in the MicroBooNE detector, breakdown has been observed at electric fields as low as 40 kV/cm.

The field cage behaves like a capacitance network. Based on measurements and simulations, the total energy stored inside the field cage when fully charged is estimated to be approximately 24 J. In the case of a discharge between the cryostat and the cathode or one of the field cage loops close to the cathode, simulations show that voltages of up to 80 kV can develop across the resistors over the timescale of a few seconds. The observed peak voltages in such discharge scenarios decrease the further the breakdown occurs from the cathode, such that discharges occurring between the cryostat and field cage loops 32 through 63 do not exceed the 10 kV rating of the resistors.

In order to protect the Ohmite Slim-Mox 104E resistors near the cathode from damage, two strategies have been implemented. First, as previously mentioned, on the first 16 field cage loops near the cathode the Ohmite Slim-Mox 104E resistors are replaced by 499 MΩ Metallux HVR 969.23 resistors that have a higher voltage rating of 48 kV. An extensive study of resistor breakdown in liquid argon of several resistor brands and models [58] has revealed that the breakdown voltage observed in liquid argon exceeds the rating in air substantially for all resistors. No breakdown has been observed up to 32 kV for the Ohmite Slim-Mox 104E resistor. For the Metallux HVR 969.23 resistors, no breakdown has been observed up to the limit of the test apparatus of 130 kV. Since the Metallux HVR 969.23 resistors are significantly larger physically than the loop-to-loop distance, they are mounted diagonally between each pair of field cage loops. They are held by copper brackets, which are attached to studs welded onto the field cage tubes, shown in figure 17.

The second type of protection installed for all resistors on field cage loops 1 through 32 is a surge protection circuit. The chosen surge protection devices are designed to short the circuit in the case of a voltage spike, which protects any other electrical components installed in parallel. Below their clamping voltage, they exhibit a very high resistance and do not influence the circuit. The behavior of Gas Discharge Tubes (GDTs) and varistors in liquid argon has been studied extensively for application in the MicroBooNE field cage [60]. The surge protection device chosen is a Panasonic ERZ-V14D182 varistor with a clamping voltage of 1700V. In order to obtain a very high resistance in normal operation and a clamping voltage above the 2 kV in normal operation mode, three of these devices are mounted in series across a block of four Slim-Mox 104E or two Metallux 969.23 resistors. These additional varistor boards make electrical contact with the field cage via brass mounting brackets that are fastened to the field cage with button head screws, as shown in figure 18.

4.3 Anode

The anode frame holds the induction and collection plane sense wires at tension and provides overall structural support for the beam-right side of the LArTPC. Individual sense wires for all anode planes are held in place by wire carrier boards, which are printed circuit board assemblies

Figure 17: The Metallux HVR 969.23 resistors mounted on the 16 field cage loops closest to the cathode.

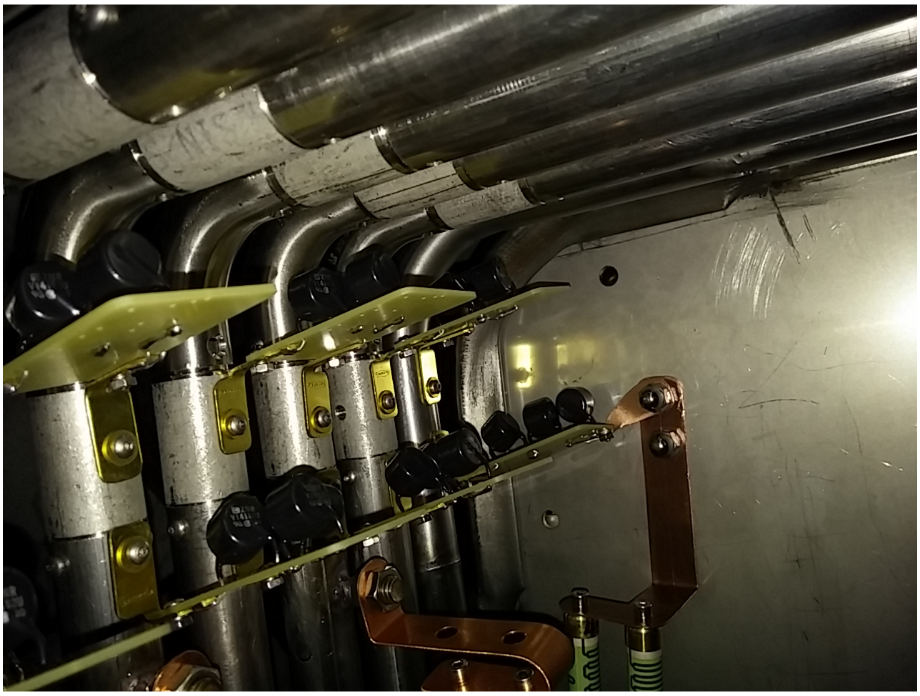

Figure 18: Surge-protecting varistors are installed in parallel with the voltage divider resistors for the first 32 field cage loops. Here, they are shown mounted on small boards in sets of 3, and attached to the field cage by means of 6-32 hex button head screws.

that locate the wires as well as provide the electrical connection to the electronic readout system of the experiment.

4.3.1 Mechanical structure

The anode frame is comprised of a stainless steel C-channel hosting adjustable tensioning bars to which the wire carrier boards are attached. The C-channel and tensioning bar assembly is depicted for one corner of the anode frame in figure 19. Wire carrier boards attach to precision alignment pins distributed along the length of the tensioning bars.

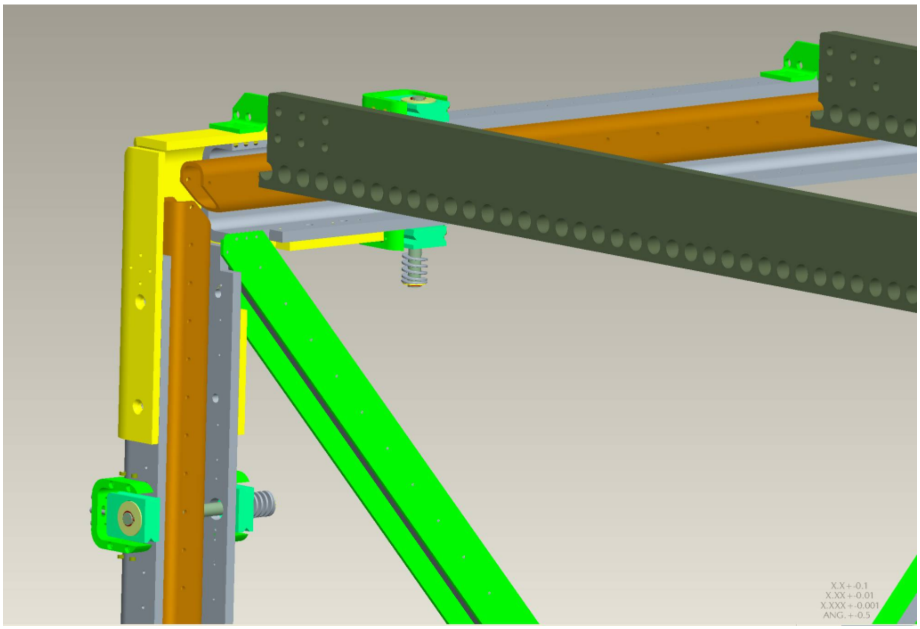

Figure 19: Rendering of the anode frame assembly. The C-channel is depicted in gray, and the adjustable tensioning bar assembly is shown in orange.

4.3.2 Wire winding and quality assurance

The three anode planes are constructed from wire carrier boards that have had individually-prepared wires attached to them in groups of 16 (for the U- and V- angled planes) or 32 (for the vertical Y-plane). Consistent quality in wire preparation was achieved by a semi-automated winding machine, which terminated the ends of each wire via wrapping around 3 mm diameter brass ferrules as shown in figure 20. Each wire was tested for strength by being placed on a tensioning stand where a load of 2.5 kg (more than 3 times the nominal load of 0.7 kg) was applied for 10 minutes, ensuring that the wire preparation did not leave any weaknesses that could result in a breakage later on. Upon successful completion of the quality assurance testing for each wire, it was placed onto a wire carrier board, shown in figure 21

When installed, the wires make contact with gold pins positioned on the wire carrier board, and these pins are connected to a trace that routes to the cold electronics described in section 6.1. After fully filling a wire carrier board with wires, a cover plate was installed and press-fit rivets were installed to hold the assembly together. The assembled wire carrier board was then placed

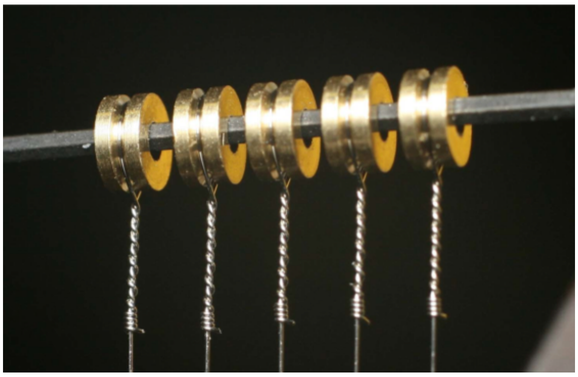

Figure 20: Picture of the wire termination on the brass ferrules. Each ferrule is 3 mm in diameter, and 1.5 mm thick.

onto a tension stand, to reapply a 2.5 kg tension/wire to the whole board for 10 minutes. This is to ensure that the wires were not weakened during the board assembly process. The tension stand is depicted in figure 22. A comprehensive description of the MicroBooNE wire preparation and associated quality assurance studies can be found in [61].

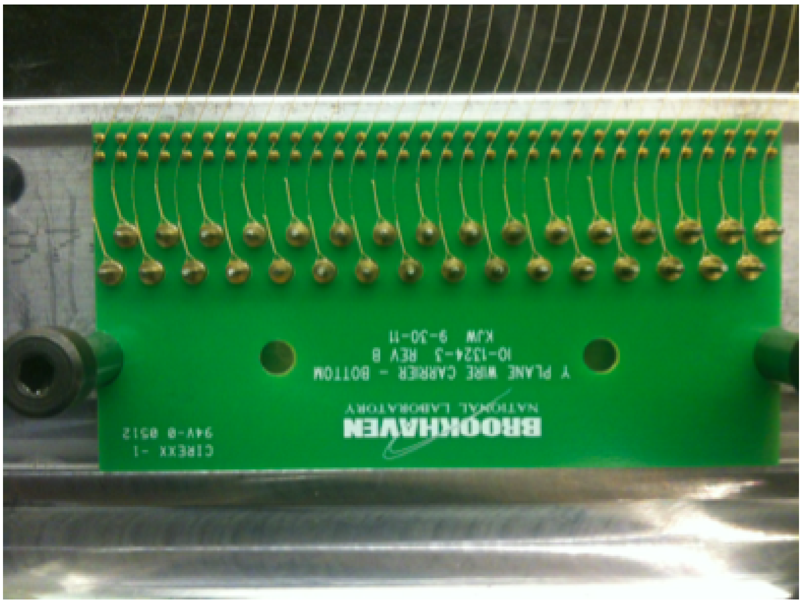

Figure 21: Picture of a collection plane wire carrier board that has been filled with wires, but has not yet had cover plate installed.

4.3.3 Wire installation and tension measurements

During detector construction the completed wire carrier assemblies were manually installed onto the adjustable tensioning bars residing in the C-channel of the supporting anode frame. A team of two people installed each assembly (consisting of wires and supporting carrier boards on either end) onto the anode frame. The collection plane was the first installed, followed by the middle induction plane, and then finally the inner induction plane. Once all three anode planes were

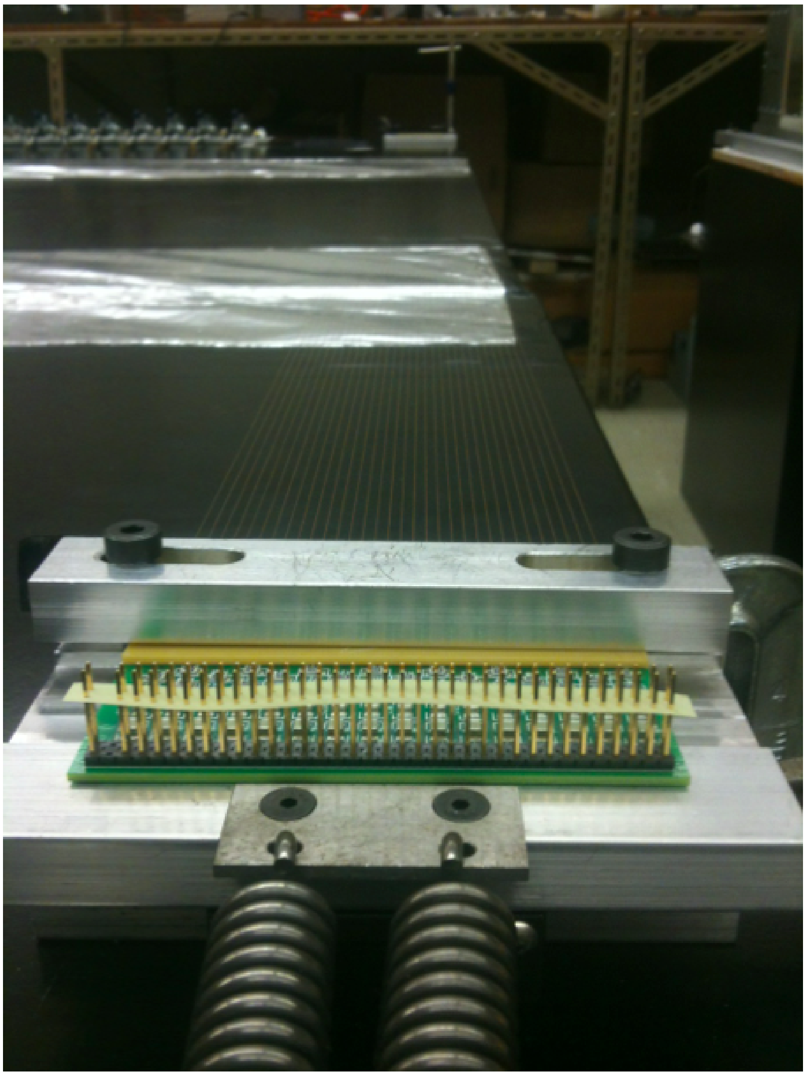

Figure 22: Picture of a collection plane wire carrier board on the tension stand.

completely installed, the tensioning bars were adjusted and a survey was taken of the tension of all anode wires. Tension was measured via measuring the resonant frequency of a laser beam reflected off of a plucked wire and incident on a photodiode connected to a spectrum analyzer program [62]. The tension measuring equipment was developed and produced by the University of Wisconsin Physical Sciences Laboratory. The tensioning bars were adjusted iteratively until the surveyed tension of all wires was within a range where no single wire was too taught or loose to create detector performance issues. Figure 23 shows the final surveyed tension of the wires within the LArTPC.

4.4 Parts Preparation

The majority of the parts that make up the LArTPC are either stainless steel or G-10. These two material types, as well as any others used in the LArTPC, were tested in the Fermilab Materials Test Stand (MTS) [36], whose purpose was to investigate the suitability of materials for use in

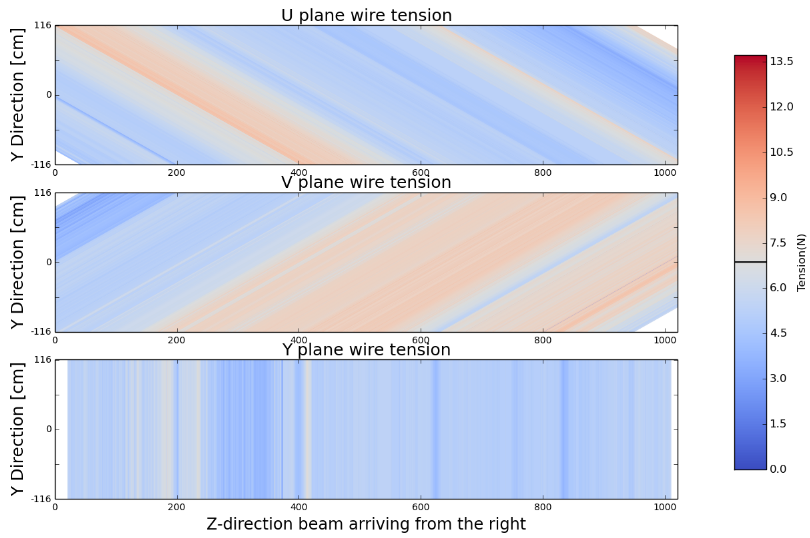

Figure 23: Final survey results for wire tension of the MicroBooNE LArTPC.

LArTPCs. The MTS confirmed that none of the materials used in the LArTPC assembly would contaminate the liquid argon. Before assembly, all LArTPC parts were cleaned according to the procedures described in the following sections.

4.4.1 Cleaning stainless steel

The delivered stainless steel parts were often greasy due to machining, and those with holes or interior cavities generally had a significant amount of trapped metal shavings due to the machining processes. Many of the pieces also had markings from permanent ink pens, dirt smears, rust spots, and/or dried oil from machining. These pieces were scrubbed with ScotchBrite 7447 general-purpose hand pads before cleaning.

Parts that were small enough to fit in an ultrasonic bath were prepared according to the following prescription. A pre-rinse with tap water was performed to remove particulate matter, followed by deburring of sharp edges. The first ultrasonic wash was 15 minutes in heated distilled water with a 3% solution of Citranox acid detergent [63]. After a first rinse in distilled water, a second ultrasonic wash was performed, again for 15 minutes, but using heated distilled water with a weak solution of Simple Green detergent [64]. A second rinse in distilled water was performed, followed by a final rinse in a fresh bath of distilled water. The parts were then wiped dry with lint-free cloths, air dried completely, and wrapped in plastic film for storage.

Stainless steel parts which were too large to fit in the ultrasonic bath were prepared by a simpler prescription out of necessity. A pre-rinse with tap water was followed by deburring to remove sharp edges. Both the first and second washes were done with tap water and a weak solution of Simple Green detergent, scrubbing with brushes and lint-free sponges. Two tap water rinses were done, and the parts were then wiped dry with lint-free cloths. As a final additional step, each part was wiped with 200-proof ethyl alcohol, and then air dried completely. These parts were also wrapped in plastic film for storage.

4.4.2 Cleaning G-10

G-10 is known to absorb large quantities of water, which would outgas in the argon and could inhibit reaching the required argon purity in the detector. For this reason all G-10 parts were cleaned and then baked to remove moisture. The largest G-10 parts on the detector are beams that span the distance between the cathode and anode. These were washed in 500-gallon ultrasonic baths that are overseen by Fermilab Accelerator Division, typically used for cleaning large sections of accelerator beam pipes. An initial pre-wash was done with tap water to remove as much particulate matter as possible, since the machining process left a large amount of dust on the machined edges. Pieces were then placed in the ultrasonic bath with heated deionized water and a 2% solution of Elma Clean 65 (EC 65) neutral cleanser [65]. Two ultrasonic bath rinses were performed, and the pieces were then sealed in plastic bags with clean dry nitrogen gas. In order to remove the absorbed water, the large G-10 parts were then transported to Fermilab Technical Division where they underwent an outgassing procedure to remove any remaining absorbed moisture. They were baked in a large oven under vacuum until a plateau in the outgassing was reached, as reported by a monitor inside the oven. Upon completion of the outgassing procedure, the parts were resealed in plastic bags for storage.

4.5 Assembly

The full mechanical structure of the LArTPC is shown in figure 24, with the top image depicting the cathode frame on the left, made semi-transparent to show the support structures on which the cathode sheets are attached. The anode frame is on the right of this image, with I-beams configured in a crossed pattern to maintain the shape and rigidity of the outer C-channel structure. Ribs of G-10 connect the anode and cathode, electrically isolating them from each other while also providing mounting holes to hold in place each of 64 field cage loops that define the active volume of the LArTPC . The field cage loops are visible in the photograph in the bottom frame of figure 24.

Assembly was done inside of a clean tent, shown in figure 25, on a flat surface made up of adjustable-height metal platforms that were installed on the assembly room floor. These platforms were leveled to better than 0.5 mm before beginning assembly. The anode frame was the first part of the detector to be assembled on this surface, shown in figure 26. It was temporarily placed aside, and the cathode frame was assembled on the same set of platforms along with the G-10 ribs, which stood vertically with the help of temporary unistrut support pieces. The combined cathode and G-10 frame was then lifted and rotated to the proper orientation, with G-10 ribs extending horizontally from the cathode to the anode, as shown in figure 27. Finally, the anode frame was brought back over and attached to the G-10 ribs, and the stainless steel tubes that make up the field cage loops were fed through the holes in the G-10 ribs to complete the mechanical structure of the LArTPC .

4.6 High Voltage System

To create the drift electric field, an adjustable negative voltage (referred to as the “high-voltage" or “HV") is supplied to the LArTPC cathode, generated outside of the cryostat by a Glassman LX150N12 power supply. Before entering the cryostat, the output of the power supply is passed through a current-limiting resistor series that serves as both a low-pass filter for the power supply

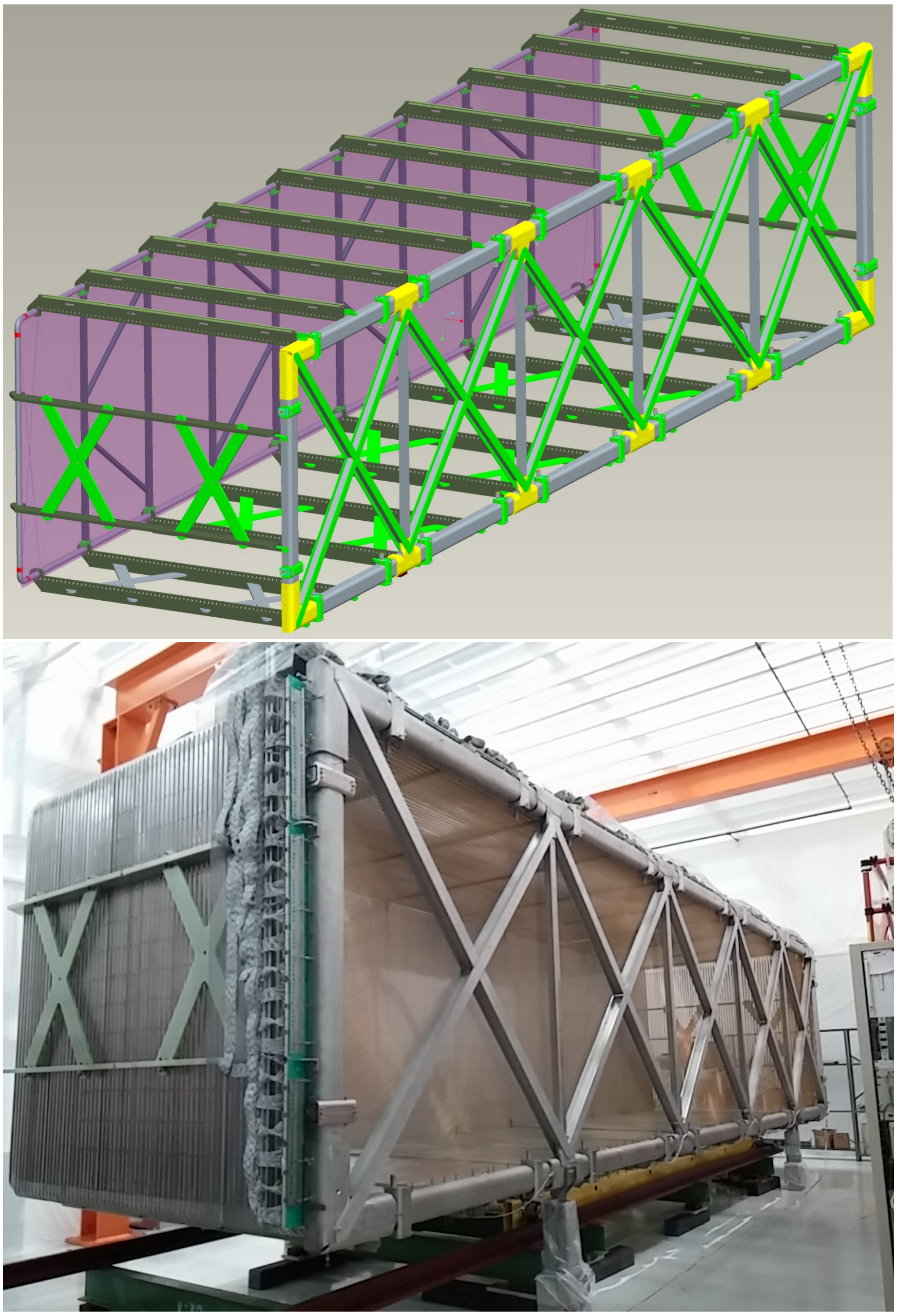

Figure 24: Top: Rendering of the full LArTPC frame assembly. Bottom: Assembled LArTPC after wire and electronics installation.

ripple, and a stored energy partition in case of a sudden reduction in voltage. The resistor series is a set of eight 10 MΩ resistors submerged in a transformer oil in an aluminum container. This assembly was successfully tested to -200 kV. The capacitance of the cable is $\sim$50 pF/m making the time constant of the component upstream of the LArTPC $\sim$35 ms.

The potential is introduced into the cryostat by a custom-designed HV feedthrough. The

Figure 25: Clean tent where MicroBooNE LArTPC assembly was conducted.

Figure 26: Anode frame in the process of being moved from the metal assembly platforms.

feedthrough is based on an ICARUS design [13]; an inner 1.0 in diameter stainless steel conductor carrying the HV is surrounded by an insulating tube, 2.0 in outer diameter and 1.0 in inner diameter, of ultra-high molecular weight polyethylene (UHMW PE), which is further encased in an outer

Figure 27: Cathode frame and G-10 ribs on metal assembly platforms.

ground tube. A photograph and drawing of the production feedthrough are shown in figure 28.

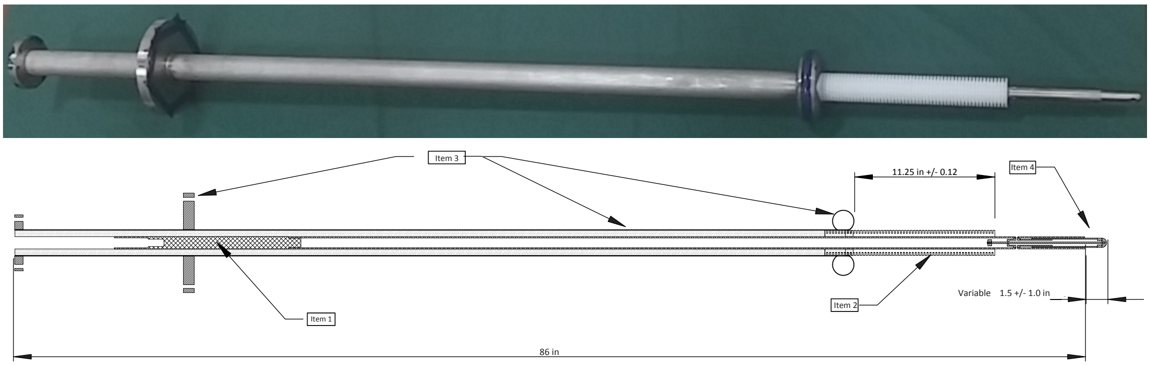

Figure 28: Photograph and drawing of the production HV feedthrough. The spherical probe tip is attached to the end of the inner conductor, on the right side of these figures.

MicroBooNE's voltage target combined with its geometry of a cylindrical cryostat with a single drift region necessitate that the HV feedthrough extend deeper into the cryostat than the ICARUS feedthrough to avoid high field regions. Figure 29 shows the HV feedthrough extending into its receptacle cup attached to the LArTPC cathode. The lower termination of the outer ground tube is a torus chosen to reduce the electric field between both the feedthrough and the cathode plane and along the feedthrough itself. The length of exposed UHMW PE is machined with grooves in an effort to improve performance. The electrical connection to the cathode is accomplished with a hemispherical spring-loaded tip attached to the inner conductor of the feedthrough. When the feedthrough is installed on the cryostat, the spring-loaded tip makes contact with the receptacle cup attached to the cathode.

Figure 29: The production HV feedthrough inserted into the cathode receptacle cup inside the cryostat.

5. Light Collection System

Liquid argon is a very bright scintillator, and collecting the light produced when charged particles travel through the LArTPC is critical aspect of fully understanding the interactions taking place in the detector. The light collection system is designed to meet MicroBooNE's physics goals for light collection, which are twofold. First, for accelerator-induced events, the light collection system is designed to trigger on 40 MeV kinetic energy protons produced in neutrino interactions. Second, for non-beam events, the system is designed for efficient observation of 5 to 10 MeV electrons from supernova neutrinos.

The light produced by neutrino interactions in MicroBooNE is an important input for both event selection and reconstruction. One of the critical capabilities the light collection system provides is the ability to form a beam-event trigger when a pulse of light is observed in coincidence with the beam spill. Because a vast majority of beam spills will not produce a neutrino interaction in the detector, such a trigger will substantially reduce the data output rate. For non-beam physics studies, the light system provides triggering and an event interaction time (t_0). For accelerator-induced events, the start time of a beam spill is, in principle, sufficient. However, because of the long window over which the ionization electrons of an event drift (about 1.6 ms maximum drift time at 500 V/cm field), there are many accelerator-induced events in which a cosmic ray muon crosses the detector during the drift time. Utilizing the position of hits in the photodetectors, one can better reject cosmic ray muon tracks. The light can also be used to trigger and select specific types of cosmic-ray calibration events (Michel electrons, straight-through muons, etc.) and non-beam events (supernova neutrinos, cosmic background events to proton decay studies, etc.).

The light collection system consists of primary and secondary sub-systems. The primary light collection system is made up of “optical units", each one consisting of a PMT located behind a wavelength-shifting plate. In total, 32 optical units were installed, yielding 0.85% photocathode coverage. The secondary system consists of four light guide paddles. These paddles are introduced for R&D studies for future LArTPCs, and are placed near the primary optical units to allow a comparison of their performances. A flasher system, used for calibration, consists of optical fibers bringing visible light from an LED to each PMT face.

The light collection detectors are located in the *y*-*z* plane behind the anode planes of the LArTPC, as shown in figure 30. The combined transparency of the three anode planes is 86% for light at normal incidence. This transparency value assumes 100% of VUV photons impinging on the wires (150 μm diameter and 3 mm pitch) are absorbed. The detectors were placed so as not to be obscured by the LArTPC structural cross-bars, shown in figure 30. Locating the light detectors behind the anode plane places them in a very weak electric field due to the +440 V bias of the collection plane. To test for an effect from weak electric fields, the response of a PMT placed between a +700 V mesh and ground, separated by 50 cm, was studied. The PMT zenith was 25 cm from the HV. No effects on the signal were observed. This was expected, as the photocathode is held at ground, effectively acting as a Faraday cage.

Throughout the design and construction of the light collection system, substantial R&D was performed. The reader should refer to [52, 66 – 77] for detailed results of these studies. A useful overall review is available in [78].

Figure 31 shows the light observed in two sequential events, consistent with a muon entering the detector followed by a Michel electron from the decay. One can see that the light is relatively well localized. This allows the light to be correlated with specific tracks in the detector. This “flash-track matching” is used to identify and reconstruct the tracks that are in time with the beam spill–an important goal of the light collection system.

5.1 Light Production in Argon

Light produced in liquid argon arises from two processes: scintillation and Cherenkov radiation. Scintillation light is produced by the formation and eventual radiative decay of excited argon dimers (or eximers) and is emitted in an isotropic distribution. Liquid argon is an excellent scintillator: it produces a large amount of light per unit energy deposited (about 40,000 per MeV at no drift field) and is transparent to its own scintillation. The scintillation light has a prompt and slow component with decay times of about 6 ns and 1.6 μs, respectively. The two lifetimes correspond to the two

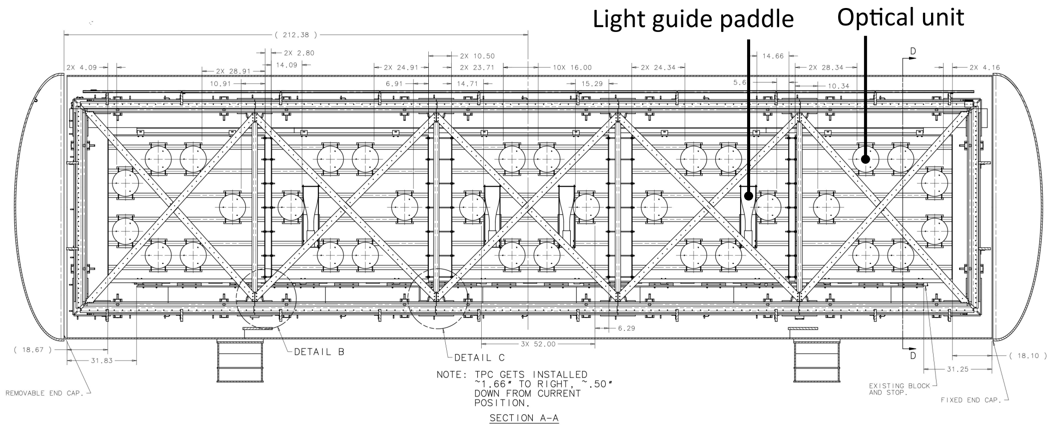

Figure 30: The MicroBooNE light collection system consists of a primary system of 32 optical units and a secondary optical system of four lightguide paddles [72]. These are mounted behind the anode wire planes such that the view is not obscured by structural cross bars of the LArTPC.

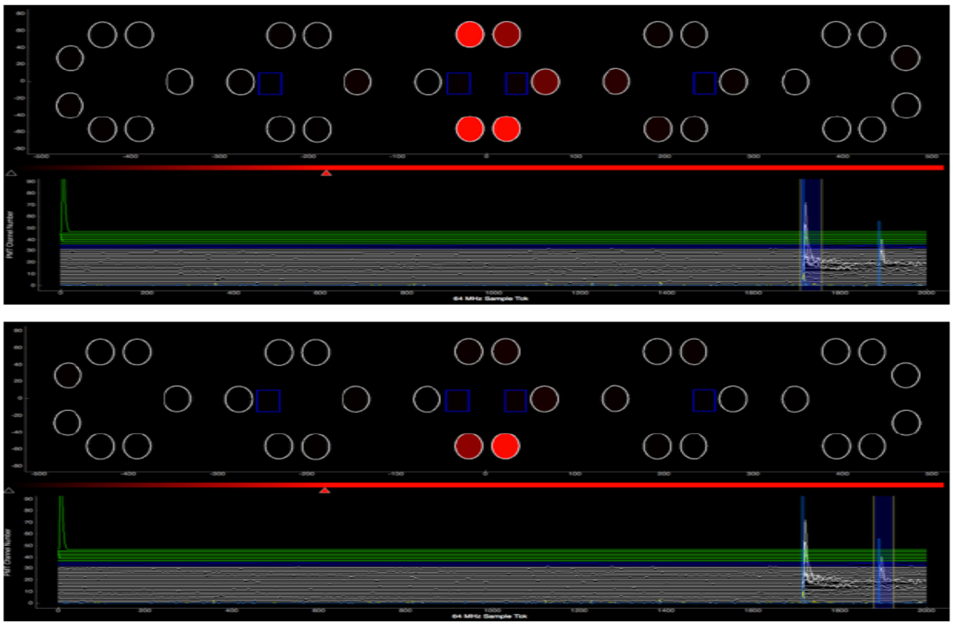

Figure 31: Two sequential event displays for the light collection system. The sequence is consistent with a muon that stops (top) and decays (bottom). The circles correspond to the optical units. Red circles indicate those units with hits. The waveforms versus time are shown below.

Table 6: Important properties of scintillation light in liquid argon that affect detection in MicroBooNE.

Property	Value	Reference
Wavelength	128 nm	[79]
Singlet, Triplet state time constants	6 ns, 1.6 μs	[80]
Photons/MeV for $E = 500$ V/cm	24000	[13]
Triplet lifetime quench due to N_2 at 1 ppm	20%	[81]
Attenuation length due to N_2 at 1 ppm	66 m	[52]
Rayleigh Scattering Length	$\sim$90 cm	[82]
Transparency of the wireplanes at normal incidence	86%	-

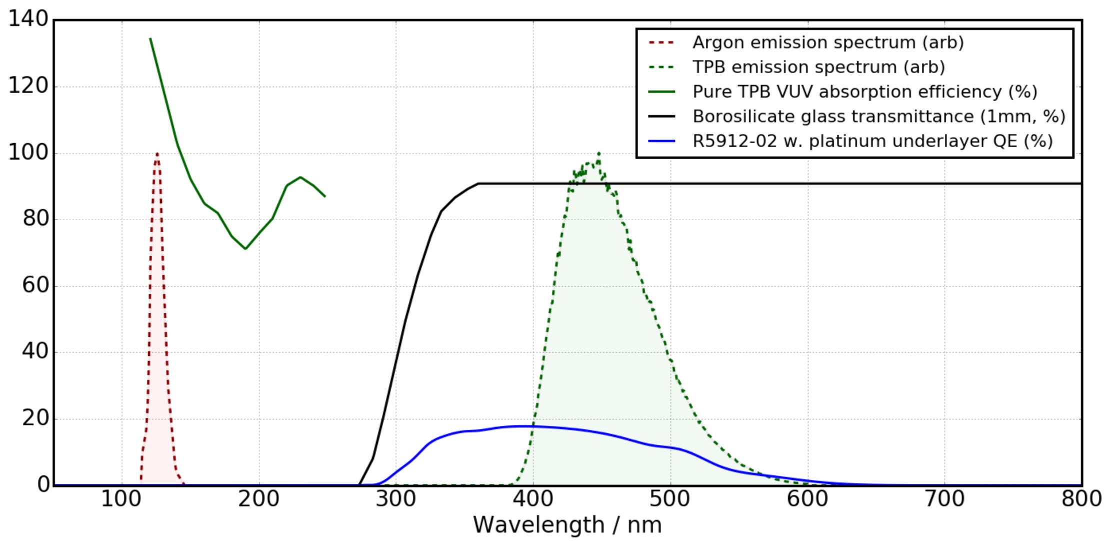

Figure 32: Scintillation light emission spectrum (red) and TPB re-emission spectrum (green), in arbitary units. Superimposed are important efficiencies (see y axis): Dark green line – absorption of VUV light by TPB; Black line – transmission of borosilicate glass; Blue line – efficiency of a R5912-02mod cryogenic PMT [78]

lowest-lying eximer states with the prompt component coming from the decay of a singlet state and the slow from the decay of a triplet state. The prompt to slow ratio is about 1:3 for minimum ionizing particles and varies with ionization density and particle type. Both components consist of photons with a wavelength of 128 nm.

There is a significant uncertainty on the expected triplet lifetime [80] and this may be further modified by quenching (non-radiative dissociation of excimers by impurities) [81]. Other factors that can affect the arrival of the light include Rayleigh scattering, absorption by impurities, and obstructions. For detailed discussion of the physics of scintillation light production and propagation in MicroBooNE, see [78]. Table 6 summarizes information about the scintillation light.

Because scintillation photons have a wavelength of 128 nm they are are very difficult to detect using conventional photodetectors. Figure 32 summarizes the challenges involved in detection of

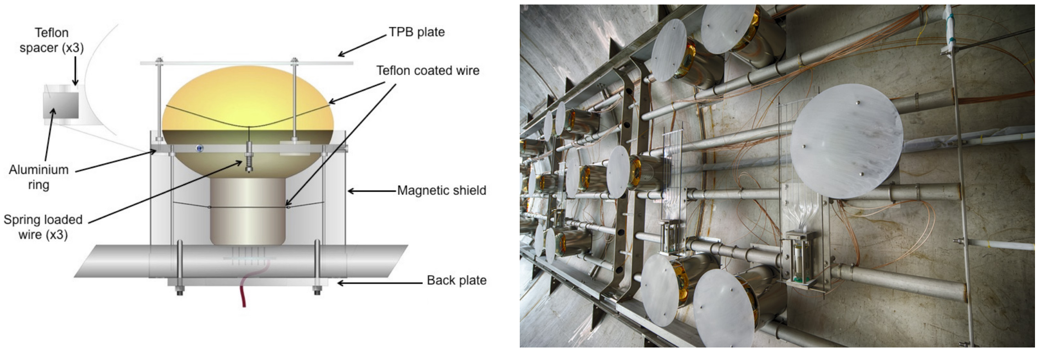

Figure 33: Left: diagram of the optical unit; Right: units mounted in MicroBooNE, immediately prior to LArTPC installation.

the 128 nm scintillation light. In order to detect the scintillation light, with spectrum shown in red, the VUV photons must be shifted into the visible region. MicroBooNE employs tetraphenyl-butadiene (TPB). This organic fluor absorbs in the UV (green line) and emits in the visible with a peak at 425 ± 20 nm (green hatched region), the peak wavelength having a slight dependence on the micro-environment of the fluors. This is a favorable wavelength for detection by the photomultiplier tubes (PMTs) employed by MicroBooNE. The efficiency for transmission through borosilicate PMT glass (black) and the quantum efficiency of the cryogenic tubes used in MicroBooNE (blue) are overlaid on the TPB spectrum.

5.2 The Primary Light Collection System

Each of the 32 optical units of the primary light collection system consist of a cryogenic Hamamatsu 5912-02MOD PMT seated behind an acrylic plate coated with a TPB-rich layer and surrounded by a mu-metal shield. Figure 33 shows a diagram of one unit (left) and a photograph of installed units (right). Past experiments have directly coated PMTs with wavelength shifter [13]. However, the MicroBooNE design separates the PMT from the wavelength-shifting plate for simplicity of quality control and installation. This proved important, as R&D indicated that TPB is particularly vulnerable to environmental degradation (see section 5.2.3). In this section, description is provided for each component of the optical unit, as well as for the overall assembly.

5.2.1 Photomultiplier Tubes and Bases

Reference [70] provides detailed information on the selection and testing of the 8" Hamamatsu R5912-02mod cryogenic PMTs employed in MicroBooNE. In this section a brief summary of the findings from this testing is presented.

The R5912-02mod employs a bi-alkali photocathode. Because the PMT is designed for cryogenic use, the R5912-02mod also features a thin platinum layer between the photocathode and the borosilicate glass envelope to preserve the conductance at low temperatures. While this allows the PMT to function below 150 K, absorption in the platinum reduces the efficiency of the PMT by 20%. Figure 34 provides quantum efficiency curves for the 8 inch photomultiplier tubes. The manufacturer's specifications do not include the effects of the platinum photocathode coating, but

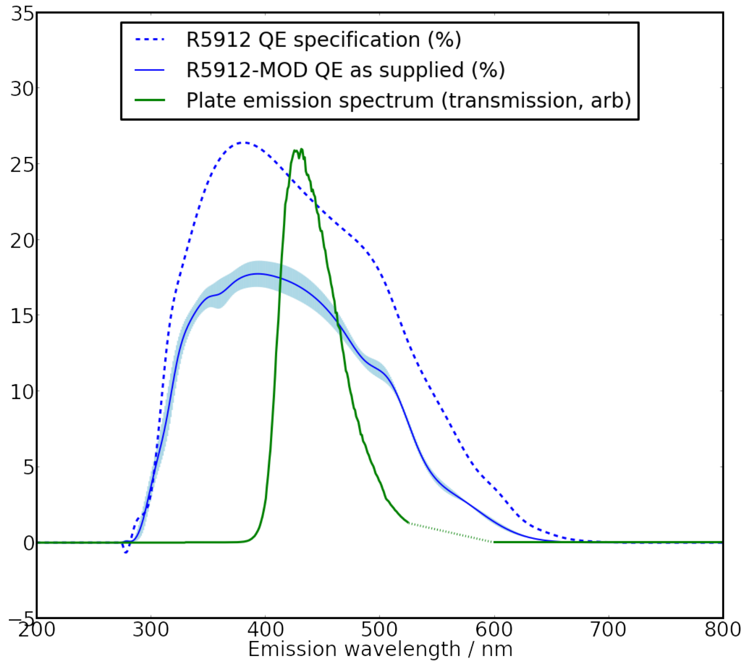

Figure 34: The specification for the non-platinum undercoated PMT from [83]. The blue band shows the mean and standard deviation of the four quantum efficiency curves provided by Hamamatsu for installed MicroBooNE PMTs. Also shown is the measured emission spectra of MicroBooNE wavelength-shifting coatings, discussed in section 5.2.2. [78]

a wavelength dependent quantum efficiency was provided by Hamamatsu for 4 of the 32 installed PMTs. The mean and standard deviation of these curves is shown in figure 34.

The R5912-02mod is a 14-stage PMT. The high gain at room temperature (10^9 at $\sim$1700 V), compensates for known reduced gain at 87 K in the liquid argon. The high gain also has the additional advantage of allowing operation at lower than nominal voltage which reduces heat-loss in the cables and the potential for high voltage breakdown at the feedthroughs.

The PMT base is designed such that the photocathode is grounded and the last dynode in the chain is held at large, positive voltage. Thus the PMT bulb, which is closest to the LArTPC anode plane, is at ground and does not disturb the electric field on the wires. The result is that the high voltage (HV) can be provided and the signal can be extracted from the PMT using a single cable, reducing the cable volume in the vapor region and removing a possible source of out-gassing water impurity.

The flat PC-board base was made of Rogers RO4000-series woven glass-reinforced laminate, which is the same material with the LArTPC cryogenic front end boards. The base is attached $\sim$ 1 cm from the bottom of the PMT and is the closest possible distance of safe approach to the PMT vacuum seal tip. A schematic and photos of the PMT base are provided in reference [70]. The passive components include only metal film resistors and C0G/NP0 capacitors, which have the minimum temperature coefficients, and the performance at cryogenic temperatures were tested. Because the supplied HV and return signal share a single cable, the signal must be split from the HV through an AC-coupling capacitor, as is discussed in section 5.2.5.

All installed PMTs were tested in a PMT test stand, both at room temperature and in liquid nitrogen which is at 77 K. The details are described in reference [70]. In brief, the test stand consisted of a light-tight 346 L, liquid nitrogen filled dewar into which up to four PMTs could be installed. The PMTs were immersed and maintained in the dark environment for up to three days before most measurements of the dark rate and gain were performed. A fiber brought in light from a pulsed blue LED, which was tested for linearity with bias voltage.

Among the important results from cryogenic testing were the following [70]:

- The PMTs could be ramped to voltage quickly in the cold environment, and after 30 minutes, the gains were found to be stable.
- If the room temperature PMTs were immersed in liquid nitrogen, dramatic changes in the gain were observed after initial turn-on. The PMT gain remained high in the first $\sim$5 hours after immersion, and then suddenly dropped by more than a factor of two, afterwards reaching a stable value with a small drift.
- The PMT response showed good linearity up to 100 photoelectrons (PE), which was the maximum attainable by the PMT test stand LED.
- The HV for each PMT was selected to produce a gain of 3×10^7 in liquid nitrogen, and was typically chosen to be $\sim$1300 V.
- The dark current plateaus extended up to 1800 V in liquid nitrogen, and the dark current is higher in liquid nitrogen than at room temperature.
- The PMT performance depended on rate of the pulsed LED.

No PMTs were rejected on the basis of the testing. However, there were three unexpected results to note here.

The first unexpected behavior was that, at room temperature, most of the PMTs showed gains that were 10 to 30% higher than manufacturer's specifications. As expected at cryogenic temperatures, the gain is reduced by $\sim$10% to 50%. To measure the PMT gain, the LED was set to produce one to two PEs. The gain was found from the separation of the single PE peak from the pedestal, where the single PE response is fitted using the procedure described in [84].

Second, it was found that the PMTs are noisier in the cryogenic environment. It would typically be expected that thermal emission is suppressed at cryogenic temperatures and one would expect a lower dark current for PMTs operating in this regime. However, the dark current measured in the liquid nitrogen is higher than at room temperature. Although the cause is unknown, this phenomenon has previously been observed[85]. A proposed explanation is provided in [86].

Third, an LED pulse-rate-dependent gain shift was found during testing, as shown on figure 9 of reference [70]. This behavior is described qualitatively in [87]. With 10 kHz LED pulsing, the gains of cold and dark-adapted PMTs were shown to steadily increase, requiring nearly 24 hours from turn-on to stabilize. The effect was not observable at 10 Hz. This is relevant to MicroBooNE because the cosmic muon rate in the MicroBooNE detector is $\sim$ 5 kHz. Therefore a similar effect is expected in the MicroBooNE detector. Preliminary results from measurements of the PMTs installed in the LAr-filled MicroBooNE cryostat shows the expected effect.

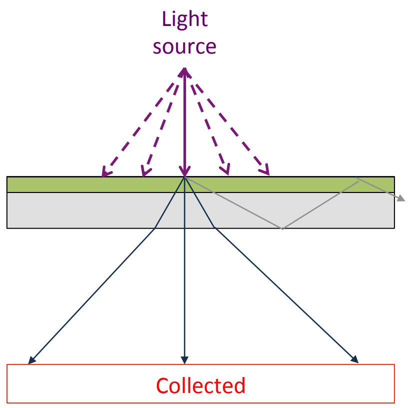

Figure 35: Left : Illustration of transmission mode, used by the optical units. Right: photograph of a coated plate.

5.2.2 Wavelength-Shifting Plates

In order to be sensitive to 128 nm VUV liquid argon scintillation photons, the optical assemblies use a wavelength-shifting coating to convert this VUV light to visible wavelengths that are detectable by photomultiplier tubes. In MicroBooNE, the active ingredient of this coating is TPB, an organic fluor which absorbs efficiently in the vacuum ultraviolet with an emission spectrum peaked around 425 nm [88] as shown in figure 32.

The optical unit PMTs observe light transmitted through TPB-coated, 12-inch diameter acrylic plates (see figure 35). The coating consists of a 1:1 TPB-to-polystyrene ratio, with 1 g of each dissolved in 50 ml of toluene. A small amount of ethyl alcohol is added as a surfactant. The coating is applied to the acrylic plate in three layers by brush-coating. The solution dries in air at room temperature. This leads to a final layer which is oversaturated with TPB, and white crystals form on the surface as the coating dries. The presence of surface crystallization gives the MicroBooNE plates a white, opaque finish. Details of the process are described in reference [89].

The emission spectrum in figure 34 was measured using a Hitachi F-4500 fluorescence spectrophotometer with an incident beam of wavelength 270 nm, selected by a diffraction grating from a xenon lamp. A standard rhodamine dye calibration sample was used to correct for drift in the lamp and spectrometer. The measurement was made in transmission mode, and an artifact peak at a harmonic of the twice incident wavelength was observed between 525 and 600 nm. This region is omitted from the reported spectrum of figure 34.

As shown in figure 34, although the absolute quantum efficiency for the platinum-undercoated cryogenic PMT is lower than the non-cryogenic version, the wavelength dependence is similar, and overlap between the TPB emission spectrum and the sensitive wavelength range of the PMT remains high. Using the measured TPB emission spectrum for plate coatings and the PMT quantum efficiency curve provided, the spectrum-averaged PMT quantum efficiency is $15.3 \pm 0.8\%$ per visible photon incident on the photocathode.

The wavelength-shifting performance of the coating was measured at 128 nm relative to evaporative coatings of the type studied in [90]. Coating efficiencies were measured as a function of wavelength between 128 and 250 nm using a vacuum monochromator at room temperature.

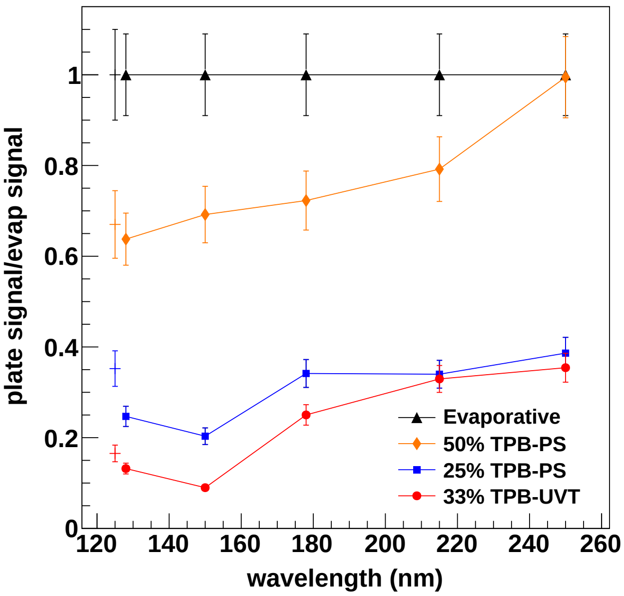

Figure 36: Measured efficiencies of various wavelength-shifting coatings, from [89]. In this plot, 50%TPB-PS is the MicroBooNE plate coating used in the optical units. The 33%TPB-UVT is the light guide coating for the secondary light collection system described below. Connected points were measured in a vacuum monochromator at room temperature, and non-connected points were measured in liquid argon with 128 nm scintillation light. All points are normalized to the performance of an evaporatively coated plate.

They were also measured in liquid argon using 128 nm scintillation light, relative to the same evaporatively coated plate. These data are shown in figure 36, and more information about these measurements can be found in [89].

The absolute efficiency of the MicroBooNE coatings can be obtained by multiplying the relative efficiencies of figure 36 by the measured absolute efficiencies from [90], and accounting for the temperature dependence in the wavelength-shifting efficiency of pure TPB reported in [91]. The expected efficiency of MicroBooNE coatings is found to be 0.98 ± 0.17 emitted visible photons per incident 128 nm photon for the plate coating.

5.2.3 UV Light Protection for the Wavelength-Shifting Plates

TPB coatings have been shown to degrade under exposure to ultraviolet light [68] through a radical mediated photo-oxidation to the UV-blocker and photo-initiator benzophenone [92]. Several measures were taken to ensure that degradation was minimized during the construction of the experiment. The TPB powder and coated elements were stored in the dark at all times, with coated plates and light guides being kept wrapped in foil and stored in a dark container before installation. The detector construction area was covered with a UV blocking plastic [93], and test plates were placed at various positions in the clean tent to check for degradation from stray light. After several weeks of exposure, one test plate with a clear line of sight to the tent entrance demonstrated

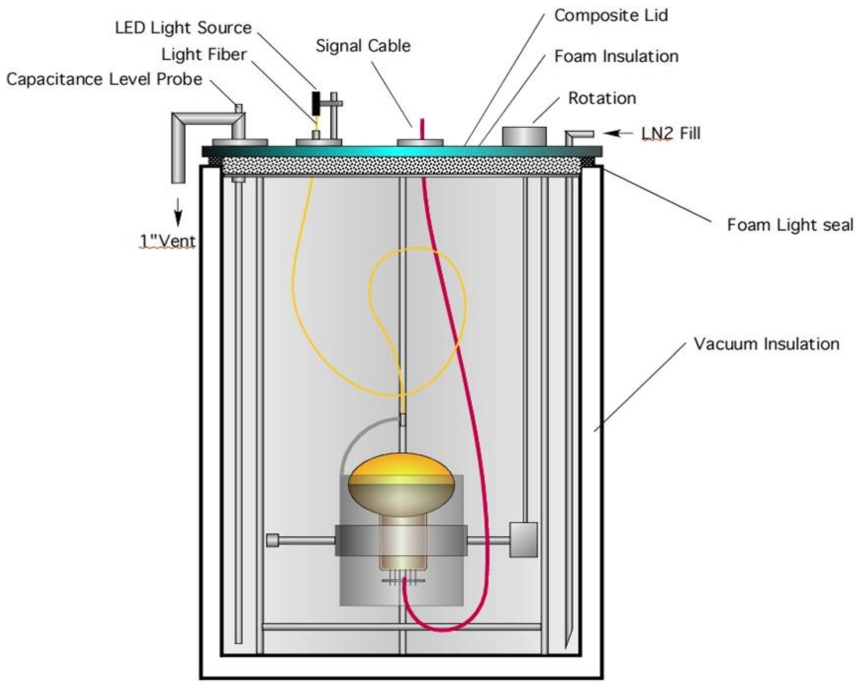

Figure 37: Schematic of the system used to study the mu-metal shields. The design allows rotation along all three axes.

a few percent degradation, and all others showed no observable loss of efficiency. The open end of the MicroBooNE cryostat was shielded from light by a black curtain after installation, and the feedthroughs of the cryostat were blocked when not in use to prevent stray light from entering. The coated plates were the final component of the optical system to be installed into the detector to give the minimum possible light exposure during the detector construction process.

5.2.4 Cryogenic Mu Metal Shields

The trajectories of electrons within the 8" PMT can be deflected by the Earth's magnetic field. This effect can be reduced or removed by surrounding the PMT with mu metal, a metal of low magnetic permeability. Commonly used mu-metal fails to provide shielding at cryogenic temperatures. Two types of cryogenic mu metal,Cryoperm 10 and A4K, both products of Amuneal, were identified that did provide shielding at cryogenic temperature.

The mu metal shields were tested in the apparatus shown in figure 37. The system allowed for the PMT to be positioned at an angle relative to the vertical axis, with the rotator set to 30 positions from 0 to 348°. The set-up was on a dolly that allowed for rotation about the vertical axis. PMT tests were performed in air and in liquid nitrogen. PMTs were dark adapted for 5 hours before testing. A blue LED provided 1 to 2 single PEs of light through an optical fiber. The fiber was fixed to the PMT mount such that the endpoint was stationary with respect to the tube as the system was rotated.

The mean charge from the PMT as a function of angle was recorded. The error was primarily systematic. The $\sim 10^6$ to LED pulses per data point give $< 1\%$ statistical error on the mean.

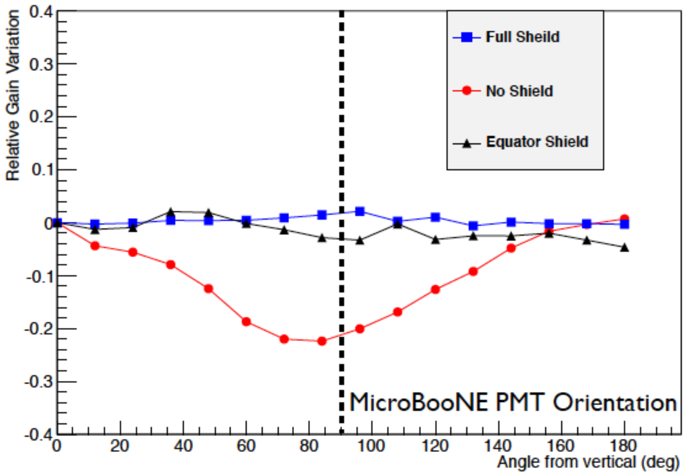

Figure 38: Red: Angular dependence of a PMT response with no shield; Black: for a shield that reaches the tube equator; Blue: for a shield that fully covers the tube to the zenith.

However, 24-hour studies of a single point showed $\sim 5\%$ variations in collected charge due to gain drift. Results showed that A4K and Cryoperm function essentially identically, to within the measurement error, and so MicroBooNE chose A4K, based on significant cost savings. A plot of the relative PMT gain variation versus angle from vertical, figure 38, shows that adding the shield significantly improves PMT performance. This plot shows the effect of the A4K shield with the height aligned with the equator of of the PMT (black) and aligned with the zenith of the bulb (blue), compared to no shield (red) as a function of PMT azimuthal angle. Given the 5% systematic error, the two shield positions are indistinguishable.

As a result of these tests, the A4K shields were designed to extend just past the equator of the PMT. The shield has small holes in the backplate that allows the PMT cables to exit the shield. MicroBooNE is the first LArTPC to use cryogenic mu metal shields in its light collection system.

5.2.5 Implementation of the Primary System

The light collection system is composed of optical units assembled as shown in the left-hand picture of figure 39. The PMT is seated within the mu metal shield on three teflon pads attached to an equatorial support ring. The neck of the tube slides inside a loose wire guide-loop that prevents the PMT from tipping. The PMT is held within this assembly using teflon-encased wires that extend across the bulb and connect to wire hooks attached to the equatorial ring with stainless steel springs. Legs extending from the support at the equator are screwed into a backplate for final mounting. Concern about differences in contraction of the materials led to this design which holds the PMT in place, but with only moderate rigidity. The units were tested to ensure the PMTs would not be displaced during installation and filling. Three posts extend upward from the equatorial ring to hold the plate 3.0 cm above the apex of the bulb. The optical units slide into a cylindrical mu-metal shield, which screws into the equatorial ring. The unit is then mounted on stainless steel back-plates affixed to a support rack, as shown in the right-hand picture of figure 39.

The support rack consists of five stainless steel components, or modules, for ease of installation. Each module has vertical height 1.83 m and horizontal length 2.07 m, resulting in a total

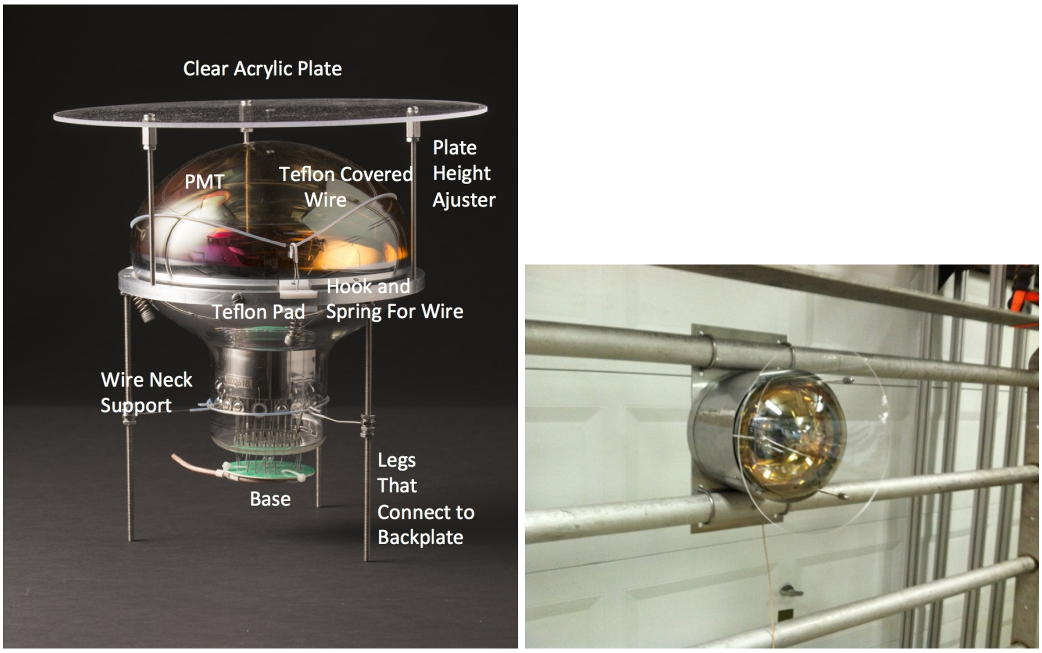

Figure 39: Left: The optical unit mount internal to the shield, with components labeled; Right: Unit mounted on rails. The clear plates were replaced with TPB-coated plates immediately before LArTPC installation, as discussed in the text [70, 72].

horizontal length of 10.36 m. Unlubricated Thomson bearings fitted to the lower edge allow each module to slide into the cryostat on rails mounted in the vessel. The system was designed to allow the light detection system to slide into the vessel after the LArTPC was installed. However, in the end, scheduling permitted installation of the system before the LArTPC installation. This had the advantage of making installation and surveying easier, but the drawback that the system would be exposed to UV light for a long period. Therefore, the units were installed with dummy clear acrylic plates, and the TPB coated plates were installed only just before the LArTPC was moved in and the detector could be easily protected from light. During optical unit installation, each rack module was supported by a temporary mounting rail. The optical units were then mounted in positions chosen to avoid obstruction by the LArTPC cross-bars, as shown in figure 30. As the units were mounted and slid into the cryostat, the cables were loosely tied to the bars of the rack for support and constraint.

The “splitter" circuit, located outside of the cryostat, is shown in figure 40. The splitter separates the HV of the PMT from its output signal which is subsequently split into a high-gain (HG) and a low-gain (LG) channel. The HG and LG channels respectively carry 18% and 1.8% of the output signal. This allows a wide dynamic range for ADC readout of the PMT pulses. The capacitance was chosen to minimize reflections, since the bases are not back-terminated. The HV is supplied to the splitter using BiRa Corporation, Model 4877PS modules.

The PMT cable system delivers HV and returns signals between the external splitter and the optical unit in the cryostat. A single cable runs from an external connector, through the feedthrough filled with Stycast 2850 epoxy [94], into the cryostat and to the PMT base. The RG316/U coaxial

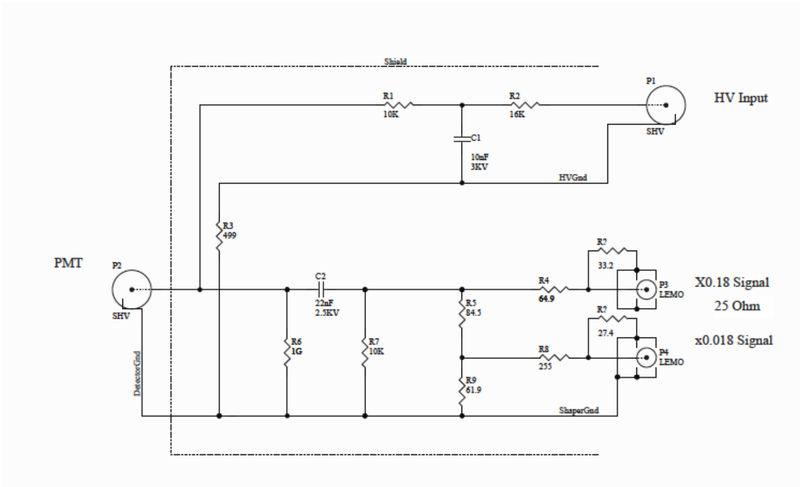

Figure 40: The "splitter" circuit. The circuit connects the HV source to the PMT. It also provides a pathway for signal pulses from the PMT to reach the readout electronics via an AC-coupling capaciter (C2). The signal is split into two copies, one provided with an attenuation factor of 0.18 and another at 0.018. Both signal sources are recorded by the readout electronics in order to provide two dynamic ranges.

cable has 50 Ohm impedance. Cables were terminated with Pasternack PE4498 SHV to accommodate that the cable carries HV to the tube as well as signals from the tube. The cable carries an AC voltage rating of 1100 V; however tests showed the DC rating to be at least three times higher and so suitable for this use. The cables were routed through feedthroughs consisting of a pipe filled with solidified epoxy mounted on a conflat disk. On the warm side of the feedthrough, the cables were terminated at a patch panel with SHV connectors. The SHV connector impedance has a negligible effect on the 20-30 ns PMT signals. SHV cables connect the patch panels to the splitters. The impedance of every channel was tested at the feedthrough patch panel for a stable and correct value for the base resistance, which was 4.04$\pm$0.02 MΩ for the 8-inch PMTs.

5.3 PMT Testing and Quality Assurance

The PMTs were tested and characterized before installation in the detector in the "Bo" cryostat at Fermilab. The Bo cryostat is a 250-liter vacuum-insulated vessel with an inner diameter 22 inches and a depth of 40 inches used for R&D studies, and, relevant to this paper, a vertical slice test of the MicroBooNE optical units. The system is described in detail in reference [78]. The cryostat can be filled with purified LAr with parts per billion level contamination of oxygen and water and parts per million level of nitrogen. The light collection system was tested with light from visible (420 nm) and UV (250 nm) LEDs piped in via fiber, as well as scintillation light from ^{210}Po alpha sources and cosmic rays.

A vertical slice test (VST) of the MicroBooNE optical system was performed in the Bo Cryostat. The slice consisted of two 8 inch PMTs with base electronics, mu-metal shield, TPB plates, cable feed throughs, splitters, the HV power supply and the interlock system. Tests were performed without and with the mu-metal shield. The test made use of the DAQ components described in sec-

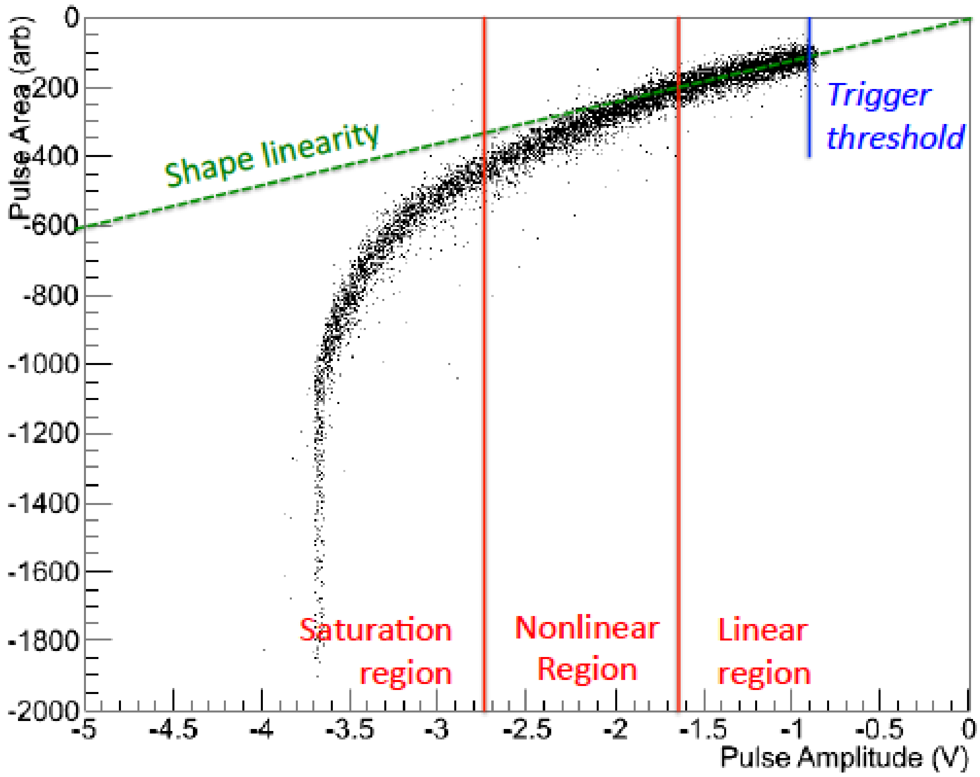

Figure 41: As shown by the VST, linearity of cosmic-ray induced PMT pulses is maintained up to amplitudes of around 1.7 V (300 PE), and amplitude saturation occurs at 3.7 V (670 PE) [78]

tion 6, including the shaper, FEM, trigger card, control card, and server. The MicroBooNE trace impurity monitors were also used.

The VST informed the final design of many components, as well as producing results relevant to understanding the running conditions and performance expectations. For example, during studies of the response of the slice to 128 nm scintillation light from the alpha source, valuable information was gathered on the single photo-electron dark rate and cosmic ray rate that could be scaled to the MicroBooNE detector expectations. As a second example, these runs allowed characterization of the pulse shape nonlinearities of the optical units, as seen in figure 41. These were shown to be significant at $\sim$300 photo-electron in pulse amplitude. Full amplitude saturation occurred at $\sim$670 PE. Thus, it is concluded that for pulses of more than 300 PE, pulse shape cannot be described by linear superposition of single photoelectron pulses.

5.4 Secondary System: Acrylic Light Guides for R&D

A secondary light collection system consisting of four lightguide paddles was also installed. This concept has several advantages for future large detectors such as DUNE. First, the collection area per channel is larger than the optical units, providing more coverage for the same number of electronics channels, cables, and feedthroughs. Second, the detectors have a flat profile so they can be slid between chambers in a multi-LArTPC detector, minimizing space requirements of the light

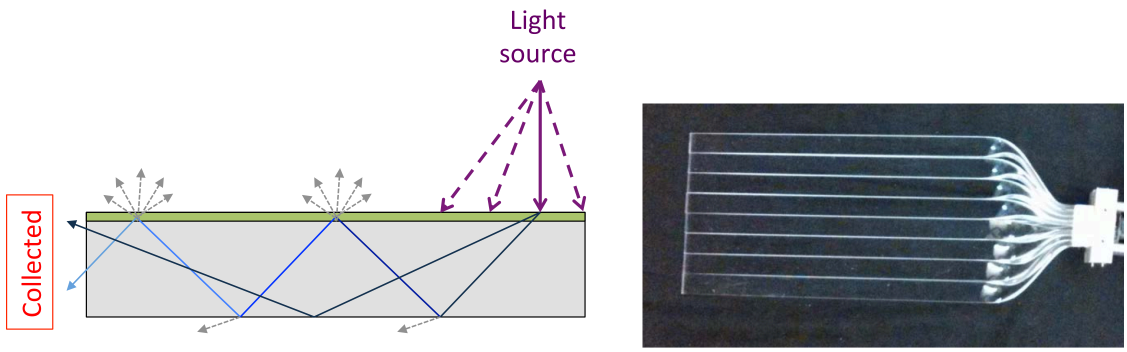

Figure 42: Left : Illustration of guiding mode, used by the paddles. Right: photograph of a coated paddle.

collection system. In the case of MicroBooNE, the design gradually guides light in bent acrylic bars to a PMT. This design was an early alternative to a perfectly flat design that guides the lights to SiPMs. Running this system will provide long-term information on performance of lightguide based systems. It also enhances the MicroBooNE dynamic range, since the lightguide detectors saturate at a much higher light level than the optical units.

In the case of the lightguides, the 128 nm light is absorbed and shifted by a clear wavelength-shifting coating, and the re-emitted light is guided to a 2-inch Hamamatsu R7725-MOD PMT, as illustrated in figure 42, left. The installed paddles consist of six bars. A photograph of one coated paddle with eight bars is shown in figure 42, right. The active length of each bar is 20 inches. This system was added for R&D purposes and made use of 8 spare channels available of HV, cables, feedthroughs, and electronics. The impedance of the 2 inch PMTs, tested at the feedthrough, was 4.89 ± 0.01 MΩ. As shown in figure 30, each paddle is installed next to an optical unit for direct comparison of performance.

The coating requirements for plate assemblies and light guides are different, and so the composition and coating methods for each were separately optimized. In the case of the light guide coatings, the figure of merit is the light emitted in guided mode. Guided mode light is the light that is detected at one of the ends of a test sample, which is orthogonal to the illuminated face of the sample. In addition to the wavelength-shifting efficiency of the active layer, the detected light yield is affected by the reabsorpative and scattering losses in the coating as visible light propagates along the bar. The light guide assemblies have a TPB coating of 33% TPB to 67% UVT acrylic by mass, also with ethanol surfactant. The coating is applied as a single layer and the TPB remains suspended in the acrylic matrix as the coating dries, leading to a smooth, visibly transparent surface. The performance and attenuation behavior of similar light guides to those installed in MicroBooNE were studied experimentally in [69]. The reported non-exponential attenuation suggests that surface losses dominate over bulk losses as the attenuation mechanism, and that the fractional loss per reflection within the light guide is of order 2-3% [92].

In the light guide coatings, the TPB is suspended in an acrylic matrix which leads to a slight

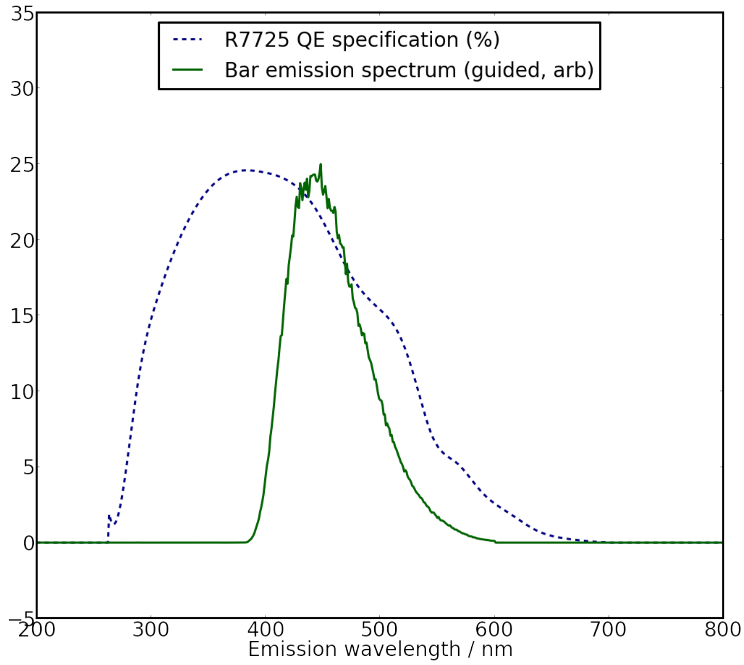

Figure 43: Measured emission spectra of the light guide coating in guided mode, and the R7725 quantum efficiency. Only the quantum efficiency of the non-undercoated PMT model is shown, from [99].

broadening of the emission spectrum compared to the spectrum from the plates. This is an expected effect–TPB fluorescence has been shown to have dependence upon its microenvironment [95, 96, 91, 97, 98], and reference [91] demonstrated spectral broadening in the presence of a polystyrene substrate. Using the monochromater described for the plate spectrum studies, the light guide coating spectrum was measured in guided mode. A 10 cm section of light guide, with the incident beam perpendicular to the TPB coated surface, was used. Based on reference [91] it is expected that the emission spectrum for the light guide coating, with TPB embedded in the substrate, will not change significantly as it cools to 87 K. The expected efficiency for the light guide coating is found to be 0.25 ± 0.05 emitted visible photons per incident 128 nm photon.

5.5 Calibration

The flasher system for the optical units and the light guides is described in reference [75]. This system was developed to check the timing of the installed optical units, exercise the optical units during construction and commissioning, and to calibrate them once the detector is operational. The reference provides engineering drawings and details. The system is briefly summarized here.

A control board pulses an array of 400 nm LEDs, each of which is coupled through an optical feedthrough to 10 m optical fibers within the cryostat. The custom feedthrough/patch panel design encases the fibers in Arathane CW 5620 blue with HY 5610 hardener. The internal fibers are Molex FVP polymide fibers with diameter of 600 mm, cladding of 30 μm, and an additional buffer layer of 25 μm. Each PMT has an individual calibration fiber. Each fiber is routed along the rack and

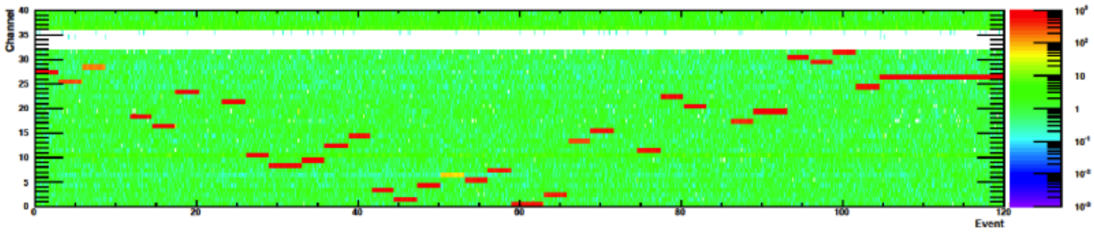

Figure 44: Charge detected in each PMT due to flasher tests, shown as a function of time. Each PMT is flashed for a short period. The white band indicates unused channels.

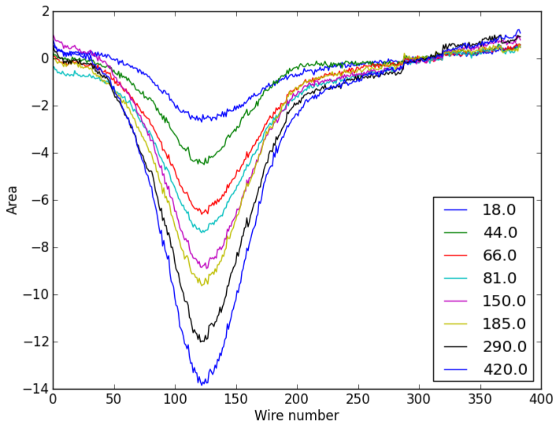

Figure 45: Area of signal pulses recorded on collection plane (in arb. units) as a function of wire number (arb. offset). The legend indicates the calibrated photo-electron count. The signal pulses are averaged over 50,000 repetitions. The plots are pinned together at wire 300, as the distribution baseline fluctuated over the course of the experiment due to intermittent noise.

attached to the PMTs by a fiber holder constructed of an aluminum standoff with a nylon-tipped set screw at a distance of about 2 inches from the PMT glass.

Figure 44 shows the results of flasher tests on all 32 optical units and four PMTs on the paddles. Time is along the x axis and PMT channel number is along the y axis. The white region separating the optical unit PMTs from the paddle PMTs represents unused channels. The colored bars indicate charge detected in the PMTs during flashing. One can see that all tubes respond properly.

5.6 Coupling of PMT Signals to the Anode Wires

The ICARUS detector has observed an unexpected cross-talk between their PMTs and collection wire plane [100]. The Argontube test stand at the University of Bern also observed this effect [101]. Therefore, while the LArTPC was under final testing, before being rolled into the cryostat, an experiment was devised in order to determine the implication of this cross-talk for MicroBooNE. One of the production 8″ Hamamatsu R5912-02mod PMTs was placed 5″ from the LArTPC collection wire plane. This PMT was encased in a dark box with an optical fiber delivering light from a LED flasher. The collection wire plane was read out using a DAQ test-stand that reflects the final DAQ design.

A clear signal was observed on the collection plane when the LED fired. The magnitude of the signal was characterized as a function of photo-electron count (figure 45) and separation between the PMT and wire-plane. The signal induced on the collection plane was estimated to be no more than ~ 10 ADC counts for a cosmic ray under normal operating conditions. This was reduced to ~ 2 ADC counts when the PMT was encased in the μ-metal shields. This was deemed an acceptably small amount that further shielding was not required.

The effect appears to saturate with photo-electron count, and is reduced when shorting the resistors between the anode and last dynode. A later test with Argontube showed that the signal was drastically amplified when using capacitors not able to withstand cryogenic temperatures in the PMT base [101]. This suggests that the effect is electrostatic in nature, and probably due to capacitive coupling between the PMT and wire-plane. This is also suggested by the similarity between the signals observed and those produced by anode-coupled readout of a light collection system [77].

5.7 Initial Performance of the MicroBooNE Light Collection System

The system was first powered on after the cryostat had been filled with liquid argon. All the PMTs in both the primary and secondary system were found to be operational. Figure 46 shows the waveforms for all the PMT channels around the time that a large pulse, potentially from a cosmic ray muon, is observed. After initial checks of the system's health, the single photoelectron response of each PMT was set such that a one photo-electron pulse has an amplitude of 20 ADC counts as seen by the PMT readout system. The flasher LED system, described previously, is used to set this response. Figure 47 shows a candidate single photoelectron pulse following arrival of a TTL logic pulse driving the LED flasher system. The LED light level is set so that the majority (about 80%) of waveforms see no response in the region where pulses from the LED are expected to occur. This ensures that for windows with pulses, the pulses are of single photoelectrons. Figure 48 shows an example of the area vs. maximum amplitude of such pulses seen by a PMT during the flasher runs.

6. Electronics and Readout Systems

The analog signals that develop on a LArTPC during its operation must be amplified, digitized, and written to disk for use in analysis. Custom low-noise electronics that are capable of operating in the liquid argon environment have been developed for this purpose in MicroBooNE. The data from these LArTPC electronic channels, as well as from the PMTs, is sent to a readout system that digitizes and organizes the information before passing it along to a Data Acquisition (DAQ) system that stores it on disk. The stages of signal processing are illustrated in figure 49. The following subsections describe the LArTPC cold electronics, the LArTPC and PMT readout electronics systems, and the DAQ system in more detail. Details of triggering capabilities available in MicroBooNE are also provided in this section.

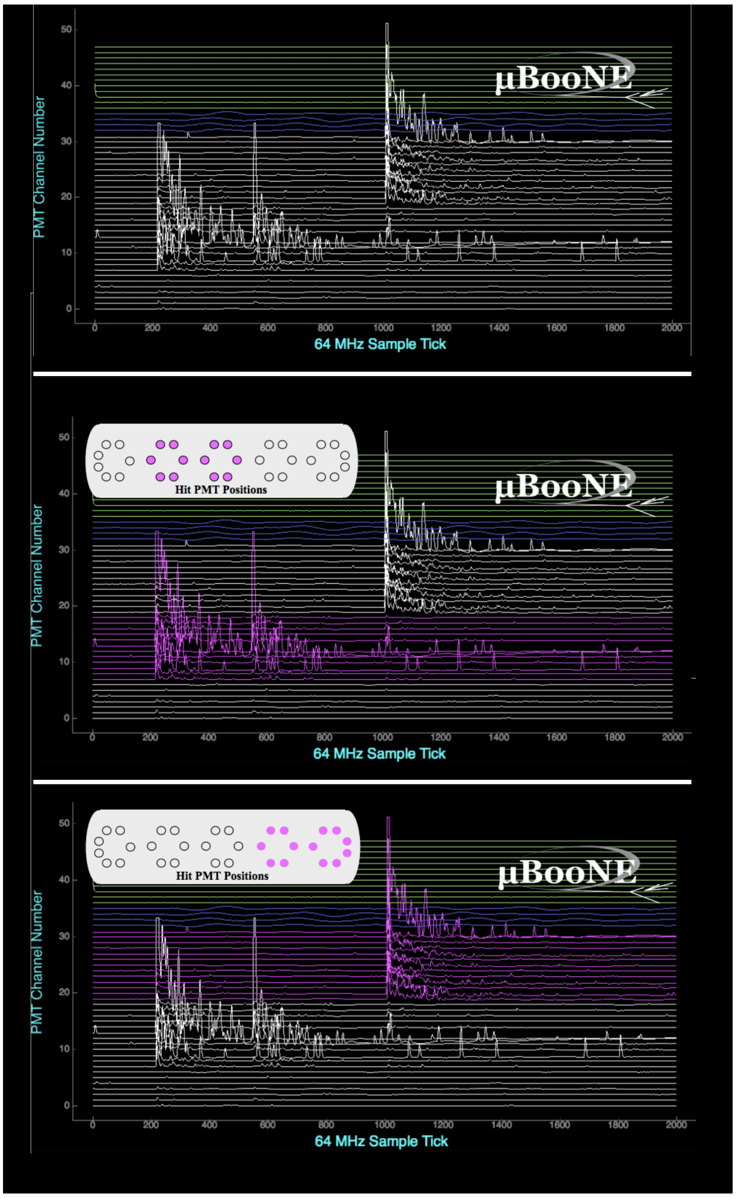

Figure 46: Top: Example waveforms from all 32 PMTs of the primary light collection system over a 31.25 microsecond readout window. The waveforms from the PMTs are in white. The blue waveforms are from the secondary lightguide PMTs, which are off in this picture. Waveforms from channels reserved for logic inputs are shown in green. In this image, the PMTs see two successive flashes of light at different parts of the detector. Middle and Bottom: Magenta highlights the early and late pulse, with the insets showing the PMTs which fired. Each pulse is likely from two cosmic ray muons traveling through the detector.

6.1 Cryogenic Low-Noise Electronics

To obtain optimum detector performance, MicroBooNE uses cryogenic low-noise front-end electronics for readout of the LArTPC. To reduce electronic noise, the interconnection length between

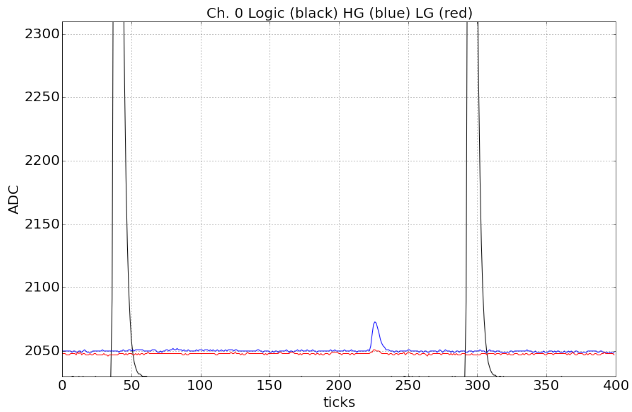

Figure 47: Example waveform captured by the PMT readout electronics during single photoelectron calibrations. The black waveform is of logic pulses that mark time at which an LED in the flasher system is driven. After some delay coming from PMT cable lengths and the flasher system, a candidate single photoelectron pulses is seen.

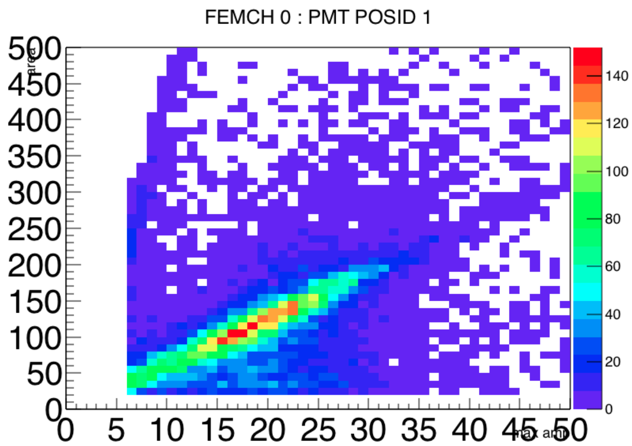

Figure 48: Distribution of the maximum amplitude and charge of pulses collected during an LED flasher calibration run. The central distribution of events is due to single photoelectron pulses.

the LArTPC wires and preamplifier should be as short as possible thus minimizing the total capacitance seen at the preamplifier input. To accomplish this, the analog front-end ASICs, which include a preamplifier, shaper, and signal driver are located inside the cryostat in addition to the wire bias voltage distribution system, decoupling capacitors, and calibration networks. The front-end ASIC and associated circuits are implemented on a cold mother board which is directly attached to wire carrier boards on the LArTPC itself. Cold cables are used to transmit output signals from cold motherboards to warm interface electronics installed on the top of signal feed-through flanges.

6.1.1 CMOS ASIC

The analog front end ASIC is designed in 180 nm CMOS technology, which integrates both the preamplifier and shaper on a single chip. Each chip has 16 channels to read out signals from 16 wires. Each channel also has a charge injection capacitor for precision calibration. In MicroBooNE,

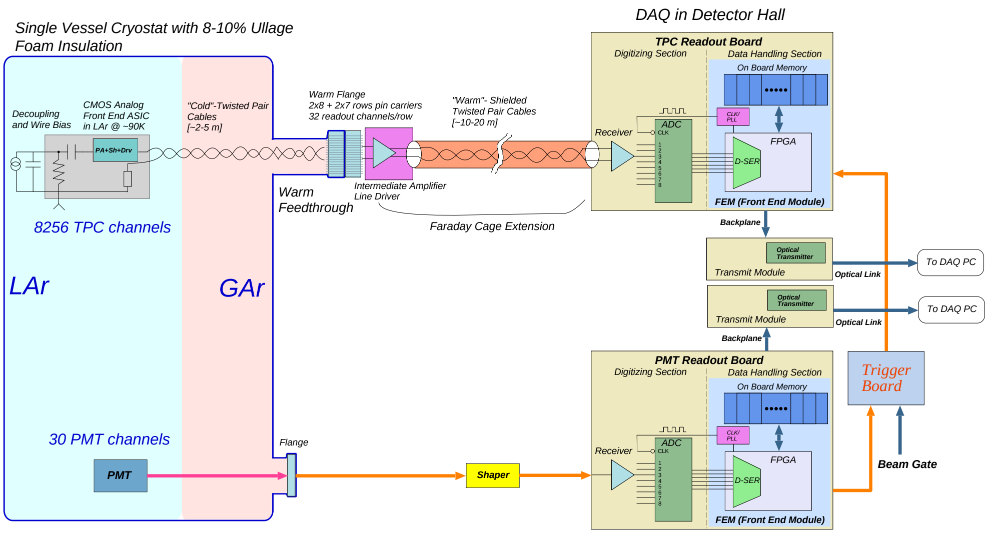

Figure 49: MicroBooNE LArTPC and PMT signal processing and readout stages.

the shaper has 4 programmable gain settings (4.7, 7.8, 14 and 25 mV/fC) and 4 programmable peaking time settings (0.5, 1.0, 2.0 and 3.0 μs) that provide increased flexibility to the readout system. The ASIC also has programmable baseline settings (200 or 900 mV) to accommodate different detection wire configurations: either collection or induction plane. It has a selectable AC/DC coupling mode with a 100 μs time constant for the AC coupling mode which can be used to reduce low frequency noise. The ASIC also has built-in band-gap reference and temperature sensors to facilitate biasing and monitoring.

The CMOS ASICs consume only $\sim$6mW/channel in its default configuration. The front end ASICs of the entire detector generate $\sim$50 W of heat load that is easily handled by the cryogenics system. Design guidelines that constrain the electric field and the current density to address the lifetime of CMOS devices operated at cryogenic temperatures have been applied to every single transistor (total $\sim$15,000 transistors) in the ASIC design. A picture of the layout of the CMOS ASIC is shown in figure 50. Test results agree well with simulations and indicate that the analog and the digital circuits (including the digital interface) operate as expected in the cryogenic environment.

The MicroBooNE LArTPC has 8,256 readout channels and a total of 516 CMOS ASICs are required to fully instrument the detector. The production testing of the CMOS ASICs required two steps: both a warm and cold test. The warm test was performed with a dedicated test board housed in a Faraday box containing a socket to house the ASIC for ease in chip exchange. All programmable parameters (gain, peaking time, baseline, AC/DC coupling etc.) were exercised with the warm test setup for careful screening at room temperature. The yield of the warm testing of the ASICs was $\sim$89%. ASICs must have passed the warm test before going through cold testing. The cold test was performed with a dedicated test board containing 6 sockets to facilitate testing of multiple chips in liquid nitrogen at the same time. A total of 201 ASICs went through cold testing with a yield of $\sim$97%. Based on this high yield, it was decided not to continue the cold

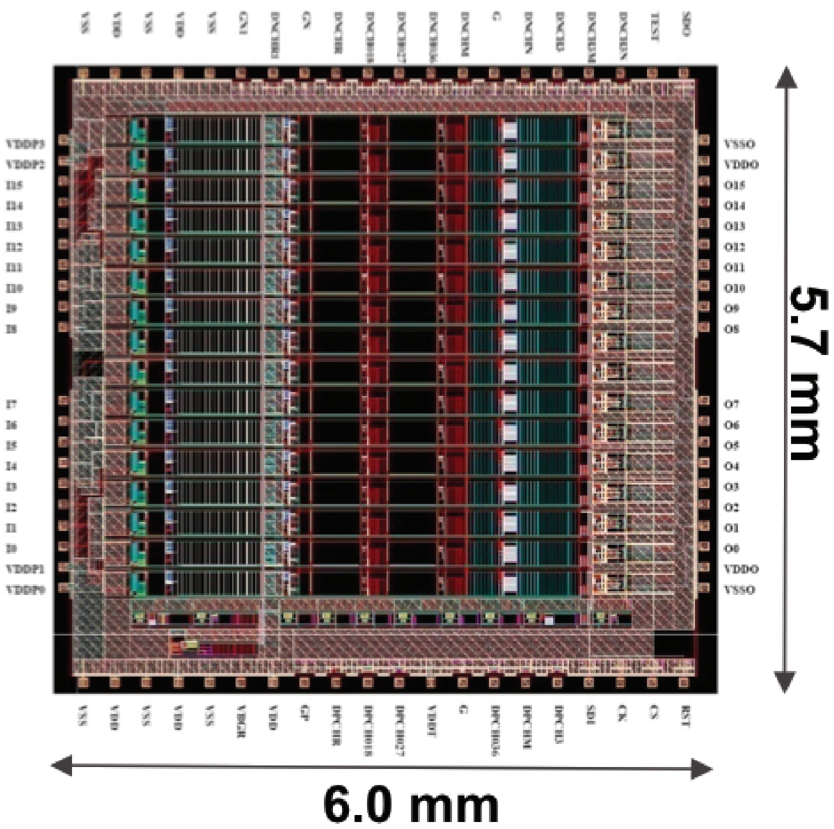

Figure 50: Layout of the CMOS analog front end ASIC

screening test on the rest of the production chips, as they were tested cold after being installed on the motherboard. After enough (∼600) ASICs passed the production screening test, they were sent to an assembly house to equip the cold motherboard.

6.1.2 Cold Motherboards

A cold motherboard was designed to house the MicroBooNE CMOS ASICs. In this capacity, the motherboard provides signal interconnections both between the detector wires and preamplifier inputs as well as between the driver outputs and cold cables to the signal feed-through. The cold motherboard design provides sufficient protection of the ASICs against electrostatic discharge during installation. It also provides a calibration network and bias voltage distribution for the wire planes. Specifically, a calibration signal enters the cryostat via a feed-through and reaches the preamplifiers through the motherboard. Each preamplifier channel in the ASIC has a built-in switch to individually cycle the calibration injection. The bias voltage reaches the LArTPC wires via a two-fold redundant path on the motherboard that allows the detector to operate normally even if one bias voltage channel fails. Use of Rogers 4000 series as the base material of the cold motherboard avoids the potential risk of contamination of the liquid argon. The Rogers material has a similar temperature expansion coefficient as the surface mounted components which enhances the reliability of the electronics assembly when operated at cryogenic temperatures. The different positions of the wire attachments along the top and sides of the LArTPC requires 2 types of cold motherboard. The top version of the motherboard has 192 readout channels that includes 96 Y channels, 48 U channels, and 48 V channels. The side version of the motherboard has 96 readout channels that are either U or V channels. A picture of the top version of a cold motherboard with 12 mounted ASIC chips is shown in figure 51.

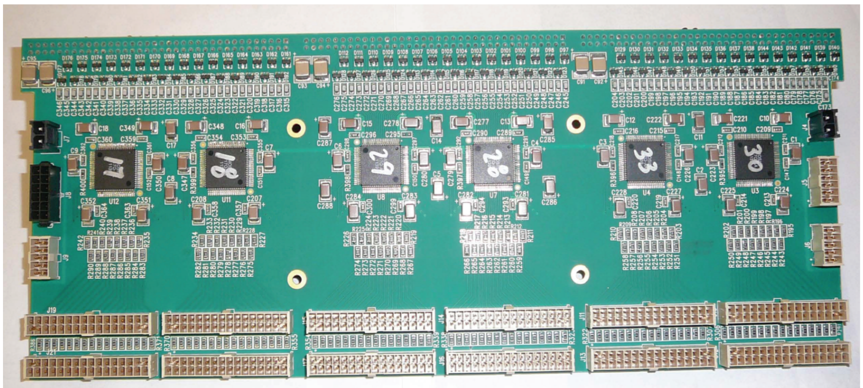

Figure 51: Top version of cold motherboard with 12 ASIC chips including 6 chips are mounted on top layer and 6 chips on bottom layer

The MicroBooNE LArTPC required a total of 36 top version motherboards and 14 side version motherboards to instrument the full detector. A test stand was built for testing of the front end electronics. This test stand included a full readout chain from the cold motherboard, cold cable, signal feed-through, warm interface electronics, warm cable and Receiver ADC board to a DAQ board based on a Xilinx ML605 FPGA evaluation board which sends acquired data to a PC over a Gigabit Ethernet. The production test of each motherboard also involved both a warm and cold test. Both tests used the same test stand, except the motherboard was placed in a Faraday box for the warm test and submerged in a liquid nitrogen dewar for the cold test. Noise, gain, peaking time, and linearity parameters were measured in both warm and cold to screen the motherboard. Motherboards had to pass both tests before being installed on the detector.

6.1.3 Cold Cables

Cold cables transmit the detector signals from the cold motherboard to an intermediate amplifier on top of the signal feed-through and distribute power to the CMOS ASICs. The cold cable is a custom-built 32-pair twisted pair flat ribbon cable with Teflon FEP insulation and 100Ω $(\pm 10\%)$ impedance, using AWG 26 stranded wire with silver-plated copper. Custom designed shells with jack screws used in the cable assembly ensured proper alignment of the insertion on the signal feed-through pin carriers. The twisted pair cable was ordered from the manufacturer and sent to a company to be woven into flat ribbon cables. Cold cables of two different formats were assembled by an assembly house: signal cables and service cables. Signal cables are used to transmit amplified detector signals while the service cable is used to transmit calibration pulses and slow control/monitoring signals. Signal cables were produced in three different lengths: 80 inch, 100 inch and 180 inch to accommodate the different lengths between the cold motherboards and the signal feedthroughs, while the service cables were produced in two different lengths: 100 inch and 180 inch. All of the cold cable assemblies were tested with a cable tester in the assembly house before they were shipped out. In addition, $\sim$10% of the cold cables were tested in the test stand at BNL to confirm the quality of the cable assembly.

6.1.4 Electronic Calibration

The MicroBooNE cold electronics include a precision charge calibration system. Through the cold cable and calibration network on the motherboard, a calibration signal enters the cryostat via a feed-through and reaches the preamplifiers. A built-in switch in the ASIC makes it possible to power cycle the calibration injection for every channel individually. The electronics calibration is based on charge injection through known capacitances (180 fF) in the ASIC. This system enables gain (charge sensitivity) calibration, verification of sense wire integrity and noise measurements. The built-in electronics calibration capability is an important tool in testing and characterizing the overall performance of the detector readout system. It was extensively used in the cold electronics production testing and the electronics checkout during installation, commissioning, and data taking.

6.1.5 Performance Tests

The development of the analog front end ASICs was initiated using 180 nm CMOS technology and 300 K models, though the performance parameters are extracted at 77 K. CMOS was found to function at cryogenic temperatures with increased gain and lower noise. The noise, gain, and pulse shaping were found to be as expected in evaluation tests of the ASICs. Extensive testing of the ASICs mounted on the motherboards was performed; these tests were done in liquid nitrogen rather than at room temperature, since noise levels and characteristics of the ASIC performance in liquid nitrogen are similar to the performance in liquid argon. Thus, cold tests were performed on all production cold motherboards fully populated with 12 chips. A total of $\sim$2,200 chip-immersions were accumulated in liquid nitrogen without any failures due to thermal contraction or expansion.

The test results show the noise of the front end readout electronics system decreasing uniformly for all 768 channels from $\sim$1,200e^- at 293 K to less than 600e^- at 77 K with 150 pF detector (sense wire) capacitance. A plot of noise versus temperature of 12 ASICs for a total of 192 channels is shown in figure 52. The response of the front end electronics exhibits excellent uniformity at cryogenic temperatures. As shown in figure 53, the gain variation of a cold motherboard with 12 ASICs is only $\sim$7% peak-to-peak across 192 channels. The spread of the gain variation is only $\sim$1% of the gain setting.

6.2 Warm Electronic Amplification

Signals from the cold electronics are carried over the cold cables to dedicated feedthroughs mounted on the cryostat. The cold cables are connected to pin-carriers located on 14-inch CF signal feedthrough flanges that are mounted on nozzles N1A-N1K of the cryostat (see figure 5). The signal feedthrough design must accommodate 100% hermeticity and high signal density. A design based on the ATLAS pin carrier style was developed for this purpose. Two 8-row pin carriers and two 7-row pin carriers are welded onto the 14-inch CF flange, as shown in figure 54, and create a vacuum-tight seal. Nine of the 11 signal feedthroughs receive signals from the three LArTPC anode planes (384 Y-plane, 192 U-plane, 192 V-plane), while the remaining two on the extreme ends of the cryostat only receive signals from one of the angled induction planes (672 U-plane on one feedthrough, 672 V-plane on the other).

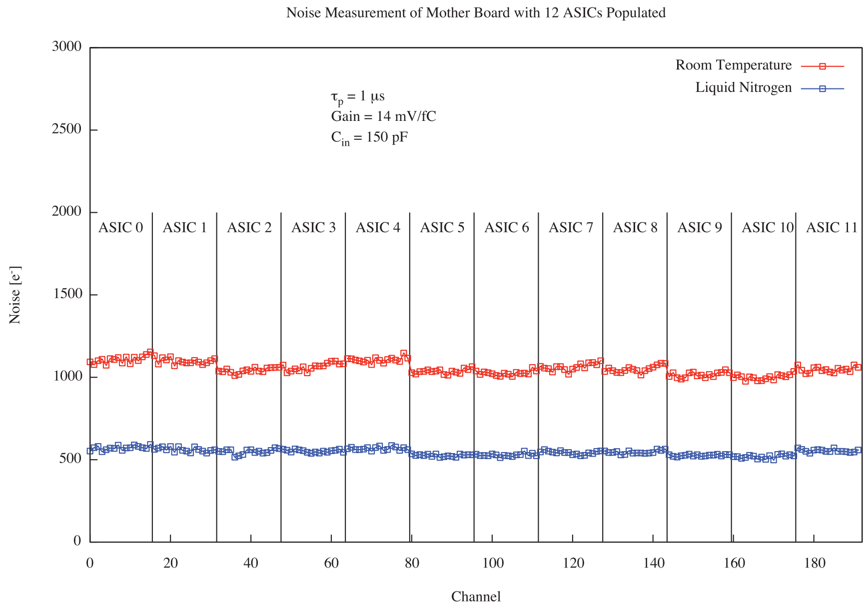

Figure 52: Plot of noise vs. temperature of 12 ASICs, total 192 channels. Noise is ∼1,200e^- at 293K, and ∼550e^- at 77 K with 150 pF C_d

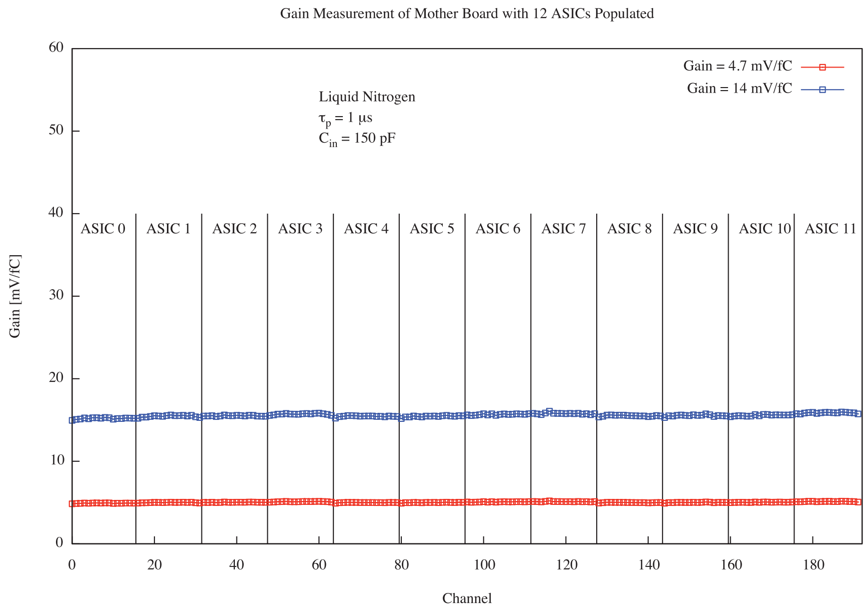

Figure 53: Plot of gain uniformity of 12 ASICs, total 192 channels, at 77 K with two different gain settings

A Faraday cage is mounted on the external, warm, side of the signal feedthroughs to provide shielding for the intermediate amplifiers located inside. The bias voltage feedthrough, which sup-

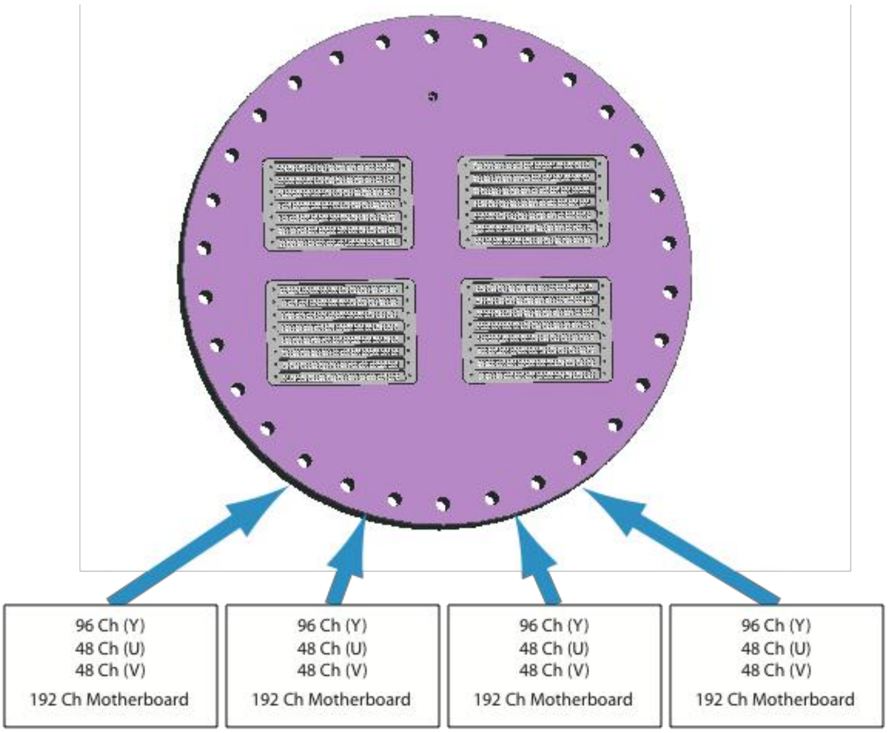

Figure 54: Signal feedthrough flange consisting of a 14-inch CF flange with two 8-row and two 7-row pin carriers welded in place.

plies anode plane bias voltages into the cryostat, is built onto a small 2.75-inch CF flange welded onto the signal feedthrough flange. A filter board mounted on the bias voltage flange filters noise and ensures a good ground connection. Figure 55 shows details of the signal feedthrough assembly with electronics boards, bias voltage feedthrough, and Faraday cage.

The intermediate amplifiers provide $\sim$12 dB gain to the LArTPC signals to make them suitable for transmission over a 20 m long cable to the readout electronics (see section 6.3). Each intermediate amplifier has 32 channels installed on the signal feedthrough flange and housed inside the Faraday cage to provide noise isolation. Figure 56 shows a picture of a prototype intermediate amplifier plugged on the signal feedthrough pin carrier. The intermediate amplifier uses a 68-pin SCSI-3 connector to drive the 32 channels of signal differentially for better noise immunity. The layout and connector position have been carefully designed to ensure the card can be plugged on the pin carrier in either direction. This efficiently utilizes the limited available space on the top of the feedthrough, which also makes the design of the Faraday cage easier.

In addition to the intermediate amplifiers, there are two service boards mounted on the top of each signal feedthrough. The service board provides regulated low voltage, control and monitoring signals to the analog front end ASICs. It also provides pulse injection to the preamplifiers for precision calibration. The control, monitoring, and calibration signals are provided to the front end electronics with two-fold redundancy. Should one set of signals become defective the detector can still operate normally with the redundant set. Each service board plugs onto a 64-pin carrier row.

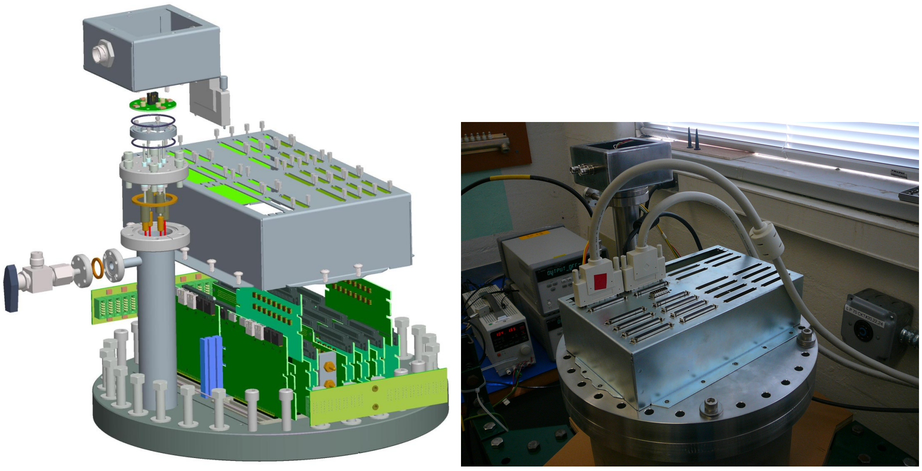

Figure 55: Left: Diagram of the signal feedthrough assembly, which includes intermediate amplifiers, Faraday cage, bias-voltage feedthrough and filtering circuit. Right: Photograph of one of the feedthrough assembly, partially constructed and being tested.

Figure 56 shows a picture of a prototype service board.

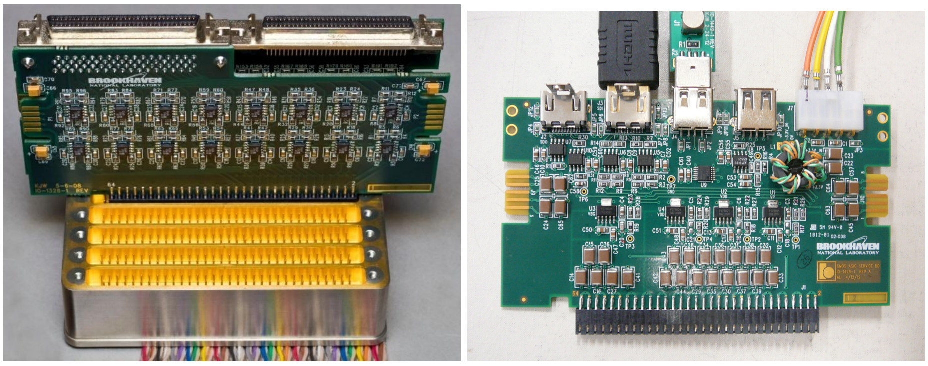

Figure 56: Left: Photograph of one of the intermediate amplifier boards plugged into a pin carrier during testing. Right: Photograph of a prototype service board.

6.3 Readout Electronics

The MicroBooNE readout electronics system consists of two subsystems: the LArTPC and PMT readout electronics. The LArTPC readout electronics are responsible for the readout, digitization, and processing of the induction and collection wire signals after amplification. The PMT readout electronics are responsible for the amplification, shaping, digitization, and handling of PMT signals, as can be used to provide a trigger signal for the readout and data acquisition systems. While the LArTPC and PMT readout systems share the same back-end design that organizes and packages the data for delivery to the DAQ system, they employ different analog front-end and digitization designs, which are described in this and the following subsection.

The LArTPC readout electronics are responsible for processing the signals from the 8,256 wires in MicroBooNE after pre-amplification and shaping in the cold electronics (section 6.1). The pre-amplified and shaped analog signals from the cold electronics are transmitted to the warm electronics outside the cryostat, as described in section 6.2, and then passed to custom-designed LArTPC readout modules distributed evenly over nine readout crates. The readout modules digitize the analog signals and then process and prepare them for shipping to designated DAQ machines (one per readout crate) (section 6.6).

The LArTPC readout crates communicate with the DAQ machines via three duplex 3.125 Gbits/sec optical links that connect to a crate controller module and data transmitter (XMIT) module on the crate end, and to three PCI Express boards on the DAQ machine end. The controller is responsible for configuration, trigger and run control command distribution as well as the slow monitoring of each readout crate. The controller occupies one of the optical links while the XMIT is responsible for sending two separate streams of readout data to the DAQ machines via the two other optical links. The first XMIT stream contains losslessly compressed LArTPC data associated with event triggers received by the LArTPC readout crates, such as the BNB trigger, and is referred to as the "NU" data stream. The second stream is a continuous LArTPC data stream which is compressed with some data loss. The continuous data stream is used for beam-unrelated physics analyses, such as the study of potential supernova neutrino events, and is referred to as the "SN" data stream. The compression schemes used in the NU and SN streams are described in section 6.3.3.

All readout crates are synchronized to a common 16 MHz clock. The clock sync is provided by a clock fanout board which shares the same ground as all readout crates, and is sent via coaxial cable to a distribution board which is mounted on each crate backplane. The readout frame size is set to 1.6 ms, which is equivalent to the time it takes for charge produced on the far end of the LArTPC to drift to the wire planes at the design cathode voltage of -128 kV.

6.3.1 Data Digitization

The amplified and shaped analog LArTPC signals are differentially received and digitized in the first section of the readout modules. Each ADC module holds 8 AD9222 octal-channel 12-bit ADCs. Each ADC module handles signals from 64 wires. The wire signals are grouped in two sets of 32 consecutive wire channels: either 32 induction wires plus 32 collection wires or two sets of 32 induction wires. The induction channel sequence alternates wires between the two induction planes. The ADC module digitizes the signals continuously at 16MHz. Each channel has a configurable baseline, which is either set low (450 ADC counts) for collection channels or at the middle of the dynamic range (2055 ADC counts) for induction channels, thus ensuring that both the collection plane unipolar differential signals and the induction plane bipolar differential signals can make use of the full ADC analog input range. The requirement to observe a MIP produced at the far end of the LArTPC in the induction plane determines the lower end of the dynamic range, while the requirement to observe a highly-ionizing stopping proton at the close end of the LArTPC without saturation sets the upper end. The digitized outputs from the ADC board are passed directly to a Front End Module (FEM) in the second section of the LArTPC readout module. The FEM houses an FPGA for data processing, data reduction, and preparation for readout by the DAQ system as described in the following section.

6.3.2 Data Handling

The FEM board consists of a 14-layer printed circuit board which is mechanically integrated with the ADC board as illustrated in figure 57. The choice of a smaller board allows for short trace lengths which is beneficial for high speed signals. The full assembly comes together as a standard VME 9U card in height, with a 280 mm depth. Differential outputs from the ADCs connect to the FPGA through HM-Zd connectors that have individual ground shielding on each differential pair.

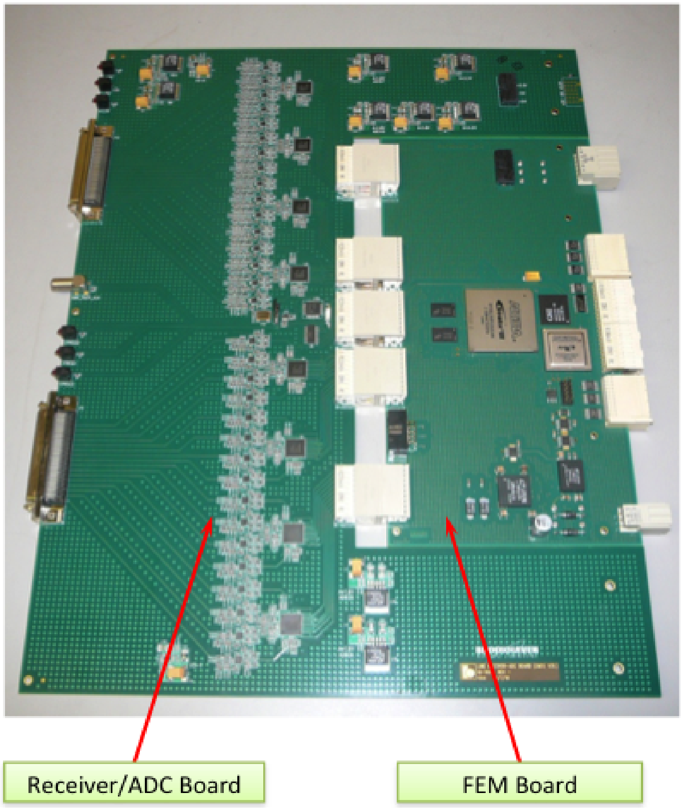

Figure 57: LArTPC ADC+FEM board.

The digitized data stream moves from the ADCs to a Stratix III Altera FPGA, which reduces the sampling rate of the ADC from 16 MHz to 2 MHz. The 2 MHz sampling rate is optimized by taking into consideration the expected pulse shape provided by the convolution of the cold electronics, the expected LArTPC field responses, and the O(1μs) diffusion effects which govern charge drift within the liquid argon. The FPGA stores the data from all 64 wires per board sequentially in time in a 1M $\times$ 36 bit 128 MHz SRAM, grouping two ADC words together in each 36 bit memory word. This requires a data storage rate of (64/2) $\times$ 2 MHz $=$ 64 MHz. The SRAM chip size and memory access speed allow for continuous readout of the LArTPC data. Since data reduction and compaction algorithms rely on the sequential time information of a given wire, the data readout out from this SRAM takes place in wire order in alternate clock cycles, again at the rate of 64 MHz. This read in/out sequence is illustrated in figure 58.

Separate DRAM multi-event buffers on the FEM store the NU and SN data streams. The data divert into the NU readout stream when a trigger is issued and received (as shown in figure 59)

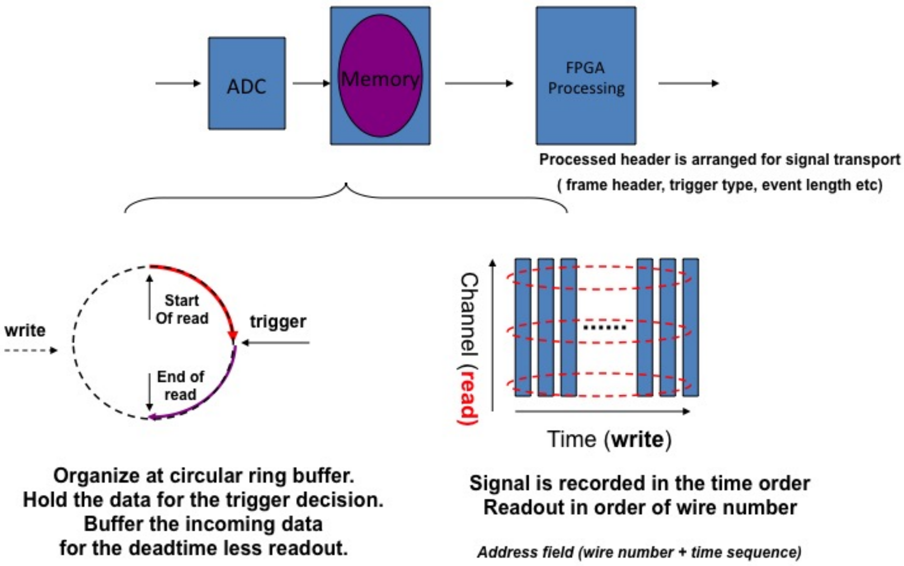

Figure 58: LArTPC readout sequence in the TPC FEM.

which signals, for example, an accelerator neutrino-induced event. When an event trigger is received, 4.8 ms worth of data, relevant to that event, are packeted per channel and sent to the DAQ through the NU data stream. The 4.8 ms readout size is governed by the maximum drift time and spans three or four frames. In order to reduce the amount of data being transmitted, the FPGA trims the three or four frames to span the exact 4.8 ms required, 1.6 ms before the trigger plus 3.2 ms after the trigger. In parallel, the data is continually sent out through the SN data stream, frame by frame. The compression and data reduction algorithms applied to each of the two streams are described in the following section.

After processing by the FPGA, the data passes to the crate backplane dataway on connectors shown in figure 57. A token-passing scheme is utilized to transfer data from each FEM board to the data transmitter module (XMIT) in a controlled way, whereby each FEM, in the order of closest to furthest from the XMIT module, receives a token, transmits its data to the XMIT, and passes the token on to the next FEM in the sequence. For the NU stream, each FEM sends all data associated with a particular trigger number; while for the SN stream, each FEM sends all data associated with a particular frame number. This data transfer is relayed via the otherwise passive crate backplane, and is limited to 512 MB/s. In the XMIT module, the data is buffered temporarily and sent to the DAQ machine through the two streams, SN and NU, which proceed effectively in parallel.

6.3.3 Compression Schemes

In the case of the NU data stream, a lossless Huffman coding scheme implemented in the FEM FPGA compresses the data by approximately a factor of five. Further reduction in the overall rate is achieved by exploiting a PMT trigger in coincidence with the BNB trigger, as described in section 6.5. Huffman coding provides for lossless data compression by taking advantage of the

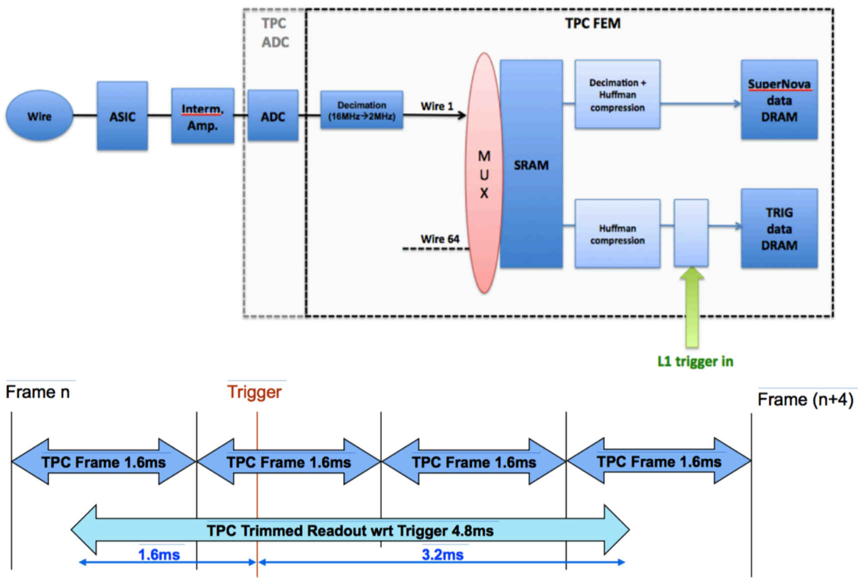

Figure 59: LArTPC trigger readout.

slow variation of the waveform TPC data in any given channel. In particular, this compression scheme relies on the fact that successive data samples on any given wire vary relatively slowly in time. As such, when noise levels are low, any two adjacent data samples either coincide or differ by 1 ADC count. The most frequent values for the difference in ADCs between successive data samples are assigned pre-specified bit patterns with the lowest number of bits possible. Those bit patterns are encoded in the 16-bit data words that would otherwise be used for a single 12-bit ADC sample value. As such, data reduction of up to a factor of 14 is theoretically possible[1]. In practice, the data reduction is sensitive to noise levels and LArTPC activity, and is also dependent on the gain setting. The compression factor achieved by MicroBooNE is shown in figure 60.

Because of the low trigger rate[2], lossless Huffman coding compression proves sufficient for the NU data stream. However, for the continuous SN stream, further compression becomes necessary, resulting in unavoidable data loss. A method called "dynamic decimation" (DD) handles this case. The DD scheme relies on recognizing regions of interest (ROI) in the data stream that contain waveforms corresponding to drift ionization charges. Portions of the data stream not containing ROI contribute to pedestal determination, and ROI are identified as deviations from the continually-updated pedestal, buffered, and read out to disk. At the time of this writing, the MicroBooNE SN stream compression scheme is being finalized and the SN readout stream will be commissioned in September 2016.

6.4 PMT Readout Electronics

The PMT readout electronics are responsible for processing signals from the 32 PMTs described in section 5 and identifying light signatures coincident with the BNB and NuMI beam spills. The

[1]The uppermost two bits are always reserved for header information, in each 16-bit word.

[2]The BNB trigger dictates an upper bound on the trigger rate of 15 Hz.

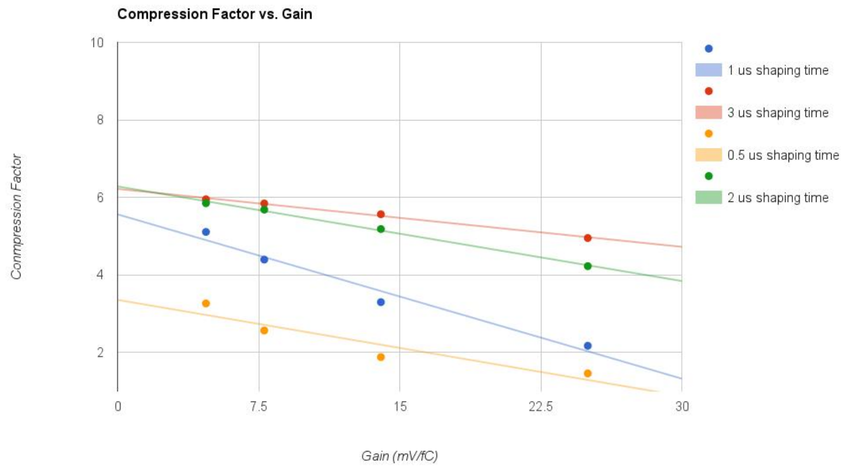

Figure 60: Compression factors achieved on ADC data with Huffman compression.

coincidences generate PMT triggers that can be later mixed with other triggers in the Trigger Board (TB). Signals from the 4 light paddle guides installed in the LArTPC are also recorded by the PMT readout electronics, but these signals do not participate in the PMT trigger generation.

The stages of signal processing are illustrated in figure 61. First, each PMT signal (with the exception of the light paddle guide signals) is split into two different gains, as described in section 5.2.5, with the HG channel carrying 18% of the PMT signal and the LG channel carrying 1.8% of the PMT signal. Each gain is split once again into HG1 and HG2, and LG1 and LG2, in order to allow different processing of beam-related and beam-unrelated PMT signals. All $32\times2\times2$ plus 4 signals are pre-amplified and shaped in 16-channel pre-amp/shaper boards (section 6.4.1). Four PMT readout modules receive the analog shaped signals differentially and digitize them (section 6.4.2) at 64 MHz. The PMT readout modules then process the signals in order to prepare them for shipping to a designated DAQ machine and to form a possible PMT trigger (section 6.4.3).

Each one of the 4 PMT ADC+FEM readout boards used in the PMT readout system handles one of the following:

- Readout of and PMT trigger generation using the HG1 PMT signals associated with neutrino beam events. The paddle signals are also readout by this board.
- Readout of and PMT trigger generation using the HG2 PMT signals that are out of beam time (i.e. cosmic rays and other cosmogenic backgrounds)
- Readout of the LG1 PMT signals associated with neutrino beam events
- Readout of the LG2 PMT signals that are out of beam time

After signal processing, the data is sent to a designated DAQ machine via a transmitter (XMIT) module in the same way as is done for LArTPC data. Two data streams are provided: a NU data

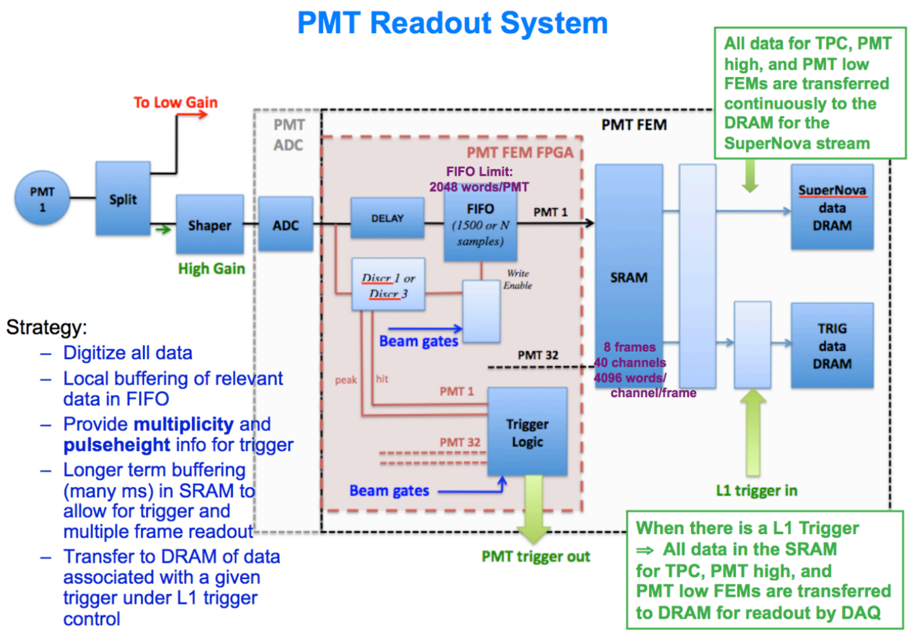

Figure 61: Signal processing in PMT FEM.

stream associated with event triggers and a SN data stream which a continuous version of the NU stream readout.

6.4.1 Signal Amplification and Shaping

The preamp/shaper boards read raw PMT signals from the PMT HV/signal splitters and shape them into unipolar signals with a 60 ns rise time. The shaped signals are sent to the LArTPC readout boards differentially via short front-panel cables, in order to minimize noise, where they are digitized at 64 MHz. The 60 ns peaking time allows digitization of two or three samples on the rising edge. This in turn enables an accurate determination of the event start time (t_0) needed to determine the x coordinates of ionization signals along the drift direction. An accurate time measurement also helps reject other tracks, such as cosmic rays, that cross the detector during the drift time.

6.4.2 PMT Data Digitization

The ADC (Texas Instruments, ADS5272) module part of the PMT readout board (figure 62) is responsible for digitization of up to 48 differentially-driven input signals. The differential signals are digitized at 64 MHz. The 64 MHz clock used by the PMT readout is generated starting from the 16 MHz clock that is common to all readout crates (LArTPC and PMT).

In addition to HG and LG waveforms from the PMTs, each readout board also receives, digitizes, and processes beam gate signal markers which arrive 4μs before the BNB 1.6μs and NuMI 10μs beam gates. These gates are used to (a) specially mark regions of interest where PMT data are read out continuously with no compression and (b) look for coincident PMT light signatures for trigger generation.

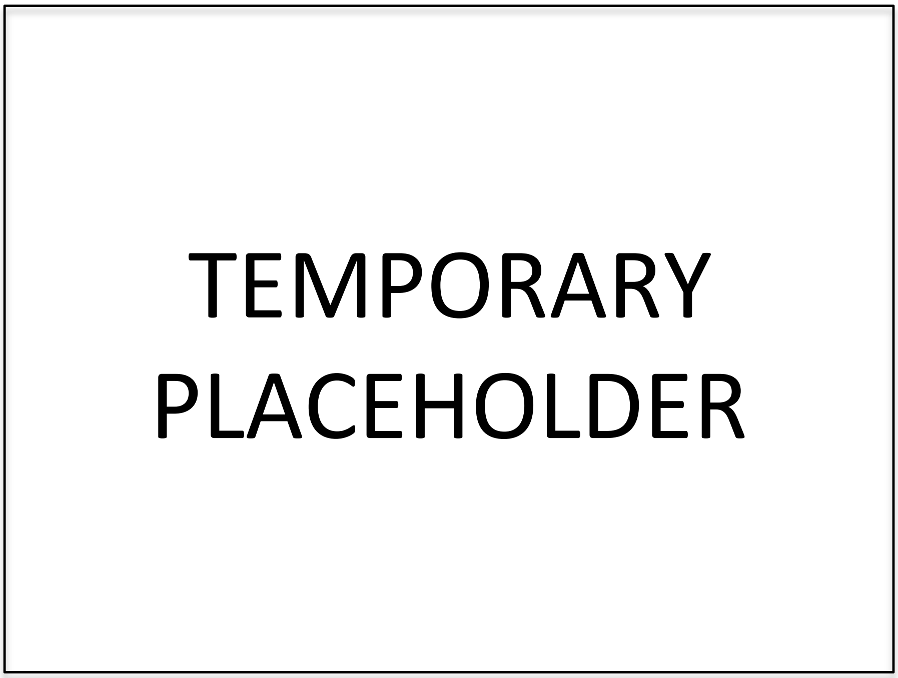

Figure 62: The PMT readout board digitizes 48 input signals. **NOTE: Missing Image!**.

6.4.3 Data Handling and PMT Trigger Generation

PMT information is recorded in the NU data stream for four 1.6 ms frames associated with an event trigger: the frame containing the (asynchronous) trigger, the frame preceding the trigger frame, and two frames following the trigger frame. To avoid the inordinate amount of data that would be generated at a 64 MHz sampling rate, the FEM applies a zero-suppression immediately after digitization, retaining only samples above a given threshold as well as enough information before and after this useful data to establish a local baseline value; this collection of information is referred to as a PMT readout ROI. An exception is formed for beam-related or other likewise-triggered data where, for example, the 4μs-early BNB and NuMI beam gates mentioned in section 6.4.2 instruct readout of 1500 consecutive samples (23.4μs) surrounding and including the beam gates regardless of signal activity.

Two different discriminators are used: one that is active inside the beam gate(s), and one that is also active outside the beam-gate-surrounding 23.4μs. The latter discriminator governs the readout activity due to cosmic rays and other non-beam related activity. The first discriminator enables PMT channels with pulse heights above a configurable threshold (e.g. corresponding to 1 photoelectron) to participate in trigger multiplicity and pulse height sum conditions, as described in the following section. The thresholds for those two discriminators are set to different levels and configured with different dead times for the HG and LG signals.

6.5 Level-1 Trigger Generation

The TB, which physically resides in the PMT readout crate, issues a "Level-1" trigger in order to flag frames that must be treated differently. In the case of the LArTPC readout, the TB flags the 4 frames that must be trimmed and readout through the NU data stream and, in the case of the PMT readout, it flags the 4 frames that must be readout in full through the NU data stream.

The inputs to the TB include a BNB trigger input (maximum rate of 15 Hz), a NuMI trigger input (1.25 Hz), a Fake Beam trigger input (configurable), a PMT trigger input, and two calibration trigger inputs, provided by the laser calibration system and the cosmic ray muon telescope, respectively. The TB also has the ability to receive, via the crate controller, DAQ-issued calibration triggers, which are used explicitly for cold electronics and PMT calibration. The various input triggers can be independently pre-scaled, masked, and mixed together (OR or AND) to generate an event trigger.

The FPGA firmware in the PMT FEM can generate two different types of PMT triggers based on the PMT signals: a cosmic PMT trigger and a beam gate PMT trigger. Beam gate PMT triggers are configured in the same way for the BNB, NuMI, and Fake Beam. The nominal criteria for these triggers are (1) PMT multiplicity $\geq$1 and (2) summed PMT pulse-height $\geq$ 2 photoelectrons (p.e.) summed over all 32 HG1 PMT channels. Both criteria must be met during any 100 ns time interval coincident with the beam spill duration (1.6μs in the case of the BNB and Fake Beam gates and 10μs in the case of the NuMI gate), and only channels enabled by the beam gate discriminator can participate in the active pulse-height and multiplicity sums. The criteria for a cosmic PMT trigger are (1) PMT multiplicity $\geq$1 and (2) summed PMT pulse-height $\geq$ 40 p.e. summed over any one of 28 preset groups of 5 HG2 PMT channels that are grouped based on their spatial correlation. Again, only channels enabled by the cosmic discriminators can participate in the trigger generation.

In addition, a software-based algorithm has been written to mimic the capabilities of the beam gate PMT trigger performed in the FPGA and provide more flexibility in trigger criteria settings. Details of this higher-level software trigger are described in section 6.7.

Figure 63 diagrams the PMT readout and trigger logic. Activation or masking of each of the trigger inputs and outputs is DAQ-controlled. The trigger condition and explicit PMT trigger type, if applicable, is available for every event in the NU data stream at both the event-building stage and offline; this information is read out via a dedicated optical data stream, directly from the TB. The trigger number and trigger time are also propagated and available in the NU data streams arriving independently at the assembler DAQ machine from each LArTPC and PMT crate, and can therefore be used to correctly associate data from the same event.

The readout control sequence is illustrated in figure 64. When a trigger is generated by the TB it is passed to a fan-out module on a single cable and from there it is distributed to all crate controllers (LArTPC and PMT). Through the crate backplane, the trigger gets propagated to each FEM. An FEM that receives a trigger temporarily inhibits the SN stream with its associated decimation and initiates the loss-less readout scheme to direct the data to the appropriate readout path. SN readout resumes once the XMIT is done sending all NU data associated with an event to the DAQ.

6.6 DAQ Design

The MicroBooNE DAQ system acquires data from the readout electronics, writes data to local disk before transferring it to long-term storage, configures and controls the readout electronics during data-taking periods, and monitors the data flow and detector conditions. These tasks are performed on a network of commodity servers running both custom and open-source software.

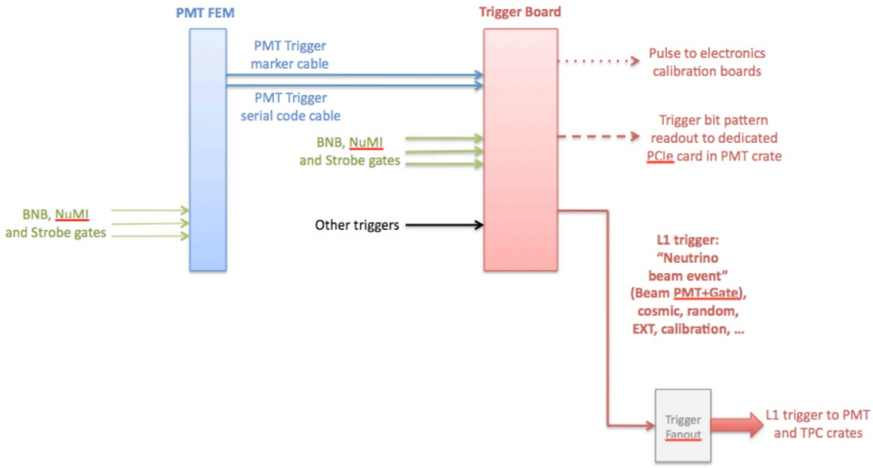

Figure 63: PMT readout and trigger logic.

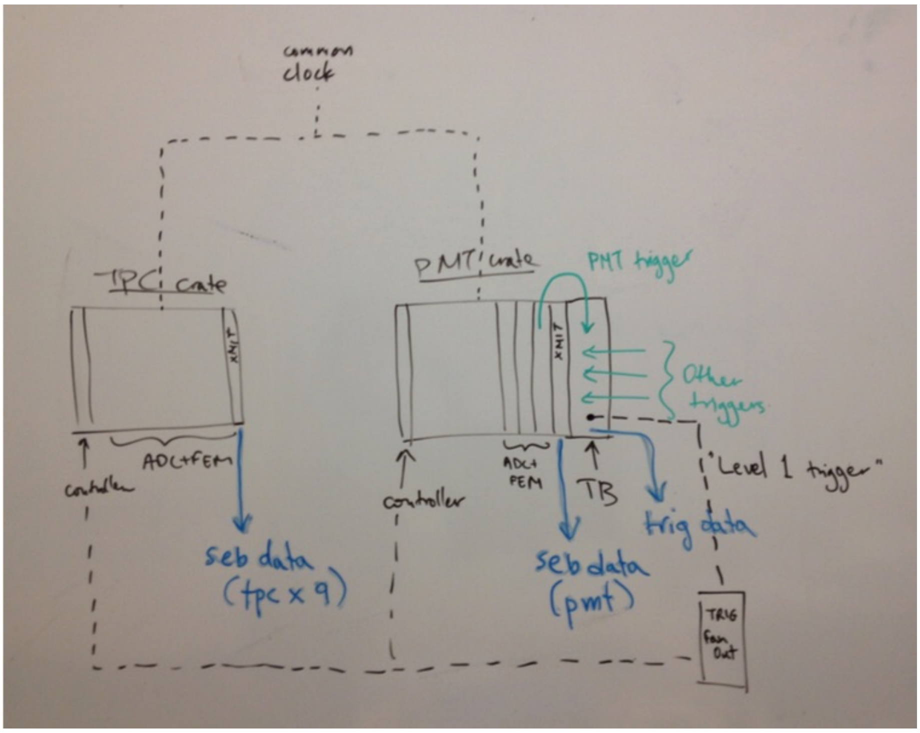

Figure 64: Readout control sequence. The MicroBooNE Level-1 trigger is a hardware trigger which consists of the OR between a BNB, NuMI, and EXT (strobe) trigger. Once received, the Level-1 trigger is propagated to all readout crates and instructs PMT and TPC data readout into ten dedicated sub-event buffer DAQ machines. The data across different DAQ machines is correlated at event building stage by the trigger number and corresponding trigger frame and sample numbers recorded in each data stream, per event. All readout crates are synchronized and correlated to the same, 16 MHz clock. **NOTE: Placeholder figure!**.

The data from each crate of the backend electronics is sent to a dedicated server (called the sub-event buffer, or SEB) via an optical fiber, arriving in a card on the SEB's PCIe bus. A real-time application places these data in an internal buffer, collects all segments belonging to an event, and creates a sub-event fragment that may be routed to a specified destination. For the NU stream, in which the data arrives with every trigger, these fragments are sent to a single event-building machine (EVB) over an internal network. Full events are checked for consistency and written to local disk on the EVB before being sent offline for further processing. A high-level software trigger, described in section 6.7, is applied to the data to determine whether events should be written locally or ignored. For the SN stream the data remains on the SEB where it is written to disk and only sent for offline analysis on explicit requests.

Data writing to either triggered or SN streams is limited by the RAID6 disk write speeds which are roughly 300 MB/sec. This is much less than the network bandwidth bottleneck, which is 10 Gbps. The 300 MB/sec disk write speed therefore sets the maximum aggregate rate at which all SEB fragments can ship data to the EVB without loss of data. With Huffman compression, which gives a data reduction of approximately a factor of five (figure 60) and the PMT trigger, which reduces the data rates by another factor of > 70, this is more than sufficient for MicroBooNE's maximum 15 Hz beam spill rate. MicroBooNE expects a total triggered write rate of around 12 MB/sec. The SN stream circular buffers, which will be aggressively (non-losslessly) compressed beyond what the triggered stream experiences, will fill each server's 14 TB in on the order of one day, which is ample time to respond to a Super Nova Early Warning System (SNEWS) alert [102].

After data is written to disk, it is then copied to another server on the internal DAQ network, where the raw data is further compressed, shipped, and queued to be stored on in tape and disk cache using the Fermilab central data management system known as SAM. Offline applications then begin processing the raw data, converting the binary data format into a LArSoft ROOT-based format which can be used as input for reconstruction algorithms. A separate process collects beam data and, during binary to LArSoft conversion, inserts that data into the built events. A duplicate copy of the data is also stored offsite at Pacific Northwest National Laboratory (PNNL). This collection of approximately 15 "projects" and the database which holds and monitors the state of the data flow is known as the Python/Postgres for MicroBooNE Scripting system (PUBS), and is patterned after a similar database state machine that the Double Chooz experiment used for data management. As PUBS pushes the data through this process, the progress of each project is monitored and viewable via GUI. PUBS can also monitor the state of the SN stream data, held locally on the SEBs. A separate offline PUBS instance controls the processing of the data, including applying newly calculated calibration constants as part of data quality management. Figure 65 schematically depicts the flow of data throughout the MicroBooNE DAQ system.

Additional software components handle the management of the main DAQ processes moving the data. A run control application issues configuration and state-progressing commands to the SEBs and EVB. Configuration states are stored in a dedicated run configuration database, which allows for the setting and preserving of configuration information for the DAQ, readout, and additional components. This database not only allows for creating the large ($\sim$200 parameters) intricate DAQ run configuration files, but also enforces certain conditions which must hold for consistency. For example, the configuration that initiates the ASICS charge-injection calibration also dials and captures the settings on the external pulser that drives the calibration signal and assures that ASICS

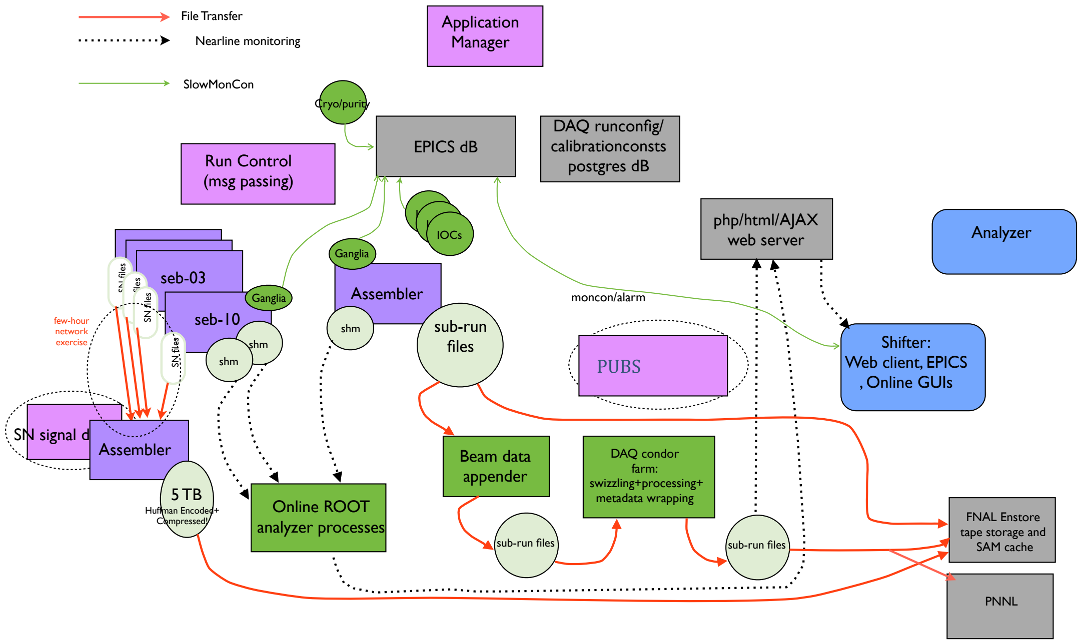

Figure 65: Data flow for MicroBooNE DAQ from raw to processed.

gains and peaking time parameters are enforced and recorded.

Another important aspect of the system is monitoring the health of the DAQ. Monitoring of DAQ components is accomplished through Ganglia which monitors basic system states (such as CPU, memory, and network usage) as well as allows use of custom metrics to monitor the data flow and status of the readout electronics [103]. These metrics are sampled and collected by the EPICS slow monitoring and control processes, which archives desired quantities and provides alarms when pre-defined thresholds are exceeded [104]. Some examples of Ganglia metrics that are monitored and alarmed in EPICS are the rates of growth of the SEB data buffers, the fragment rates leaving each SEB, and fragment arrival rates at the EVB. Figure 66 shows examples of Ganglia metrics.

Additional online monitoring exists to check data quality in more detail, through both programmed checks and visual checks including a real-time event display. The online monitoring takes snapshots into shared memory segments on the SEBs and the EVB, and thus provides the desired low latency checks of newly-arriving data. It continually walks through these ≈ 150 MB snap-shotted events and outputs histograms of occupancies and rates which are saved in ROOT files [105]. The histograms are then displayed in a web-based monitoring system that is easily accessible by the shift crew. Channels are aggregated in a variety of formats, including the order in which they appear in crates or across the wires and PMTs themselves. In this way, potential problems across connectors or crates, for example, may be more readily identified. Noisy, quiet, and unresponsive channels are easily marked and displayed to the shift crew. Figure 67 shows an

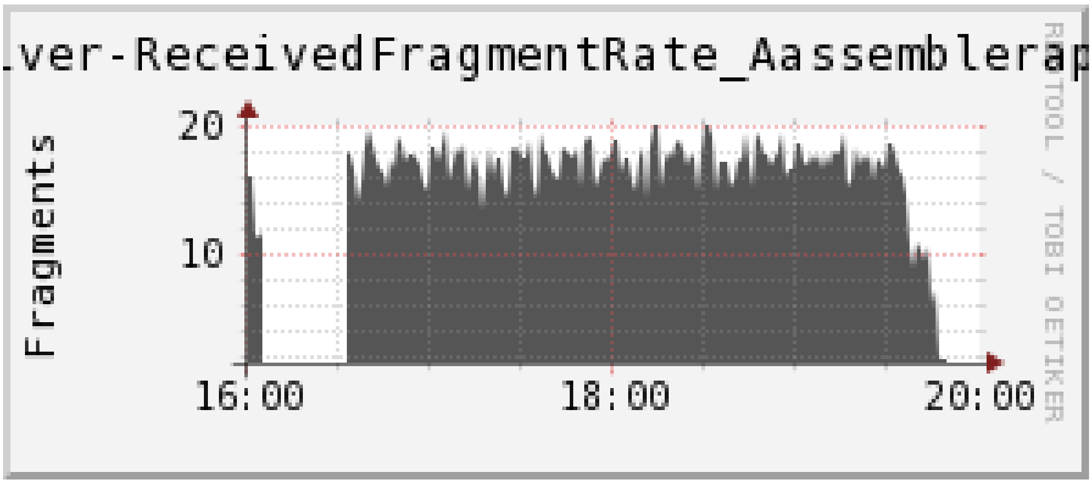

Figure 66: Ganglia metrics showing data flow on the EVB machine during a 2 Hz test run. (ul) the event disk write rate (ur) The number of assembled queued-up events waiting to be written (ll) The total EVB received data rate, and the (lr) received fragment rate.

12 example of available online monitoring information.

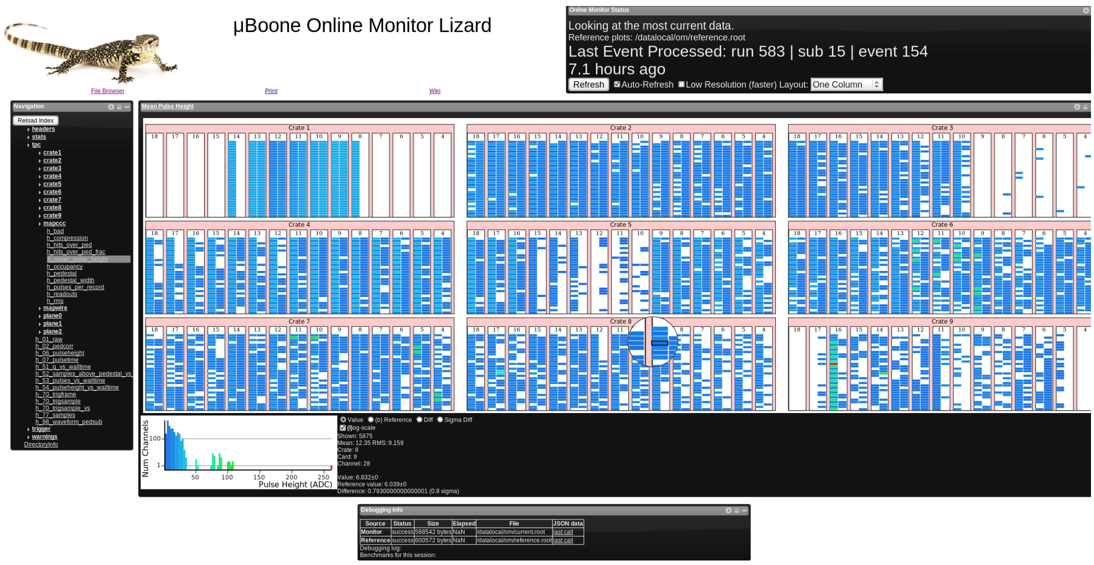

Figure 67: The online monitoring GUI (Lizard). The pedestal-subtracted ADC values for all 8256 wires in one minimum bias event are shown. Each box is a channel. Not all crates are fully populated with electronics.

13 ## 6.7 High-level software trigger

14 After events are collected on the DAQ event-builder server, a suite of trigger algorithms are applied
15 to the data. Currently, these algorithms mimic the PMT readout electronics' FPGA-based beam
16 gate trigger algorithms, described in section 6.5. A search over the PMT digitized waveforms from
17 the beam-spill period is performed, and if there is a significant amount of light in coincidence

with the expected arrival time of the neutrinos, the event is marked and saved. This selection is performed on data that passes the level-1 trigger, which typically includes data from the BNB and NuMI beams, and randomly selected off-beam data from an “external" trigger. A fraction of the data from each of these level-1 trigger input streams is also retained via a random prescale, which provides a selection of data that has not been biased by the trigger. The high-level trigger algorithms take approximately 10 ms to return a result, a latency that is well-below the event-taking rate and so does not impact data-taking performance. The average pass rate for data-events in the PMT beam gate trigger algorithm is roughly 5%.

7. Infrastructure and Monitoring Systems

MicroBooNE is housed at LArTF, which is located on-axis to the BNB. Complete knowledge of the electrical and cryogenic systems housed within LArTF is necessary to maintain acceptable operating conditions for the experiment. Continuous monitoring of the beam being delivered to LArTF is also necessary for subsequent physics analyses. This section describes the details of infrastructure within LArTF, as well as monitoring of the experiment and beam conditions.

7.1 Electronics Infrastructure at LArTF

This section describes the electronics infrastructure of the experiment, which is essential for proper operation of the electronics that control the functioning of and extract data from the LArTPC, PMTs, and other detector subsystems. Figure 68 shows a diagram of this system at LArTF, depicting racks located on a platform directly above the cryostat that house electronics for: LArTPC control and readout, light collection system, drift high voltage, purity monitor, calibration laser, trigger, and cryogenic control systems. Additional server racks containing the data acquisition, beam timing, and external network electronics are located in a separate computer room above and adjacent to the above-cryostat platform. The distribution of power, data, and network connections to and from all of these racks are also presented in figure 68, and is described in more detail in the following sections, as are electronics safety systems and interlocks.

7.1.1 AC Power Distribution and Grounding for Low-Noise LArTF Data-taking

As with any large detector operating with a high dynamic range, prevention of electromagnetic interference and its attendant effects on MicroBooNE data is an essential aspect of detector design. MicroBooNE’s strategy for producing a low-noise environment for the LArTPC and associated readout electronics can be largely summarized in a few key points. AC power distribution-related items will be described here, while cabling, connections, and shielding will be described in a following section.

- ‘Clean power,’ or AC power electrically isolated from AC power for the rest of LArTF (‘building power’), is supplied to all sensitive electronics via an isolation transformer.

- Highly sensitive electronics are housed inside the Faraday cage provided by the detector cryostat or inside Faraday cages directly grounded to the cryostat.

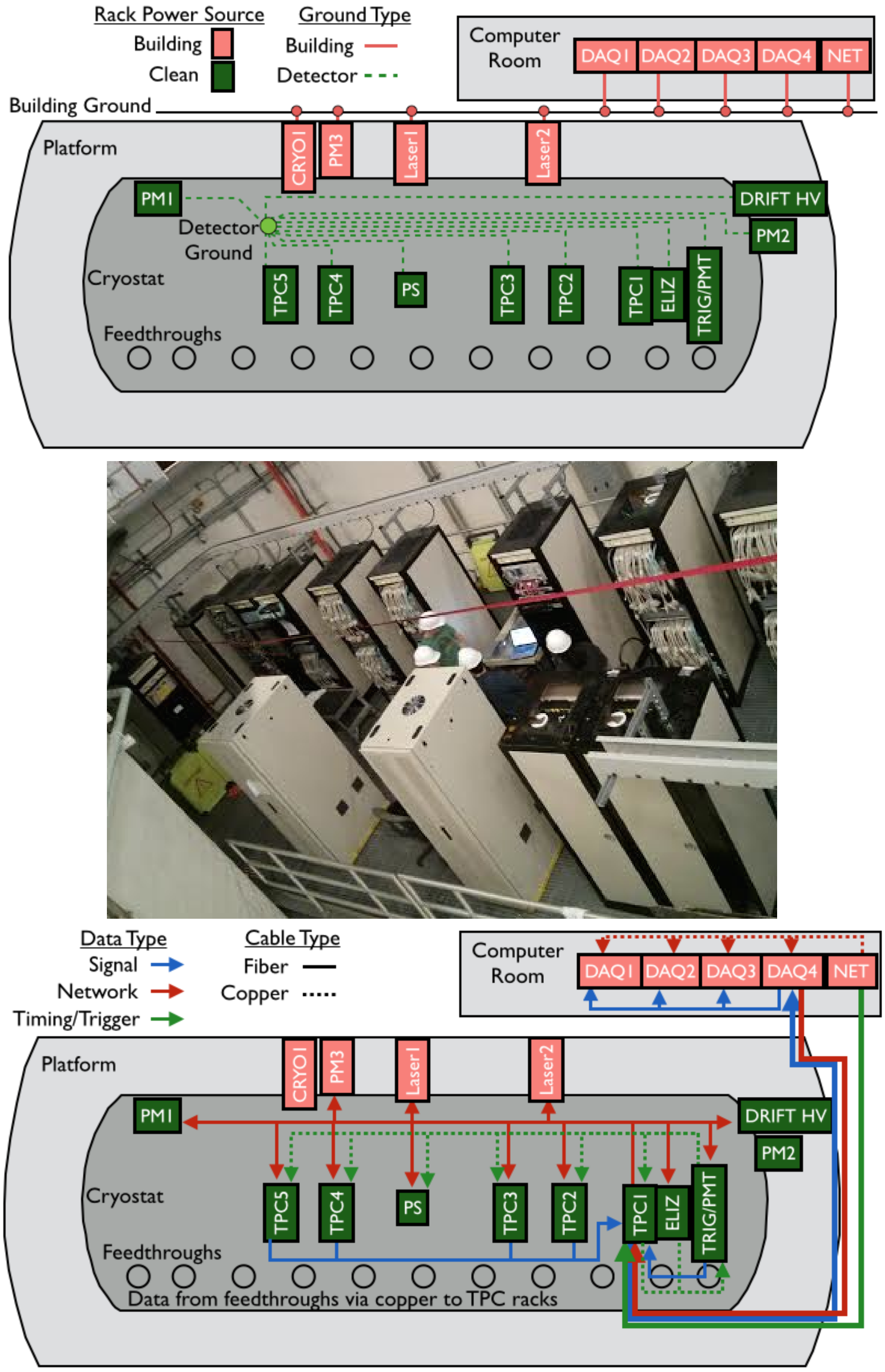

Figure 68: Top: Diagram illustrating location of deployed electronics racks and separation of detector and building grounds and clean and building power for differing racks. Middle: Photograph of installed electronics racks on the LArTF platform. Bottom: A diagram illustrating the general scheme of signal, network, and timing signal cabling in the LArTF computer room and platform.

- The detector cryostat is grounded to a 'detector ground,' which is physically and electrically isolated from the ground provided to all other LArTF power circuits, or 'building ground.'

- No direct electrical connections are present between detector ground and building ground. This is accomplished through the use of insulating platform and cryostat saddle materials, insulating cable trays and cables, and by inserting insulating 'breaks' (i.e. fiber data links or insulating cryo pipe sections) when connections between sensitive and potentially noisy detector components are necessary.

- Indirect pickup on clean signals through capacitive coupling to adjacent noise sources is minimized through use of detector-grounded shielding and electrically-insulating cable trays.

- Ground loops on detector ground are avoided wherever possible by connecting all electronics racks directly to the cryostat and by minimizing direct electrical connections between racks.

- Direct or capacitive couplings between building and detector ground are constantly monitored during installation and operation with a custom-designed impedance monitor.

A line drawing describing the production of clean power and clean ground are shown in figure 69. Two 200-Amp clean power circuits produced at isolation transformers are used to power all sensitive racks, which are indicated in figure 68. All racks containing LArTPC readout electronics are placed on one circuit, while all other sensitive equipment is placed on the alternate circuit. On the platform, all racks utilize clean power with the exception of the calibration laser and in-line purity monitor racks, which either contain noise-producing elements or support building-grounded components. All racks in the LArTF computer room utilize building power.

208-3phase power is distributed to each individual electronics rack. For racks with significant power requirements or a large number of components, this power is delivered to a Fermilab-designed 'AC switch box,' which distributes power to an Eaton Power Distribution Unit (PDU) only upon receiving an interlock signal from a smoke detection system in each rack, which will be described in more detail below. Rack components then receive power from one of the three phases on this PDU. For racks with fewer requirements, power is supplied to components directly from an interlocked simplified AC switch box or SurgeX SX-1120-RT PDU. Racks with sensitive electronics are grounded to the cryostat via copper sheeting running throughout insulated cable trays above the cryostat. Sensitive components within each rack are connected to a tin-plated copper grounding bar electrically connected to the rack bottom and running the height of the rack. Mechanical attachments to the rack provide grounding for less sensitive rack components. As mentioned before, any unintentional direct connection between building and detector ground can be quickly identified by the impedance monitor located on the LArTF platform.

7.1.2 DC Power Distribution to the MicroBooNE Detector

DC power is provided to the LArTPC and readout electronics by power supplies in clean-powered, detector-grounded racks for a variety of purposes:

- Holding the LArTPC cathode plane at voltage to produce the desired ionization electron drift speed

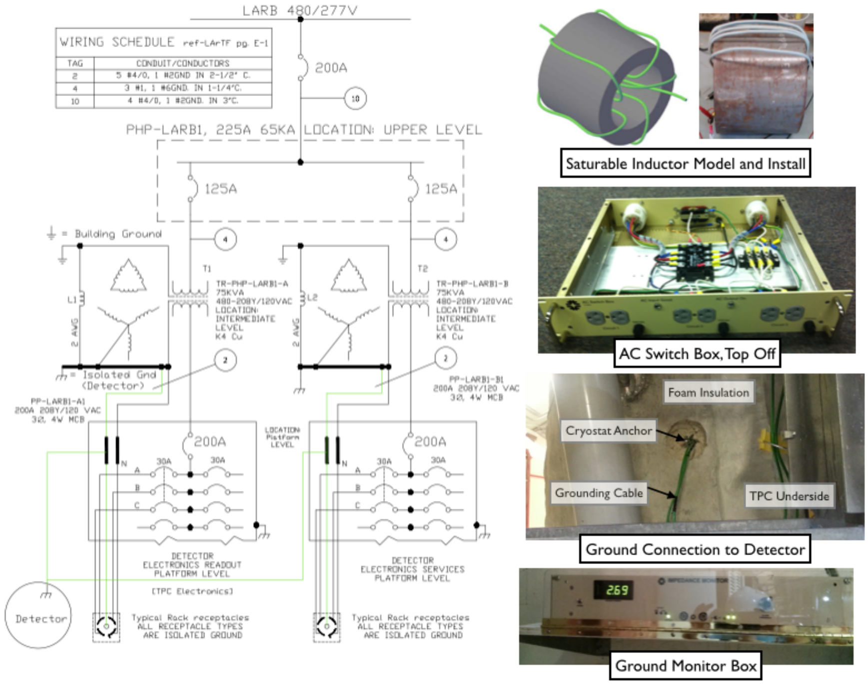

Figure 69: Line drawing of clean power generation and distribution and connections to detector ground, along with pictures of the installed saturable inductor (top), AC switch box (top middle), detector ground strap and connection (bottom middle), and impedance monitor (bottom).

- Holding the two ungrounded anode planes at the proper constant voltage to ensure the planes are transparent to drifting electrons
- Operating the light collection system PMTs
- Powering the cold electronics located inside the LArTPC
- Powering the warm electronics located in the LArTPC readout electronics racks
- Powering auxiliary systems, such as LArTPC temperature sensors and purity monitors

Table 7 summarizes the required voltages or currents for each of these purposes as well as the power supply make and model utilized in each case. Power supplies are located in the relevant subsystem's electronics rack, with power and grounding connections as dictated by that rack.

DC supply power consumption is minimal in most cases, with the exception of the warm LArTPC electronics PL-508 supplies, which can draw in the vicinity of **XXX** W during normal operation. Care was taken to distribute the AC power load by limiting the number of high-draw PC supplies per electronics rack.

7.1.3 Network, Timing, and Data Distribution for Low-Noise LArTF Data-taking

Network, timing, and data connections must be made between the detector, building-ground, and detector-ground racks to properly read out MicroBooNE data. However, as described above, these

Table 7: Overview of MicroBooNE DC power distribution. Delivered voltages or currents are listed, along with power supply makes and models and whether each supply utilizes clean or building power.

Sub-System	Supplied Value	Supply Made/Model	Clean Power?
Drift High Voltage	120 kV	Glassman LX150N12	Y
Anode Plane Voltage	1 kV / 8 mA	Wiener MPOD ISEG_EHS 82 10X_805F	Y
PMT High Voltage	2 kV / 3 mA	BIRA T4	Y
Cold Electronics Power	8 V / 10 A	MPOD MPV 800l	Y
Warm LArTPC/PMT Electronics	+/-5V MDH 2-8V/25A +12V MEH 8-15V/92A +3.3V MEH 2-7V/115A	Wiener PL508	Y
Auxiliary Systems Power	Various	Various	Laser: N Inline PM: N Cryostat PM: Y

connections must be made while maintaining strict detector-building electrical isolation. Deployed interconnections meeting both of these requirements are displayed in figure 68.

Timing and LArTF-external network signals are brought into LArTF via electronics in the computer room, where all racks are building grounded and powered. These signals are distributed and processed in the computer room via copper cable, while network and processed timing signals to be sent to the platform are converted onto fiber cables and aggregated into a central fiber termination box. A fiber trunk line then delivers these signals to the platform, where another fiber termination box on a detector-ground rack is used to fan out these signals. Network connections are fanned out via fiber to a network switch in each platform rack, while timing signals are re-converted to copper and further processed for use by the trigger system on a different detector-grounded rack. All rack-to-rack cables are run in insulating cable trays beneath the platform.

PMT and LArTPC data are transferred from each detector feedthrough to readout crates in detector-ground racks via insulated copper cable whose shield is tied to detector ground. Digitized crate output is then sent to the aforementioned platform fiber termination box, where these signals are sent via fiber trunk line to the computer room. In the computer room, these fibers are then fanned out to the appropriate DAQ computer. Readout crate and cold electronics control commands are transmitted in the opposite direction utilizing a similar scheme, with crate controls delivered directly via fiber, and cold electronics commands delivered via ranger fiber to a copper fanout in a detector-ground rack.

Clock and trigger signals must also be sent from a central trigger rack to all detector-ground LArTPC/PMT readout racks. These signals are transmitted via copper connections, and represent the only source of ground loops on detector ground. To further reduce the possible impact of induced noise in these and all copper cables mentioned above, all insulating cable trays beneath the platform are lined with copper sheeting grounded to the detector. As an additional precaution, all LArTPC signal copper cables are run in separate cable trays from power and auxiliary cabling beneath the platform as well as inside every rack.

All cables between all detector components have been uniquely labelled with serial number, source, and destination to allow for ease of replacement and reconnection. Ample fiber and copper spares for every major cable type are also installed along with the production cables to allow for quick replacement of any failed cable.

7.1.4 Interlocks and Safety Systems

All electronics racks contain smoke-sensing and temperature-monitoring systems, which, when interlocked with AC and DC power transmission in each rack, constitute a rack protection system (RPS) designed to meet Fermilab safety requirements and reduce the risk of fire and related damage in LArTF and to individual rack components.

The RPS principally consists of a smoke sensor connected to a Fermilab-designed rack protection box. This box produces and outputs a 12 V interlock signal when the rack protection box is on and receiving a 'no-smoke' signal from the smoke sensor. This 12 V signal can be sent to the AC distribution box located in each rack, as described above, to allow AC transmission to all rack components only if the RPS is on and not detecting smoke. A similar 12 V 'RPS Status' signal is also produced by the RPS box for input into the MicroBooNE slow control box, which will be described in following sections. Alternate contacts are available on the rear of the RPS box for coupling the status of additional subsystems, such as the DAQ and calibration laser uninterruptible power supply (UPS), to smoke sensor or rack power status.

Temperature sensors deployed in two or three locations in each electronics rack sample air temperature within each rack. Temperatures at each sensor are read out and recorded in the slow-control database by the slow-control monitoring box. In addition, the box also produces a 5 V interlock signal if all sampled temperatures are within pre-programmed thresholds. In electronics racks distributing PMT- or LArTPC-related DC power these temperature interlock signals are input into each relevant power supply, allowing DC power distribution only when this interlock signal is present, for safety purposes.

Additional hardware interlocks ensure the non-simultaneous operation of particular subsystems. In particular, the PMT system is disabled when cryogenic system liquid level sensors detect a level below that of the highest PMT bases, or when the UV laser system is active. The former requirement is enforced with a dry-contact hardware interlock, while the latter is enforced with a software interlock in the MicroBooNE online software.

7.1.5 Performance Measurements

The proper operation of each production electronics rack's AC and DC distribution and RPS systems has been tested prior to installation at LArTF. Furthermore, test stands exercising functionality of DAQ, PMT and LArTPC electronics, trigger, and drift HV systems have successfully incorporated and tested various aspects of these same AC and DC distribution and RPS systems. Impedances between detector and building grounds were recorded throughout the installation of the rack infrastructure at LArTF using the impedance monitor located on the LArTF platform.

7.2 Slow monitoring and control system

MicroBooNE uses the Experimental Physics and Industrial Control System (EPICS) [104] for controlling and monitoring most devices and conditions important to the experiment. These include power supply controls, temperatures, fan speeds, rack protection interlock status, and various environmental conditions. The DAQ, cryogenics systems, and beam data collection systems operate independently of the EPICS slow monitoring, but export data which are imported into EPICS for archiving and status displays. Applications from the Control System Studio software collection [106] are used for providing displays, alarm notifications, and data archiving.

An EPICS system consists of any number of server programs implementing the EPICS Channel Access (CA) protocol [107] to provide client programs access to any number of process variables, where each process variable represents a quantity being controlled (an output) or measured (an input). The EPICS base distribution provides a standard type of channel access server called an Input/Output Controller (IOC), which can be extended to support specific hardware as desired.

Most power supplies are controllable over the network through the NetSNMP protocol [108]. Several EPICS driver modules are available for SNMP, and MicroBooNE utilizes one written at NSCL [109]. An IOC with this SNMP module runs on a central computer and contacts the power supplies over a private network for monitoring and control. The photomultiplier power supplies are reused from the D0 experiment and have custom IOCs running in their own controllers. The main high voltage power supply has only a simple RS-232 serial interface; control and monitoring for it is provided by a nearby computer running an IOC with the EPICS asynDriver [110] and StreamDevice [111] modules.

MicroBooNE has a number of racks in various positions above the detector and in an adjacent server room. Each is equipped with a rack-protection system and multiple digital temperature sensors, and most contain one or two fan packs, each containing 6 fans. To monitor and control these devices, each rack has an 1U rack-mount enclosure containing an ARM-based single-board computer (SBC) running Linux. An off-the-shelf GESBC-9G20 from Glomation Inc. [112] is utilized for the SBC. A custom interface board [113] connects the SBC to front panel LEDs, temperature probes, fan packs, and rack-protection-status input. The temperature sensors are DS1621 chips, controlled and read out over an I2C bus by the SBC's I2C controller. The DS1621 also has a thermostat output with programmable trip and reset temperatures, which are connected via the interface board to outputs that can be used to interlock devices in the racks, such as power supplies. The fans provide pulse-per-rotation outputs, which are monitored by a 12-channel tachometer implemented via a PIC16F887 microcontroller, and also read out by the I2C bus. An EPICS IOC runs in each SBC, with custom device drivers for reading all status information and controlling the heartbeat LED and temperature sensor trip and reset points.

Data are imported into EPICS channels from a number of external sources. The primary reason for duplicating these data in EPICS is to integrate displays and warnings into one system for the experiment operators, and to provide integrated archiving for sampled data in the archived database. An IOC running on a central computer provides "soft" process-variables channels for these data. The data acquisition system provides many metrics describing its operation via the Ganglia system[103, 114], which makes the data available in an XML format easily read by a Python script, which in turn writes to EPICS using the PyEPICS module [115]. The hardware and system status of the DAQ computers is monitored through the industry standard Intelligent Platform Management Interface (IPMI); rather than writing a script to import data from IPMI directly into EPICS, a IPMI-to-Ganglia interface provided by the FreeIPMI's "ipmi-sensors" package [116] is used, allowing data to be imported via the same mechanism used for the DAQ metrics. Separate Python scripts periodically retrieve data about outside weather conditions from various sources, cryogenics system data from a file retrieved non-intrusively from the IFIX cryogenics control system, and beam data from Fermilab's Intensity Frontier Beam Database (IFDB) [117].

7.3 Beam Monitoring

The primary source of neutrinos for the MicroBooNE experiment is the BNB. The primary beamline is lined with instrumentation including toroids which indicate beam intensity, "multiwires" showing beam profile in the horizontal and vertical planes, and beam position monitors measuring the mean beam position. Data from these monitors are stored on a spill-by-spill basis in the IFDB. Many of MicroBooNE's physics analyses require that beam data are recorded for each spill and matched to detector events.

Primary beam monitoring in MicroBooNE is done using a "dashboard" interface to IFDB. By using the IFBD instead of the accelerator control system, the experiment can also verify that data are being acquired by the IFBD. The dashboard is accessible over the network using a web browser. The final monitoring step includes a post-data-merge check, ensuring that beam data are successfully matched with detector data for all beam spills. This is done once the detector DAQ binary data file is closed.

The dashboard presents a graphic representation of the data, allowing for easy error identification, as shown in figure 70. The experiment monitors: two toroids which indicate beam intensity; three multiwires, each of which shows beam profile in each plane; and beam position monitors along the beamline which show the vertical and the horizontal position. Parameters pertaining to the target and horn, such as cooling air temperature and horn current, can also be monitored. The dashboard allows the experiment to easily add additional devices if experience demonstrates the need for their monitoring.

Data are monitored in near real-time. A reasonable history is also kept so that changes are easily identified. The accelerator control system provides detailed diagnostics tools to experts and can be used in case of any problems.

8. UV Laser System

The knowledge of the electric field inside the drift volume of a LArTPC is a necessary aspect for performing subsequent event reconstruction. Distortions of particle tracks due to field non-uniformities affect the accuracy of the particle momentum reconstruction based on multiple scattering. Deviations from a uniform drift field may arise mainly due to accumulation of positive argon ions in the drift volume. These ions are produced by ionizing particles from neutrino interactions, as well as by cosmic rays. While electrons produced by ionizing particles are quickly (within few milliseconds) swept towards the readout system, ions have significantly lower mobility. Their drift velocity in the MicroBooNE detector at nominal drift field is of the order of 0.8 cm/s. The rate of cosmic muons in the LArTPC volume is estimated to be 11,000 muons/s within the active volume

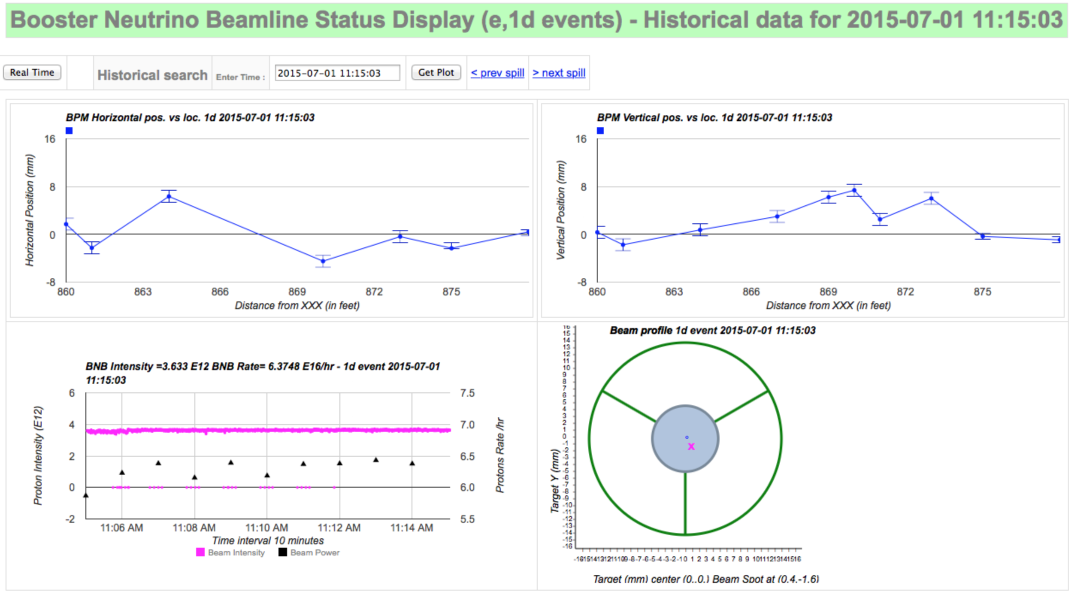

Figure 70: The BNB dashboard, showing graphical representation of beam instrumentation data, is used to monitor the beam. The top box shows the timestamp of the beam spill and indicates if data is stale by changing the color. The two top plots show the primary proton beam position along the BNB. The bottom left plot shows the recent beam spill intensity and rate. The bottom right plot shows the beam as projected onto the Beryllium target (the grey circle in the middle with radius of 0.5cm). The dashboard is accessible via web page providing both real time updates and the review of past data. The page can be easily extended to monitor additional beam devices.

(assuming a cosmic rate of 200 muons/m^2/s through a horizontal plane at the earth's surface and 63 muons/m^2/s through a vertical plane), traversing a combined length of 1.9×10^4 m through the liquid argon. Assuming that cosmic muons are minimum-ionizing (2.1 MeV/cm) and produce 23.6 eV per ion pair, positive ion charge is produced at a rate of 2.8×10^{-8} C/s in the MicroBooNE TPC. These ions are continuously neutralized at the cathode. The resulting charge distribution in equilibrium is shown in figure 71. Such accumulated space charge leads to noticeable distortion of the drift field and, consequently, to deviations of reconstructed track coordinates by up to 10cm (see figure 72). The ion drift velocity is comparable to local argon flow velocities, produced by global argon recirculation flow and thermal convection. Therefore the distribution of positive space charge inside the drift volume may be not only nonuniform (figure 73), but also non-stationary.

A nonuniform drift field in the LArTPC leads to bending of initially straight tracks of high-momentum ionizing particles. In principle, a set of events from such particles allows for the reconstruction of the field in any small region of the LArTPC drift volume, using the systematic apparent curvature of tracks at different angles passing through that region. In practice, the rate of such events from cosmic muons is too low to acquire sufficient statistics in reasonable time. A method to generate straight ionization tracks at a defined location in liquid argon is described in [118]. A collimated photon beam from a pulsed UV laser with λ=266 nm can ionize liquid argon via multi-photon absorption. The resulting ionization track is straight, characterized by low

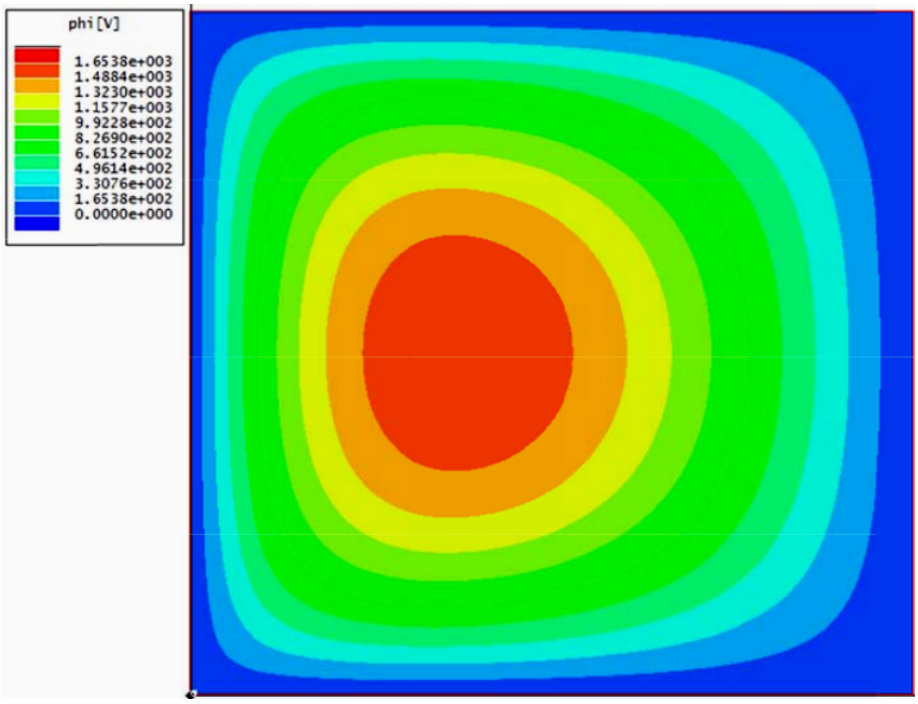

Figure 71: Distorting potential distribution due to positive space charge in equilibrium in the MicroBooNE detector.

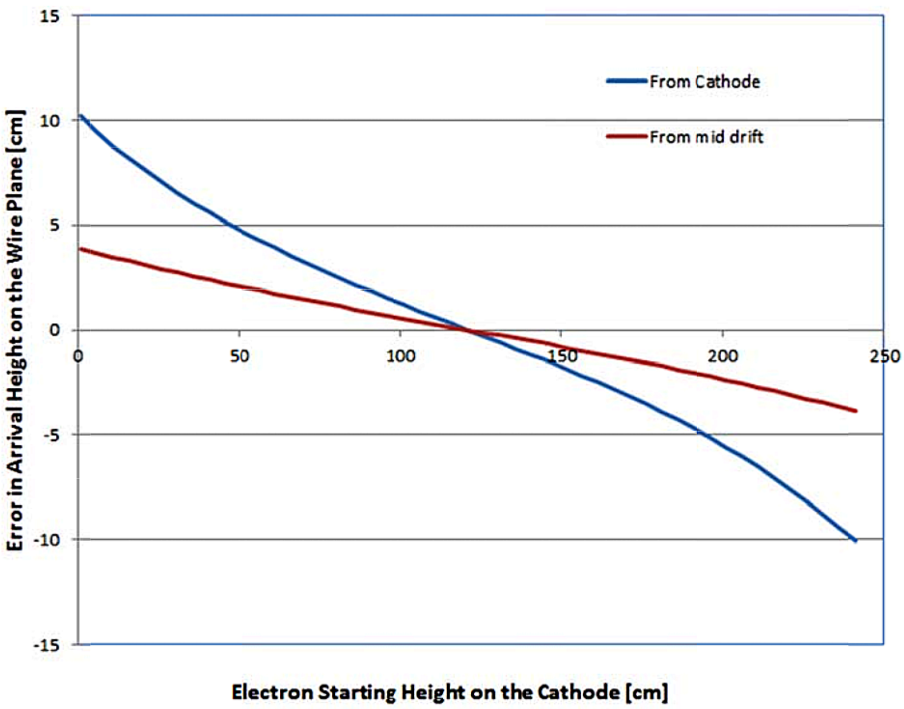

Figure 72: Deviation of a crossing track from its true coordinates due to positive ion space charge.

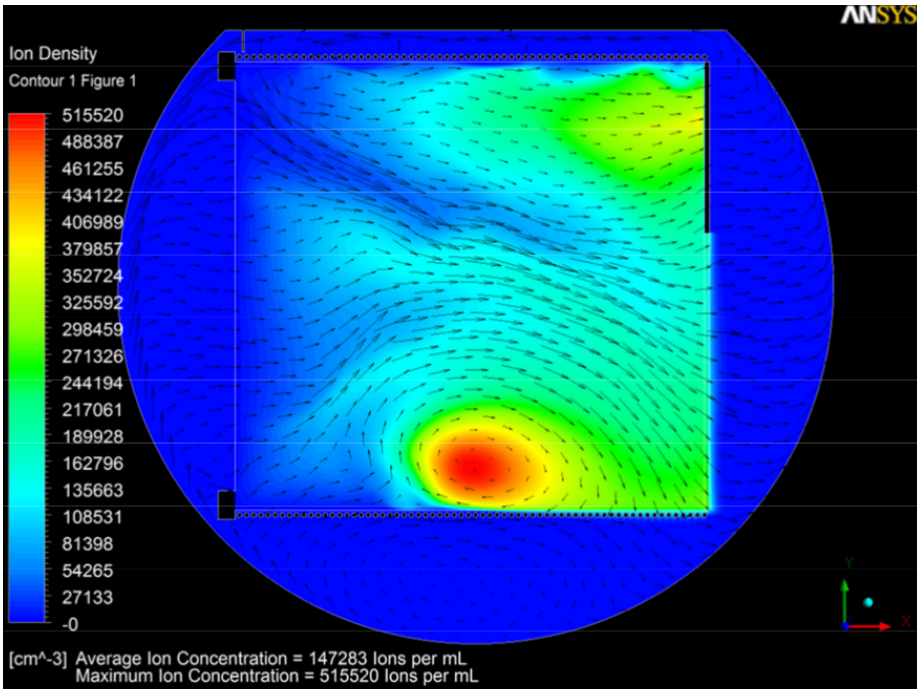

Figure 73: Distribution of the positive space charge in presence of argon circulation.

electron density, therefore featuring little charge recombination loss, unlike cosmic muon tracks. Laser tracks are also free from δ-electrons, which complicate track reconstruction in the case of muons. The method was successfully exploited in the Argontube long drift LArTPC [119 – 121] to derive the non-uniformity of the electric field along its 5 m long drift volume (see [122]). The MicroBooNE LArTPC requires a set of such tracks in order to cover the whole sensitive volume to reconstruct field distortions. Tracks are generated one at a time by steering a pulsed laser beam with the use of a custom-designed opto-mechanical feedthrough (see [123]). The pulse rate of the laser generator is 10 Hz. This allows production of a minimum required set of 100 tracks within one minute (taking into account steering time). Details of this solution are described in the following sections.

8.1 UV Laser Calibration

In order to unambiguously reconstruct a drift field vector at any point within the detector fiducial volume, a minimum of two ionization tracks are required to cross in the region of interest. The total number of crossing points is determined by the required reconstruction granularity. In MicroBooNE the initial scenario is to acquire 100 tracks from each direction, producing a reconstructed 3-D map with voxels that are approximately 10x10x50 cm^3 in volume. This map provides a rough picture of the space charge distribution. Depending on the results of this measurement, areas of interest can be studied in more detail. Repetitive study of small volumes may reveal dynamics in the space charge distribution due to turbulent circulation, and should further inform an optimized scenario for a standard UV laser calibration procedure.

An algorithm of drift field calibration utilizes an input array of detector events with one straight ionization track in each element of the array. The result of the calibration is a coordinate correction map, to be applied to each track, which converts apparently curved track images back to the true coordinate system where they are straight. The algorithm is iterative with an optimizable iteration step and required accuracy. An example of simulated reconstruction in 2-D space is depicted in figure 74, showing that the magnitude of the field distortions is reduced from 10 cm down to several millimeters in 99% of the detector volume.

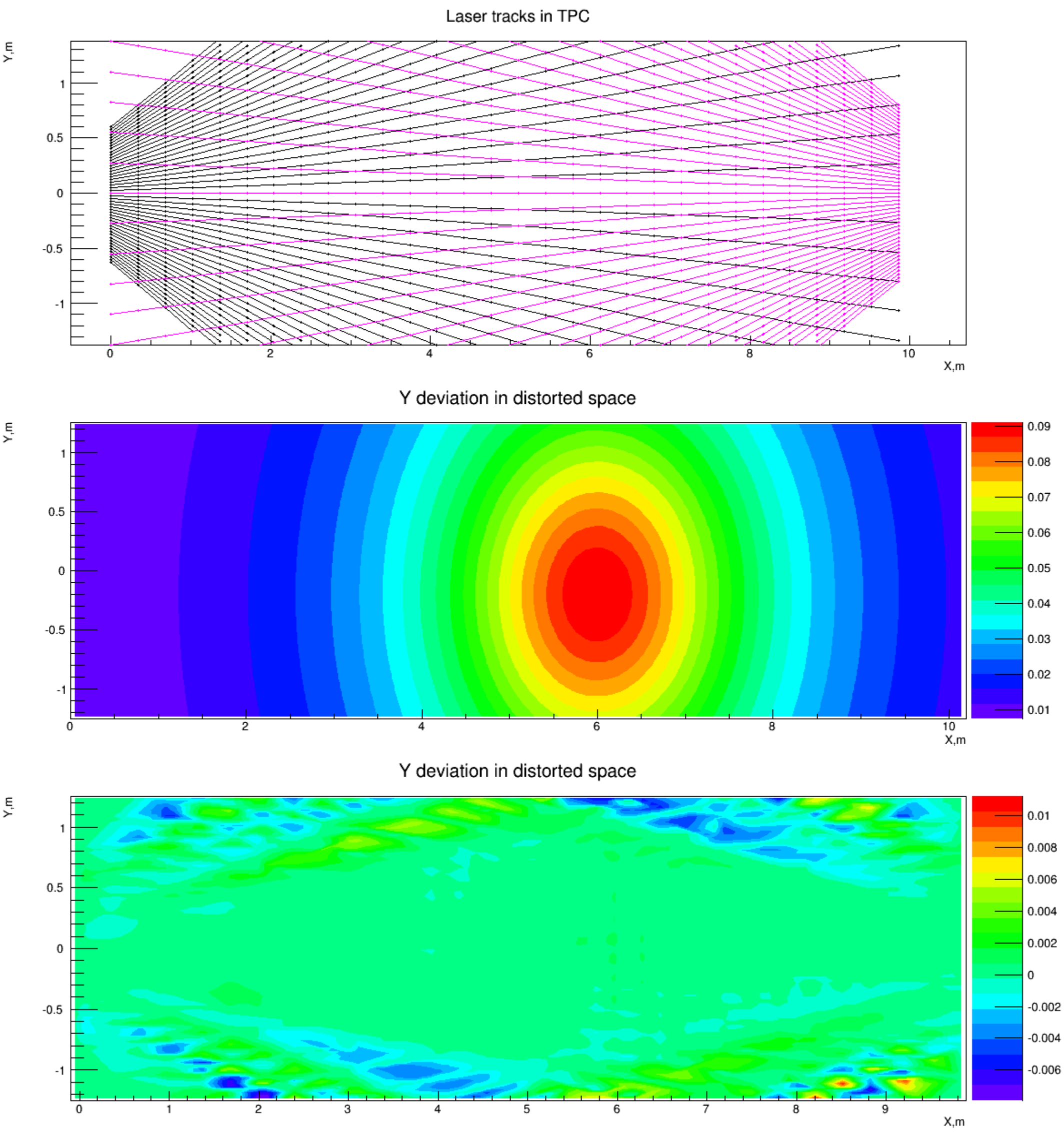

Figure 74: Top: Simulated true laser beam trajectories in the detector; Middle: map of Y coordinate of track deviation under influence of non-uniform electric field; Bottom: residual map of reconstructed track Y-coordinates versus true ones.

8.2 Laser Source and Optics

A Nd:YAG laser emitting light at a wavelength of 1024 nm is used as the primary light source [124]. Inside the laser head, nonlinear crystals are installed in the beam line for frequency doubling and summing, resulting in a wavelength of 266 nm needed for ionization of liquid argon. For this wavelength, the Nd:YAG laser is specified to produce an output energy of 60 mJ for each 4 to 6 ns long pulse and a horizontal polarization. The maximal repetition rate is 10 Hz; the beam has a divergence of 0.5 mrad.

An optical table, as seen in figure 75, was developed to introduce the necessary parts in a stable and compact environment. With regard to the operation of the optical table on MicroBooNE, the parts were chosen to be accessible remotely where necessary. The emitted laser beam contains not only ultraviolet light but also all other harmonics generated in the crystal and the primary light of 1024 nm. Dichroic Mirrors optimized to reflect only wavelengths in the UV region are used to filter higher wavelengths out. To absorb the transmitted wavelength behind the mirrors, glass-ceramic plates are installed. The beam leaving the laser head is reflected by the first 45°-mirror into an attenuator. For optical adjustment and verification of the non-visible UV-beam, a green alignment laser is placed behind this mirror and adjusted such that its path is coincident with the UV-laser beam. In the attenuator (Altechna Wattpilot) a turnable $\lambda/2$-plate enables rotation of the orientation of the laser beam polarization. Behind the attenuator two parallel plates are installed such that the angle of the incident beam matches the Brewster angle of the reflector. Modulating the polarization of the beam adjusts the intensity of the reflected beam. After the attenuator an aperture is put in the optical path of the beam to control the beam diameter. The last part in the beam line is a remotely-controllable mirror mount (Zaber T-OMG), which directs the beam to the laser feedthrough on the cryostat. A photodiode (Thorlabs DET10A/M), which is sensitive in the ultraviolet region, detects the scattered light when a laser pulse is fired. Its signal is then used as a trigger for data taking. Both the UV-laser head and the optical table are mounted on a 15 mm thick aluminum plate.

8.3 Steering System

One of the main challenges of the laser calibration system is the introduction of a steerable laser beam into the detector. Earlier, an evacuated quartz-glass [125] was utilized to introduce a laser beam into liquid argon, however this beam had a fixed path through the detector. For the purpose of scanning the full detector a fully steerable mirror in liquid argon is necessary. In the MicroBooNE detector, this is achieved by mounting a mirror on a horizontally-rotatable support structure. A rack and pinion construction, where the mirror is mounted on the frontside of a half gear (pinion), provides the necessary freedom for the vertical movement (see figure 76 right). To steer the horizontal movement from outside the cryostat, a commercial differentially-pumped rotational feedthrough is deployed (see figure 76 left). The rack and pinion construction is attached to a linear feedthrough. Both feedthroughs are motorized to allow for remote control and automation of the mirror movement. The mirror support structure was fabricated out of polyamide-imide (Duratron T4301 PAI), which has a very low outgassing rate and low thermal expansion coefficient, and is certified for operation at 87 K. To minimize the probability of discharges due to the close location of the feedthrough to the field cage structure in MicroBooNE, no conductive parts were used in the support structure. The support structure has a total length of 2.5 m in MicroBooNE. Both feedthroughs are equipped with high precision position encoders from Heidenhain. The accuracy of the encoders is chosen such that a position accuracy of 2 mm for the laser beam spot over 10 m distance is achieved. An external interface box controls the encoders and records a position reading

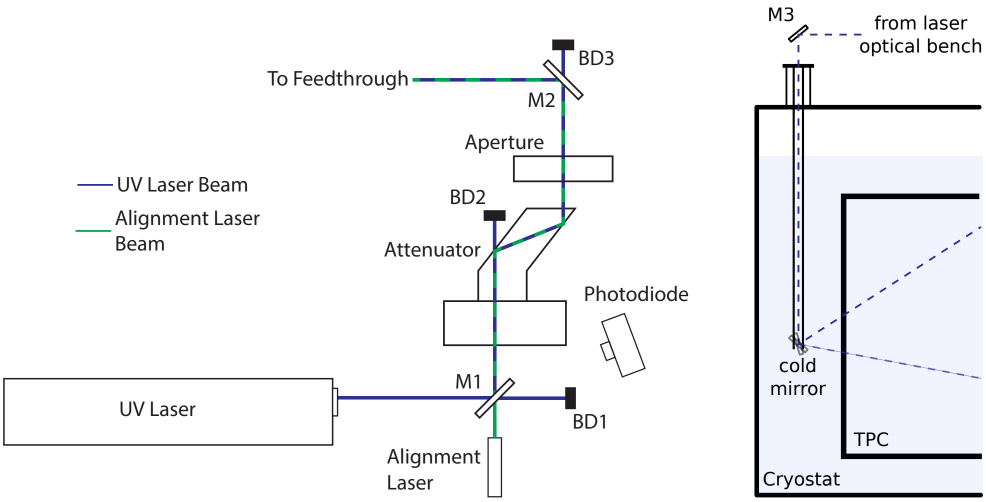

(a) Optical Table (b) Side View

Figure 75: (a) A schematic drawing (not to scale) of the components used for laser beam configuration. An alignment laser (visible light) is introduced along the UV-laser path at the first dichroic mirror (M1), such that the paths overlap. In the attenuator the UV-laser beam intensity can be adjusted to the desired level, and the diameter of the beam is controlled by an aperture. A motorized mirror (M2) deflects the light into the direction of the feedthrough. Beam dumps (BD) are installed behind all mirrors to absorb the non-reflected laser light. (b) Side view of the cryostat indicating the mirror support structure with respect to the LArTPC.

upon receiving a trigger signal from the photodiode. The DAQ computer accesses the position information over an ethernet connection. The same computer is also used for steering the two motors via a motor driver system (over a RS232 interface).

8.4 Performance Tests and Initial Operation

A full performance test of the laser calibration system identical to the one installed in the MicroBooNE LArTPC was performed prior to the final installation. Apart from the general proof-of-principle of the laser calibration system, several operationally relevant parameters were identified. These include scanning speed, positioning accuracy, positioning limits, optimal laser beam intensity, beam diameter, and the minimal achievable field distortion which can be resolved. The test system consists of a LArTPC equipped with 64 readout channels and an active area of about 400 cm^2, with a drift distance of 40 cm (see [126] for further details).

Several tests of the motorized feedthrough were performed under warm conditions before cold tests were conducted. One crucial parameter for the quality of the electric field calibration is the resolution at which laser tracks can be aimed in the detector. For the rotational axis this angle is directly measured on a circular scale. For the vertical movement the linear displacement of the bellow is translated into a rotation inside the cryostat, as can be seen in the CAD drawing in figure 76. This construction introduces uncertainties to the measurement position and backlash. The backlash can be compensated by always approaching positions from the same direction. For the translation of the linear movement ΔL into a rotation $\Delta\phi$ the translation ratio s according to

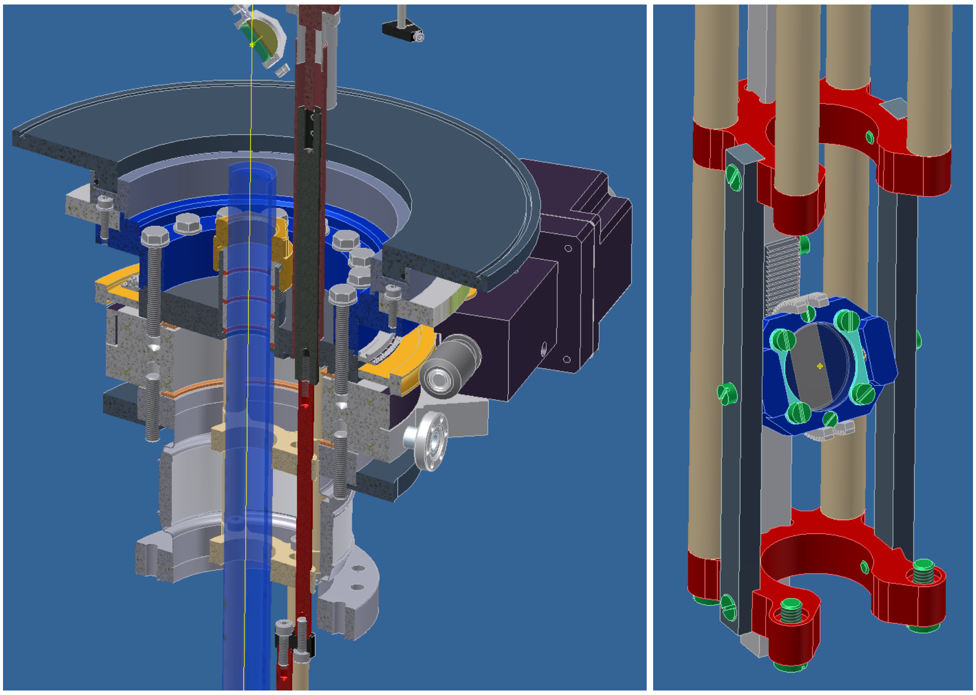

Figure 76: Left: CAD cutaway drawing of the feedthrough construction is shown. The yellow line indicates the laser path. Right, CAD drawing of the cold mirror including the support structure.

$\Delta L = s \cdot \Delta\phi$ was measured with a laser alignment device[3]. The obtained ratio is $s = 0.3499 \pm 0.0002\ mm/^{\circ}$. The dominant uncertainty in the vertical position measurement is the accuracy of the encoder $\sigma_{linear} = \pm 1\ \mu m$, which translates into a vertical rotation measurement accuracy $\sigma_{vertical} = 10.29''$.

Horizontal movement limitations arise from the construction of the feedthrough system, namely the warm mirror support structure. This limit has its origins in the way of mounting the laser table relative to the feedthrough on the MicroBooNE cryostat. Vertically the mirror can be rotated more than 45° relative to the horizon in both directions. In an upward looking configuration, no limitations arise which would affect the coverage of the detector with the beam. A limit arises when the mirror faces the opposite downward direction, when properly aligned onto the centre of the mirror the laser diameter and the size of the mirror limits the achievable coverage. However slight misalignment will affect this limit, since the beam will not be in the optimal spot anymore. In warm tests an maximal downward angle of the beam of 52.5° with respect to the horizon was achieved. During the cold tests the horizontal movement speed was set to 2.6 °/s and the vertical speed to 1 °/s, horizontally an angle of 81 ° was covered and 22 ° vertically, respectively. Tests in warm of the fully expanded setup showed vibrations if to high speed was chosen. The vibrations are expected to be dampened with a more stable fixation on the detector and the immersion of the setup in liquid argon.

Modulation of the beam energy with respect to the vertical alignment of the cold mirror was found to be crucial for obtaining sufficient ionization in the detector. Investigations showed that

[3] Bosch GPL3.

the reflectivity of the selected dielectric mirrors, which were optimized for 45° in air, are very sensitive to the angle of incidence in liquid argon. Therefore during a calibration run, the beam energy has to be controlled. The emitted UV-laser beam has a diameter of 6 mm and will spatially diverge during propagation. A beam with this diameter will produce an ionization signal larger than the wire spacing, which will limit the capabilities of the full system. With the aperture a small as possible diameter of the laser was selected to enter the detector. Measurements of the diameter were performed with thermal paper (used for thermal printing) on which the selected beam spot burns in. The minimal achieved diameter was 1 mm.

9. Conclusion

The MicroBooNE detector is the culmination of several years of development and construction. It is the largest LArTPC ever constructed in the U.S., and represents a major technological advance that future experiments will build upon.

Acknowledgments

We gratefully acknowledge support from the National Science Foundation, the United States Department of Energy, and the EU funding gods.

References

[1] **MiniBooNE** Collaboration, A. A. Aguilar-Arevalo et al., *Unexplained Excess of Electron-Like Events From a 1-GeV Neutrino Beam*, *Phys. Rev. Lett.* **102** (2009) 101802, [arXiv:0812.2243].

[2] T. A. Mueller, D. Lhuillier, M. Fallot, A. Letourneau, S. Cormon, M. Fechner, L. Giot, T. Lasserre, J. Martino, G. Mention, A. Porta, and F. Yermia, *Improved predictions of reactor antineutrino spectra*, *Phys. Rev. C* **83** (May, 2011) 054615.

[3] P. Huber, *Determination of antineutrino spectra from nuclear reactors*, *Phys. Rev. C* **84** (Aug, 2011) 024617.

[4] **GALLEX** Collaboration, W. Hampel et al., *Final results of the Cr-51 neutrino source experiments in GALLEX*, *Phys. Lett.* **B420** (1998) 114–126.

[5] **SAGE** Collaboration, J. N. Abdurashitov et al., *Measurement of the response of the Russian-American gallium experiment to neutrinos from a Cr-51 source*, *Phys. Rev.* **C59** (1999) 2246–2263, [hep-ph/9803418].

[6] C. Adams et al., *LAr1-ND: Testing Neutrino Anomalies with Multiple LArTPC Detectors at Fermilab*, arXiv:1309.7987.

[7] T. Doke, *A historical view on the r&d for liquid rare gas detectors*, *Nuclear Instruments and Methods in Physics Research Section A* **327** (1993), no. 1 113 – 118.

[8] W. Willis and V. Radeka, *Liquid-argon ionization chambers as total-absorption detectors*, *Nuclear Instruments and Methods* **120** (1974), no. 2 221 – 236.

[9] C. Rubbia, *The liquid-argon time projection chamber: A new concept for neutrino detectors*, EP Internal Report 77-8, CERN, May, 1977.

[10] P. Benetti et al., *A three-ton liquid argon time projection chamber*, *Nuclear Instruments and Methods in Physics Research Section A: Accelerators, Spectrometers, Detectors and Associated Equipment* **332** (1993), no. 3 395 – 412.

[11] P. Cennini et al., *Performance of a three-ton liquid argon time projection chamber*, *Nuclear Instruments and Methods in Physics Research Section A: Accelerators, Spectrometers, Detectors and Associated Equipment* **345** (1994), no. 2 230 – 243.

[12] F. Arneodo et al., *The ICARUS 50-l LAr TPC in the CERN ν beam*, `hep-ex/9812006`.

[13] S. Amerio et al., *Design, construction and tests of the ICARUS T600 detector*, *Nuclear Instruments and Methods in Physics Research Section A: Accelerators, Spectrometers, Detectors and Associated Equipment* **527** (2004), no. 3 329 – 410.

[14] S. Amoruso et al., *Measurement of the muon decay spectrum with the icarus liquid argon tpc*, *The European Physical Journal C - Particles and Fields* **33** (2004), no. 2 233–241.

[15] S. Amoruso et al., *Study of electron recombination in liquid argon with the {ICARUS} {TPC}*, *Nuclear Instruments and Methods in Physics Research Section A: Accelerators, Spectrometers, Detectors and Associated Equipment* **523** (2004), no. 3 275 – 286.

[16] M. Antonello et al., *Detection of cherenkov light emission in liquid argon*, *Nuclear Instruments and Methods in Physics Research Section A: Accelerators, Spectrometers, Detectors and Associated Equipment* **516** (2004), no. 2–3 348 – 363.

[17] S. Amoruso et al., *Analysis of the liquid argon purity in the ICARUS T600 TPC*, *Nuclear Instruments and Methods in Physics Research Section A: Accelerators, Spectrometers, Detectors and Associated Equipment* **516** (2004), no. 1 68 – 79.

[18] F. Arneodo et al., *Observation of long ionizing tracks with the ICARUS T600 first half-module*, *Nuclear Instruments and Methods in Physics Research Section A: Accelerators, Spectrometers, Detectors and Associated Equipment* **508** (2003), no. 3 287 – 294.

[19] P. Aprili et al., *The ICARUS experiment: A second-generation proton decay experiment and neutrino observatory at the gran sasso laboratory. cloning of t600 modules to reach the design sensitive mass. (addendum)*, LNGS-EXP 13/89 add.2/01 CERN-SPSC-2002-027, CERN, 2002.

[20] D. B. Cline, J. G. Learned, K. McDonald, and F. Sergiampietri, *LANNDD–a massive liquid argon detector for proton decay, supernova and solar neutrino studies and a neutrino factory detector*, *Nuclear Instruments and Methods in Physics Research Section A: Accelerators, Spectrometers, Detectors and Associated Equipment* **503** (2003), no. 1–2 136 – 140. Proceedings of the 3rd International Workshop on Neutrino Factories based on Muon Storage Rings.

[21] A. Rubbia, *Experiments for CP violation: A Giant liquid argon scintillation, Cerenkov and charge imaging experiment?*, `hep-ph/0402110`.

[22] A. Rubbia, *Underground Neutrino Detectors for Particle and Astroparticle Science: The Giant Liquid Argon Charge Imaging ExpeRiment (GLACIER)*, *J.Phys.Conf.Ser.* **171** (2009) 012020, [`arXiv:0908.1286`].

[23] **LAGUNA** Collaboration. http://laguna.ethz.ch/LAGUNA/Welcome.html.

[24] A. Stahl et al., *Expression of Interest for a very long baseline neutrino oscillation experiment (LBNO)*, Tech. Rep. CERN-SPSC-2012-021. SPSC-EOI-007, CERN, Geneva, Jun, 2012.

[25] S. Agarwalla et al., *The mass-hierarchy and CP-violation discovery reach of the LBNO long-baseline neutrino experiment*, *JHEP* **1405** (2014) 094, [`arXiv:1312.6520`].

[26] C. Adams et al., *The Long-Baseline Neutrino Experiment: Exploring Fundamental Symmetries of the Universe*, `arXiv:1307.7335`.

[27] **DUNE** Collaboration, R. Acciarri et al., *Long-Baseline Neutrino Facility (LBNF) and Deep Underground Neutrino Experiment (DUNE)*, `arXiv:1512.0614`.

[28] C. Anderson et al., *The ArgoNeuT Detector in the NuMI Low-Energy beam line at Fermilab*, *JINST* **7** (2012) P10019, [`arXiv:1205.6747`].

[29] R. Acciarri et al., *A study of electron recombination using highly ionizing particles in the ArgoNeuT Liquid Argon TPC*, *JINST* **8** (2013) P08005, [`arXiv:1306.1712`].

[30] C. Anderson et al., *First Measurements of Inclusive Muon Neutrino Charged Current Differential Cross Sections on Argon*, *Phys.Rev.Lett.* **108** (2012) 161802, [`arXiv:1111.0103`].

[31] R. Acciarri et al., *Measurements of Inclusive Muon Neutrino and Antineutrino Charged Current Differential Cross Sections on Argon in the NuMI Antineutrino Beam*, *Phys.Rev.* **D89** (2014) 112003, [`arXiv:1404.4809`].

[32] R. Acciarri et al., *First Measurement of Neutrino and Antineutrino Coherent Charged Pion Production on Argon*, `arXiv:1408.0598`.

[33] R. Acciarri et al., *LArIAT: Liquid Argon In A Testbeam*, `arXiv:1406.5560`.

[34] A. Szelc, *The LArIAT light readout system*, *JINST* **8** (2013) C09011.

[35] M. Adamowski et al., *The Liquid Argon Purity Demonstrator*, *JINST* **9** (2014) P07005, [`arXiv:1403.7236`].

[36] B. Rebel et al., *Results from the Fermilab materials test stand and status of the liquid argon purity demonstrator*, *J.Phys.Conf.Ser.* **308** (2011) 012023.

[37] D. Montanari et al., *First scientific application of the membrane cryostat technology.*, .

[38] **HEPAP Subcommittee** Collaboration, S. Ritz et al., *Building for Discovery: Strategic Plan for U.S. Particle Physics in the Global Context*, .

[39] A. Marchionni, *Status and New Ideas Regarding Liquid Argon Detectors*, *Ann.Rev.Nucl.Part.Sci.* **63** (2013) 269–290, [`arXiv:1307.6918`].

[40] P. Adamson et al., *The NuMI Neutrino Beam*, *Nucl. Instrum. Meth.* **A806** (2016) 279–306, [`arXiv:1507.0669`].

[41] **MiniBooNE** Collaboration, A. Aguilar-Arevalo et al., *The Neutrino Flux prediction at MiniBooNE*, *Phys.Rev.* **D79** (2009) 072002, [`arXiv:0806.1449`].

[42] E. Aprile, K. Giboni, and C. Rubbia, *A study of ionization electrons drifting large distances in liquid and solid argon*, *Nuclear Instruments and Methods in Physics Research Section A: Accelerators, Spectrometers, Detectors and Associated Equipment* **241** (1985), no. 1 62 – 71.

[43] C. Tegeler, R. Span, and W. Wagner, *A new equation of state for argon covering the fluid region for temperatures from the melting line to 700 k at pressures up to 1000 mpa*, *Journal of Physical and Chemical Reference Data* **28** (1999), no. 3 779–850.

[44] R. L. Amey and R. H. Cole, *Dielectric constants of liquefied noble gases and methane*, *The Journal of Chemical Physics* **40** (1964), no. 1 146–148.

[45] C. Amsler et al., *Review of particle physics*, *Physics Letters B* **667** (2008), no. 1–5 1 – 6. http://pdg.lbl.gov/2008/reviews/rpp2008-rev-passage-particles-matter.pdf.

[46] E. Shibamura, A. Hitachi, T. Doke, T. Takahashi, S. Kubota, and M. Miyajima, *Drift velocities of electrons, saturation characteristics of ionization and W-values for conversion electrons in liquid argon, liquid argon-gas mixtures and liquid xenon*, *Nuclear Instruments and Methods* **131** (Dec., 1975) 249–258.

[47] M. Miyajima, T. Takahashi, S. Konno, T. Hamada, S. Kubota, H. Shibamura, and T. Doke, *Average energy expended per ion pair in liquid argon*, *Phys. Rev. A* **9** (Mar, 1974) 1438–1443.

[48] E. Shibamura, T. Takahashi, S. Kubota, and T. Doke, *Ratio of diffusion coefficient to mobility for electrons in liquid argon*, *Phys. Rev. A* **20** (Dec, 1979) 2547–2554.

[49] S. Derenzo, *Electron diffusion and positive ion charge retention in liquid-filled high-resolution multistrip ionization-mode chambers*, *Lawrence Berkeley Laboratory, Group A Physics Note No. 786* (1974).

[50] V. Atrazhev and I. Timoshkin, *Transport of electrons in atomic liquids in high electric fields*, *IEEE Transactions on Dielectrics and Electrical Insulation* **5** (June, 1998) 450 –457.

[51] *ASME boiler and pressure vessel code: an international code. I - Rules for construction of power boiler*. American Society of Mechanical Engineers, New York, NY, 2010.

[52] B. Jones, C. Chiu, J. Conrad, C. Ignarra, T. Katori, et al., *A Measurement of the Absorption of Liquid Argon Scintillation Light by Dissolved Nitrogen at the Part-Per-Million Level*, *JINST* **8** (2013) P07011, [arXiv:1306.4605].

[53] Barber-Nichols Inc., 6325 West 55th Avenue, Arvada, CO 80002 USA.

[54] Sigma-Aldrich, P.O. Box 14508, St. Louis, MO 63178 USA.

[55] BASF Corp., 100 Park Avenue, Florham Park, NJ 07932 USA.

[56] Aspen Aerogels, Inc., 30 Forbes Road, Building B, Northborough, MA 01532 USA.

[57] G. Carugno et al., *Electron lifetime detector for liquid argon*, *Nuclear Instruments and Methods in Physics Research Section A: Accelerators, Spectrometers, Detectors and Associated Equipment* **292** (1990) 580.

[58] L. F. Bagby et al., *Breakdown voltage of metal-oxide resistors in liquid argon*, *JINST* **9** (2014), no. 11 T11004, [arXiv:1408.4013].

[59] **MicroBooNE** Collaboration, R. Acciarri et al., *Liquid Argon Dielectric Breakdown Studies with the MicroBooNE Purification System*, *JINST* **9** (2014), no. 11 P11001, [arXiv:1408.0264].

[60] J. Asaadi, J. M. Conrad, S. Gollapinni, B. J. P. Jones, H. Jostlein, J. M. St. John, T. Strauss, S. Wolbers, and J. Zennamo, *Testing of High Voltage Surge Protection Devices for Use in Liquid Argon TPC Detectors*, *JINST* **9** (2014) P09002, [arXiv:1406.5216].

[61] R. Acciarri et al., *Construction and Assembly of the Wire Planes for the MicroBooNE Time Projection Chamber*, arXiv:1609.0616.

[62] W. Buescher, *Spectrum Laboratory*, . http://www.qsl.net/dl4yhf/spectra1.html.

[63] "Citranox acid detergent." http://www.alconox.com/resources/StandardDocuments/MSDS/msds_citranox_english_ghs.pdf.

[64] "Simple Green detergent." http://simplegreen.com/pdfs/MSDS_EN-US_AllPurposeCleaner.pdf.

[65] "Elma Clean 65." http://www.elma-ultrasonic.com/fileadmin/downloads/CleaningAgents/SafetyDataSheets/GB/S_EC%2065_GB.pdf.

[66] L. Bugel, J. M. Conrad, C. Ignarra, B. J. P. Jones, T. Katori, T. Smidt, and H. K. Tanaka, *Demonstration of a Lightguide Detector for Liquid Argon TPCs*, *Nucl. Instrum. Meth.* **A640** (2011) 69–75, [arXiv:1101.3013].

[67] **MicroBooNE** Collaboration, T. Katori, *MicroBooNE, A Liquid Argon Time Projection Chamber (LArTPC) Neutrino Experiment*, *AIP Conf. Proc.* **1405** (2011) 250–255, [arXiv:1107.5112].

[68] C. Chiu, C. Ignarra, L. Bugel, H. Chen, J. Conrad, et al., *Environmental Effects on TPB Wavelength-Shifting Coatings*, *JINST* **7** (2012) P07007, [arXiv:1204.5762].

[69] B. Baptista, L. Bugel, C. Chiu, J. Conrad, C. Ignarra, et al., *Benchmarking TPB-coated Light Guides for Liquid Argon TPC Light Detection Systems*, arXiv:1210.3793.

[70] T. Briese, L. Bugel, J. Conrad, M. Fournier, C. Ignarra, et al., *Testing of Cryogenic Photomultiplier Tubes for the MicroBooNE Experiment*, *JINST* **8** (2013) T07005, [arXiv:1304.0821].

[71] B. Jones, T. Alexander, H. Back, G. Collin, J. Conrad, et al., *The Effects of Dissolved Methane upon Liquid Argon Scintillation Light*, *JINST* **8** (2013) P12015, [arXiv:1308.3658].

[72] **MicroBooNE** Collaboration, T. Katori, *The MicroBooNE light collection system*, *JINST* **8** (2013) C10011, [arXiv:1307.5256].

[73] B. Baller, N. Buchanan, F. Cavanna, H. Chen, E. Church, et al., *Liquid Argon Time Projection Chamber Research and Development in the United States*, *JINST* **9** (2014) T05005, [arXiv:1307.8166].

[74] Z. Moss, L. Bugel, G. Collin, J. Conrad, B. Jones, et al., *Improved TPB-coated Light Guides for Liquid Argon TPC Light Detection Systems*, arXiv:1410.6256.

[75] **MicroBooNE** Collaboration, J. Conrad, B. Jones, Z. Moss, T. Strauss, and M. Toups, *The Photomultiplier Tube Calibration System of the MicroBooNE Experiment*, *JINST* **10** (2015), no. 06 T06001, [arXiv:1502.0415].

[76] R. Acciarri, M. Adamowski, D. Artrip, B. Baller, C. Bromberg, et al., *Summary of the Second Workshop on Liquid Argon Time Projection Chamber Research and Development in the United States*, arXiv:1504.0560.

[77] Z. Moss, M. Toups, L. Bugel, G. Collin, and J. Conrad, *Anode-Coupled Readout for Light Collection in Liquid Argon TPCs*, arXiv:1507.0199.

[78] B. J. P. Jones, *Sterile Neutrinos in Cold Climates*. PhD thesis, MIT, 2015.

[79] M. Suzuki and S. Kubota, *Mechanism of proportional scintillation in argon, krypton and xenon*, *Nuclear Instruments and Methods* **164** (1979), no. 1 197 – 199.

[80] A. Hitachi, T. Takahashi, N. Funayama, K. Masuda, J. Kikuchi, and T. Doke, *Effect of ionization density on the time dependence of luminescence from liquid argon and xenon*, *Phys. Rev. B* **27** (May, 1983) 5279–5285.

[81] **WArP** Collaboration, R. Acciarri et al., *Effects of Nitrogen contamination in liquid Argon*, *JINST* **5** (2010) P06003, [arXiv:0804.1217].

[82] N. Ishida, M. Chen, T. Doke, K. Hasuike, A. Hitachi, M. Gaudreau, M. Kase, Y. Kawada, J. Kikuchi, T. Komiyama, K. Kuwahara, K. Masuda, H. Okada, Y. H. Qu, M. Suzuki, and T. Takahashi, *Attenuation length measurements of scintillation light in liquid rare gases and their mixtures using an improved reflection suppresser*, *Nuclear Instruments and Methods in Physics Research A* **384** (Feb., 1997) 380–386.

[83] Hamamatsu, "Large area photomultipier tubes." Specification for R5912 and R5912-02 photomultiplier tubes: http://www.hamamatsu.com/resources/pdf/etd/LARGE_AREA_PMT_TPMH1286E05.pdf.

[84] E. H. Bellamy, G. Bellettini, F. Gervelli, M. Incagli, D. Lucchesi, C. Pagliarone, F. Zetti, Yu. Budagov, I. Chirikov-Zorin, and S. Tokar, *Absolute calibration and monitoring of a spectrometric channel using a photomultiplier*, *Nucl. Instrum. Meth.* **A339** (1994) 468–476.

[85] H. O. Meyer, *Dark Rate of a Photomultiplier at Cryogenic Temperatures*, `arXiv:0805.0771`.

[86] H. Meyer, *Spontaneous electron emission from a cold surface*, *EPL* (2010), no. 89 58001.

[87] Hamamatsu Photonics, *Photomultiplier Tubes, Basics and Applications, Third Edition, Chapter 13.9*, . https://www.hamamatsu.com/resources/pdf/etd/PMT_handbook_v3aE.pdf.

[88] W. Burton and B. Powell, *Fluorescence of tetraphenyl-butadiene in the vacuum ultraviolet.*, *Appl Opt.* **12** (1973), no. 1 87–9.

[89] C. M. Ignarra, *Sterile Neutrino Searches in MiniBooNE and MicroBooNE.* PhD thesis, MIT, Cambridge, 2014.

[90] V. Gehman, S. Seibert, K. Rielage, A. Hime, Y. Sun, et al., *Fluorescence Efficiency and Visible Re-emission Spectrum of Tetraphenyl Butadiene Films at Extreme Ultraviolet Wavelengths*, *Nucl.Instrum.Meth.* **A654** (2011) 116–121, [`arXiv:1104.3259`].

[91] R. Francini, R. Montereali, E. Nichelatti, M. Vincenti, N. Canci, et al., *VUV-Vis optical characterization of Tetraphenyl-butadiene films on glass and specular reflector substrates from room to liquid Argon temperature*, *JINST* **8** (2013) P09006.

[92] B. J. P. Jones, *A simulation of the optical attenuation of TPB coated light-guide detectors*, *JINST* **8** (2013) C10015, [`arXiv:1307.6906`].

[93] Sundance Supply, "Lexan Thermoclear Multiwall Polycarbonate Sheet." https://www.sundancesupply.com/Lexan.pdf.

[94] "Stycast 2850." http://www.ellsworth.com/manufacturers/emerson-cuming.

[95] J. B. Birks and K. N. Kuchela, *Energy transfer in fluorescent plastic solutions*, *Disc. Faraday. Soc* **27** (1959) 57–63.

[96] J. B. Birks and K. N. Kuchela, *Energy transfer in organic systems ii: Solute-solute transfer in liquid solutions*, *Proc. Phys.Soc* **77** (1961) 1083.

[97] S. Hanagodimath, B. Siddlingeshwar, J. Thipperudrappa, S. Kumar, and B. Hadimani, *Fluorescence-quenching studies and temperature dependence of fluorescence quantum yield, decay time and intersystem crossing activation energy of tpb*, *J. Lumin* **129** (2008), no. 4 335–339.

[98] L. Liu, "Time resolved fluoresence studies of dye-polymers as excited by laser and beta radiation." PhD Thesis at Texas Tech Univeristy - http://repositories.tdl.org/ttu-ir/bitstream/handle/2346/13744/31295012500558.pdf?sequence=1.

[99] Hamamatsu, "Photomultipler tube r7723, r7724, r7725." http://www.hamamatsu.com/resources/pdf/etd/R7723_TPMH1315E01.pdf.

[100] **ICARUS** Collaboration, A. Ankowski et al., *Energy reconstruction of electromagnetic showers from pi0 decays with the ICARUS T600 Liquid Argon TPC*, *Acta Phys. Polon.* **B41** (2010) 103–125, [`arXiv:0812.2373`].

[101] A. Ereditato Private Communication.

[102] K. Scholberg, *The SuperNova Early Warning System*, *Astron. Nachr.* **329** (2008) 337–339, [arXiv:0803.0531].

[103] M. Massie et al., *Monitoring with Ganglia: Tracking Dynamic Host and Application Metrics at Scale*. O'Reilly Media, 2012.

[104] "Experimental physics and industrial control system." http://www.aps.anl.gov/epics/.

[105] R. Brun and F. Rademakers, *Root — an object oriented data analysis framework*, *Nuclear Instruments and Methods in Physics Research Section A: Accelerators, Spectrometers, Detectors and Associated Equipment* **389** (1997), no. 1 81 – 86.

[106] "Control system studio." http://controlsystemstudio.org/; developer's manual: http://cs-studio.sourceforge.net/docbook/.

[107] *Channel access protocol specification*, September, 2014. http://www.aps.anl.gov/epics/docs/ca.php.

[108] "Net-snmp." http://www.net-snmp.org.

[109] J. Priller, *Epics snmp device support module: Release 1.0.0*, April, 2014. https://groups.nscl.msu.edu/controls/.

[110] M. Rivers, *asyndriver: Asynchronous driver support*, September, 2014. http://www.aps.anl.gov/epics/modules/soft/asyn/.

[111] D. Zimoch, *Epics streamdevice*, September, 2014. http://epics.web.psi.ch/software/streamdevice/doc/.

[112] *Glomation, inc., gesbc-9g20 user's manual, version 0.2*, June, 2009. http://www.glomationinc.com/GESBC-9G20-user-manual.pdf.

[113] D. Huffman, *Peripheral interface: Fan and temperature probe*, September, 2014. http://www-ppd.fnal.gov/EEDOffice-W/Infrastructure_group/Huffman/WEB/uboone/pia.html.

[114] *Ganglia*, September, 2014. http://ganglia.info/.

[115] M. Newville, *Pyepics: Epics channel access for python*, September, 2014. http://cars9.uchicago.edu/software/python/pyepics3/.

[116] *Gnu freeipmi*, September, 2014. http://www.gnu.org/software/freeipmi/.

[117] I. Mandrichenko, A. Norman, A. Petrov, and V. Podstavkov, *Implementation of beam conditions database for intensity frontier experiments*, June, 2012. http://cd-docdb.fnal.gov/cgi-bin/ShowDocument?docid=4781.

[118] I. Badhrees et al., *Measurement of the two-photon absorption cross-section of liquid argon with a time projection chamber*, *New J.Phys.* **12** (2010) 113024, [arXiv:1011.6001].

[119] I. Badhrees et al., *Argontube: An R&D Liquid Argon Time Projection Chamber*, *JINST* **7** (2012) C02011.

[120] A. Ereditato et al., *Design and operation of ARGONTUBE: a 5 m long drift liquid argon TPC*, *JINST* **8** (2013) P07002, [arXiv:1304.6961].

[121] M. Zeller et al., *First measurements with ARGONTUBE, a 5m long drift Liquid Argon TPC*, *Nucl.Instrum.Meth.* **A718** (2013) 454–458.

[122] A. Ereditato et al., *Measurement of the drift field in the ARGONTUBE LAr TPC with 266 nm pulsed laser beams*, arXiv:1408.6635.

[123] A. Ereditato et al., *A steerable UV laser system for the calibration of liquid argon time projection chambers*, arXiv:1406.6400.

[124] "Continuum Lasers." http://www.continuumlasers.com.

[125] I. Badhrees, A. Ereditato, I. Kreslo, M. Messina, U. Moser, B. Rossi, M. S. Weber, M. Zeller, C. Altucci, S. Amoruso, R. Bruzzese, and R. Velotta, *Measurement of the two-photon absorption cross-section of liquid argon with a time projection chamber*, *New Journal of Physics* **12** (2010), no. 11 113024.

[126] A. Ereditato, I. Kreslo, M. Lüthi, C. R. von Rohr, M. Schenk, T. Strauss, M. Weber, and M. Zeller, *A steerable uv laser system for the calibration of liquid argon time projection chambers*, *Journal of Instrumentation* **9** (2014), no. 11 T11007.